

Magnetic Resonance Imaging Method for Measuring Functional Cerebral Blood Volume Changes at 7 Tesla

Ludwig-Maximilians-Universität München
Max-Planck-Institut für Kognitions- und Neurowissenschaften Leipzig
By Laurentius Huber
Under the Supervision of PD Dr. Walter Assmann

November 1, 2011

Contents

0.1	Glossary	5
0.2	Abstract	7
1	Introduction	8
2	Physical Basis	10
2.1	Magnetic Resonance (MR)	10
2.1.1	Spin in Magnetic Field	10
2.1.2	Macroscopic Magnetization in RF Field	10
2.2	Magnetic Resonance Imaging	12
2.2.1	Data Acquisition	13
2.2.2	Imaging	14
2.2.3	Pulse Sequence	14
2.2.4	EPI	14
2.2.5	EPI Artifacts	15
2.2.6	Signal to Noise Ratio	18
2.2.7	Specific Absorption Rate	19
2.3	Adiabatic Inversion	19
2.3.1	Resistance of Adiabatic Pulses Against B_1 -Inhomogeneities at High Fields	19
2.3.2	Constraints for Adiabatic Inversion	21
2.3.3	Design of Adiabatic Inversion Pulses in MRI	22
3	Physiological Basis	26
3.1	Neural Activity and Brain Metabolism	26
3.1.1	Neurons	26
3.1.2	Cerebral Blood Vessels	26
3.1.3	Perfusion of the Brain at Rest and During Activation	27
3.2	Physiological Variables	28
3.3	Hyperoxia and Hypercapnia	31
4	fMRI Methods: ASL and BOLD	33
4.1	MRI Techniques to Measure Perfusion	33
4.2	BOLD	34
4.2.1	Time Course of the BOLD Response	34
5	VASO	36
5.1	CBV Based fMRI	36

5.2	VASO	36
5.2.1	Components of Cerebral Blood Volume	38
5.2.2	VASO at High Fields	39
5.2.3	ASL and Steady-State Effect	39
5.2.4	Dependencies of blood T_1 on VASO	39
5.2.5	Quantification of CBV Change from VASO Signal Changes	41
5.3	BOLD-Corrected VASO	43
5.4	Slab-Selective VASO	48
5.4.1	Steady-State Considerations in Traditional VASO at High Fields	48
5.4.2	Slab-Selective VASO	48
5.4.3	Transit Times of Blood	51
5.4.4	Nullled CSF	52
5.5	Determination of GM Fraction of a Voxel in the BOLD-Corrected VASO Sequence	53
5.5.1	Introduction	53
5.5.2	Theoretical Signal Composition at the Blood-Nulling Point	55
5.5.3	A Simple Fast Way of Determining GM Fraction	57
6	Sequence Development and Validation	60
6.1	Measurements and Discussion of the Dependencies of the tr-FOCI Adiabatic Inversion Pulse	60
6.1.1	Attributes of an Adiabatic Inversion Pulse	60
6.1.2	RF Pulse Magnitude B_1	61
6.1.3	Bandwidth μ	62
6.1.4	Duration T	64
6.1.5	T_2 -Relaxation During Inversion	68
6.1.6	Position and Thickness of the Slab	72
6.1.7	B_1 Measurements	75
6.1.8	B_1 Sensitivity in a Water Phantom	76
6.2	Inversion Efficiency and T_1 In Vivo	79
6.3	Arbitrary Inversion Efficiency	81
6.4	Magnetization Transfer	83
6.4.1	MT-VASO	83
6.4.2	MT-Experiment	84
6.5	Experimental Validation of BOLD-Corrected VASO Calculation	85
6.5.1	Hyperoxia-Experiment	85
6.5.2	Interpretation of an Increase in BOLD-Corrected VASO during Hyperoxia	87
7	Materials and Methods	88
7.1	Experimental Setup	88
7.2	Parameters of the Slab-Selective BOLD-Corrected VASO Sequence	88
7.2.1	Parameters of the Inversion Pulse	88
7.2.2	Parameters of the Sequence	89

7.3	Session Protocol	90
7.3.1	Additional Subjects	91
7.4	Processing of the Functional Data	92
8	Results and Discussion	97
8.1	Relative Change in CBV	97
8.2	Connection of Signal Change in VASO and in BOLD to GM and CSF Content	99
8.3	Time Courses of VASO and BOLD Signal	100
8.4	BOLD Correction	101
8.5	TR-Dependencies	102
8.6	Influence of Slab Thickness	103
8.7	Post Stimulus Undershoot	104
8.8	Stimulus Length	107
8.9	Spatial Specificity of BOLD and VASO	108
8.10	CSF	109
8.11	Signal Change Distribution	111
8.12	Noise-Induced Bias in $\frac{\Delta CBV}{CBV_{rest}}$ Determination	114
8.12.1	Cluster Threshold	116
8.13	GM-Content	116
8.14	Gender Dependencies	117
8.15	T ₁ Dependency on Blood Nulling Time	118
8.16	Water Exchange Between Tissue and Blood During TI	118
9	Conclusion	119
	Bibliography	120

0.1 Glossary

Abbreviation	Name	Description
AFI	A ctual F lip-angle I maging	method to determine the RF amplitude B_1
AFP	A diabatic F ast P assage	technique to rotate magnetization with RF pulses
ASL	A rterial S in L abeling	MRI method measuring CBF
BOLD	B lood O xygen L evel D ependence	MRI contrast emergent from hemoglobin oxygenation changes
CASL	C ontinuous A rterial S pin L abeling	
CBF	C erebral B lood F low	
CBV	C erebral B lood V olume	
CMRGlc	C erebral M etabolic R ate of G lucose	
CMRO ₂	C erebral M etabolic R ate of O ₂	
CSF	C erebrospinal F luid	bodily fluid inside and around the brain
CVR	C erebral V ascular R esistance	
EPI	E cho P lanar I maging	very fast MRI acquisition method
FAIR	F low-sensitive A lternating I nversion R ecovery	PASL method with overlapping image and label slice
FLAIR	F luid A ttenuated I nversion R ecovery	MRI sequence that reduces signal contribution of CSF
fMRI	f unctional M agnetic R esonance I maging	MRI technique to visualize local change in neural activity
FOCI	F requency O ffset C orrected I nversion	class of adiabatic inversion pulses with reduced spatial localization error
FOV	F ield of V iew	total size on an image
GE	G radient E cho	MRI data acquisition method based on alternating gradients
GM	G rey M atter	cortical component, which contains neural cell bodies
MR	M agnetic R esonance	phenomenon that magnetic nuclei absorb and re-emit RF radiation in a magnetic field
MRI	M agnetic R esonance I maging	
MT	M agnetization T ransfer	MRI contrast based on magnetization exchange between free and bound water
PASL	P ulsed A rterial S pin L abeling	
PET	P ositron E mission T omography	nuclear medicine imaging technique
RF	R adio F requency	frequency range of precession of spins in common MRI scanners

Abbreviation	Name	Description
SAR	Specific Absorption Rate	watts of deposited RF energy per kg per s
SNR	Signal to Noise Ratio	measure of the quality of MR Images
TE	Echo Time	time between excitation and echo in RF data acquisition
TI	Inversion Time	time between inversion and excitation in an MRI sequence
tSNR	temporal Signal to Noise Ratio	measure of time course stability of MR images
TR	Repetition Time	time between RF-excitations of MR acquisitions
tr-FOCI	time resampled FOCI	category of slice selective inversion pulses tailored for ultra high fields
VASO	Vascular Space Occupancy	MRI method for measuring CBV changes
VERSE	Variable Rate Selective Excitation	see VR
VERVE	Venous Refocusing for Volume Estimation	MRI method for measuring changes in venous CBV
VR	Variable Rate	RF pulses that are played concurrently with a time-varying gradient also known as VERSE
WM	White Matter	cortical component, which consists mostly of myelinated axons

0.2 Abstract

Functional changes in cerebral blood volume (CBV) may localize changes in neural activity better than other MRI-accessible physiological variables [Kim and Kim, 2010]. Vascular space occupancy (VASO) MRI measures changes in CBV through extravascular tissue signal changes [Lu et al., 2003], based on the difference in blood T_1 and tissue T_1 . At high magnetic field strengths contrast-to-noise-ratio (CNR) is reduced due to convergence of tissue and blood T_1 values [Rooney et al., 2007]. To improve VASO CNR a slab-selective gradient is applied during inversion, such that fresh blood fills the small blood vessels in the imaging slice after it has been inverted only once [Jin and Kim, 2008]. This can be done at 7T because here blood arrival and transit times are comparable to the blood nulling time after inversion. To assess and eliminate blood oxygen dependent (BOLD) signal contamination, BOLD data are acquired interleaved with VASO. Measurements of the slab-selective, BOLD-corrected VASO are taken in human brain at 7T during a visual task. The high CNR of the developed method is reflected in stable and consistent results throughout all ten subjects. The measured average change in $\frac{\Delta CBV}{CBV_{rest}}$ of $28\% \pm 5\%$ is in good agreement with the literature [Belliveau et al., 1991]. Direct comparison of temporal and spatial properties of BOLD and VASO signal suggests the following. (a) The post stimulus return to baseline has a similar time constant for VASO and BOLD signals, contrasting with [Mandeville et al., 1999] but in agreement with [Dechent et al., 2010]. (b) Change in CBV is smaller in voxels closer to the pial surface, in contrast with BOLD [Kim and Kim, 2010]. In conclusion, it is shown that VASO can give reliable and consistent CBV changes at 7T. Slab-selective, BOLD-corrected VASO might become a useful tool for high resolution functional brain mapping in humans at high fields.

1 Introduction

Functional magnetic resonance imaging (fMRI) can map physiological correlates of neuronal activity in the brain in a non-invasive way. fMRI has become an indispensable tool for investigating brain function. One of the most popular fMRI techniques is based on the blood oxygenation level dependent (BOLD) contrast that is associated with changes in the energy consumption of brain tissue. However, BOLD is a compound measure of neural activity, depending on several physiological parameters namely cerebral blood flow (CBF), cerebral blood volume (CBV) and cerebral metabolic rate of oxygen (CMRO₂). An unexpected interplay of these parameters, e.g. in pharmacological or pathological studies, can disrupt the connection of BOLD to neural energy consumption. To better understand neural activation processes in the human brain it is essential to study direct physiological variables, such as CBV [Belliveau et al., 1991].

The transition to ultra high magnetic fields in MRI in the last decade allows sub-millimeter resolution mapping of neural activity changes. At this resolution the BOLD signal does not map changes in oxygenation at the site of neural activity only, but also downstream along vasculature [Turner, 2002]. CBV on the other hand is the physiological variable that is spatially more closely linked to neural activity than any other variable that can be measured with MRI [Kim and Kim, 2010] [Kennerley et al., 2010].

An fMRI technique known as vascular space occupancy (VASO) was devised to measure functional changes in CBV without the application of contrast agents [Lu et al., 2003]. The contrast based on the difference between tissue and blood T_1 is generated by manipulating the tissue magnetization prior to acquisition, such that blood water magnetization is nulled at the time of image acquisition, while keeping substantial tissue signal for detection. Relative changes of residual tissue signal are then associated with changes in CBV. At high magnetic field strengths remaining tissue signal is reduced due to convergence of tissue and blood T_1 values. Furthermore, increasing BOLD effect at high fields contaminates the VASO signal.

In this thesis a slab-selective, BOLD-corrected VASO sequence is implemented that counteracts the low signal and BOLD contamination. The challenges of the technique are evaluated and its advantages are validated both theoretically and experimentally. To convert VASO signal changes to changes in CBV, the grey matter signal contribution is determined for every voxel by means of a novel method that is based on the same MR sequence used in slab-selective, BOLD-corrected VASO.

The physical and physiological background knowledge necessary for this research is briefly reviewed in chapters 2 and 3. They will cover the behavior of magnetization in magnetic field, the principles of the imaging techniques used, the method to manipulate magnetization with adiabatic pulses and the physiological basis of neural activation. Chapter 4 reviews the fMRI methods BOLD and arterial spin labeling (ASL) that must be consid-

ered in order to understand the contrast of the VASO variant that is devised here. The ideas behind the slab-selective, BOLD-corrected VASO and its dependencies on different physiological parameters at high field are discussed in chapter 5.

To achieve proper slab-selective inversion despite large B_1 inhomogeneities and SAR limits, an adiabatic tr-FOCI inversion pulse is implemented, adapted, examined and validated in detail. During hyperoxia, the BOLD signal is believed to increase, while the vasculature remains constant. This is used to validate the developed BOLD correction scheme. These and other validations of the self-developed sequence are discussed in chapter 6. The experimental setup and the evaluation software are described in chapter 7. The experimental results and their discussion are covered in chapter 8.

2 Physical Basis

2.1 Magnetic Resonance (MR)

2.1.1 Spin in Magnetic Field

Quantum mechanical spin is a basic property of elementary particles such as protons. Zeeman coupling describes the energy of a spin in an external magnetic field in dependence of its orientation.

$$H = -\vec{\mu} \cdot \vec{B}_0 \quad (2.1)$$

Here H denotes the Hamiltonian corresponding to Zeeman coupling. $\vec{\mu}$ stands for the magnetic moment of the spin and \vec{B}_0 denotes the external static magnetic field. By solving the Schrödinger equation, the difference of energy states of a single proton can be obtained.

$$\Delta E = \gamma \hbar B_0 \stackrel{\text{Larmor}}{\hat{=}} \gamma \omega_0 \quad (2.2)$$

γ denotes the gyromagnetic ratio and ω_0 denotes the Larmor frequency. The energy states correspond to the orientation of the spin in the external magnetic field. Due to the low value of the reduced Planck constant \hbar , this energy difference is far below the thermal energy at room temperature. The distribution of energy states for a given temperature T is given by the Boltzmann distribution.

$$\frac{p_{up}}{p_{down}} = e^{-\frac{\Delta E}{k_B T}} \quad (2.3)$$

p_{up} , p_{down} are the probabilities of the spins to be oriented parallel or anti-parallel to the external magnetic field. The orientation along the external field is preferred with respect to energy. This results in a macroscopic net magnetization parallel to the external magnetic field. Eq. 2.3 suggests that the magnetization induced by the external magnetic field of 7T at room temperature is only $\approx \frac{1}{20,000}$ corresponding to the maximum magnetization. This magnetization induced by the alignment of nuclear spins in the external magnetic field is the source of signal in magnetic resonance.

2.1.2 Macroscopic Magnetization in RF Field

According to Larmor precession, an external magnetic field exerts a torque on any magnetic moment, such as the magnetization of an atomic nucleus \vec{M} .

$$\frac{d\vec{M}}{dt} = \gamma \vec{M} \times \vec{B} \quad (2.4)$$

In MR the magnetic fields consist of a time-constant strong field B_0 and a perpendicular oscillating field \vec{B}_1 that is induced by an RF antenna (often in coil shape). \vec{B}_1 is mostly adjusted to oscillate just with the Larmor frequency of the main magnetic field B_0 . Conventionally, the main magnetic field's direction \vec{B}_0 is designated by the +z direction. \vec{B}_1 is powered only for very short periods during an MR experiment. This polarized RF field $\vec{B}_1(t)$ can be described with equation 2.5.

$$\vec{B}_1(t) = \frac{1}{\sqrt{2}} B_1 \cdot [\cos(\omega_{RF}t)\hat{x} + \sin(\omega_{RF}t)\hat{y}] \quad (2.5)$$

Considering that the magnetic field is a superposition of B_0 and B_1 , equation 2.4 can be expressed as:

$$\frac{d\vec{M}}{dt} = \gamma \vec{M} \times \vec{B}_{eff} \quad (2.6)$$

$\vec{B}_{eff} = \vec{B}_0 + \vec{B}_1(t)$ is the so-called effective magnetic field. The magnetization precesses around this field with the effective Larmor frequency:

$$\omega_{eff} = \gamma B_{eff} \quad (2.7)$$

The mathematical description of the behavior of the magnetization \vec{M} can be simplified by transforming equation 2.6 into a rotating frame of reference. A useful relation for transforming a vector into a rotating frame of reference is equation 2.8 [Slichter, 1989].

$$\left(\frac{d\vec{p}(t)}{dt}\right)_{\text{lab}} = \left(\frac{d\vec{p}(t)}{dt}\right)_{\text{rot}} + \vec{\Omega} \times \vec{p}(t)$$

where $\vec{\Omega} = -\omega\hat{z}$ and ω denotes the angular velocity (2.8)

The equation of motion in the rotating frame is given by employing equation 2.8 in equation 2.6.

$$\begin{aligned} \left(\frac{d\vec{M}(t)}{dt}\right)_{\text{rot}} &= \left(\frac{d\vec{M}(t)}{dt}\right)_{\text{lab}} - \vec{\Omega} \times \vec{M} = \gamma \vec{M} \times \vec{B}_{eff} + \gamma \vec{M} \times \frac{\vec{\Omega}}{\gamma} = \\ &\underbrace{=}_{\vec{\Omega} = -\omega_0\hat{z}} \gamma \vec{M} \times \vec{B}_{eff} \end{aligned}$$

with B_{eff} in the rotating frame $\vec{B}_{eff} = \begin{pmatrix} B_1 \cos((\omega_{RF} - \omega)t) \\ -B_1 \sin((\omega_{RF} - \omega)t) \\ B_0 - \underbrace{\omega}_{\gamma} \\ = 0 \text{ on resonance} \end{pmatrix}$ (2.9)

On-resonance, the magnetization in the rotating frame of reference 'feels' no magnetic field in z-direction, but only a time constant B_1 field (see Eq. 2.9). In this picture, it is apparent that the influence of the RF field results in magnetization precession around an axis in the transverse plane. This precession can be used in MR experiments to flip the magnetization by an arbitrary angle θ .

$$\theta = \gamma \int_0^T B_1(t) dt \quad (2.10)$$

$B_1(t)$ is the amplitude of the RF magnetic field and T denotes the pulse duration. RF pulses that flip the magnetization into the transverse plane for subsequent data sampling are often called excitation pulses. RF pulses that invert the magnetization to evoke certain relaxation behavior are called inversion pulses.

The precessing magnetization is associated with an alternating magnetic field that induces electrical current and voltage in an RF coil. This current can be sampled and used for reconstruction of MR images. In order to provide a high signal to noise ratio and a relatively uniform RF field, coil arrays are built.

Relaxation

Spins cannot be assumed to be totally isolated. If spins are not in thermodynamic equilibrium with their surroundings, interactions via magnetic coupling bring them back into equilibrium. The mechanism by which magnetization comes into equilibrium can be described by two different relaxation mechanisms. (a) Longitudinal relaxation, associated with magnetization change perpendicular to the plane of precession and (b) transversal relaxation associated with magnetization change within the plane of precession. Longitudinal and transversal relaxation are characterized by the corresponding time constants T_1 and T_2 . These relaxation constants are highly dependent on the tissue properties and are mostly the basis of image contrast in MRI. T_1 -relaxation can be explained by energy transfer between single nuclei and the lattice they are embedded in. T_2 -relaxation can be considered as dephasing of initially coherently precessing magnetizations. This dephasing can be caused by magnetic interaction between adjacent nuclei. Additional dephasing can be caused by inhomogeneities in the external magnetic field e.g. caused by susceptibility variations and corresponding variations in Larmor frequency. The combined transversal relaxation of both extrinsic field variations and intrinsic dephasing caused by spin-spin interactions is referred to T_2^* -relaxation.

Bloch Equations

The total behavior of magnetization including precession and relaxation is described with the Bloch-equations:

$$\begin{aligned}\frac{dM_x(t)}{dt} &= \gamma(\vec{M}(t) \times \vec{B}(t))_x - \frac{M_x(t)}{T_2} \\ \frac{dM_y(t)}{dt} &= \gamma(\vec{M}(t) \times \vec{B}(t))_y - \frac{M_y(t)}{T_2} \\ \frac{dM_z(t)}{dt} &= \gamma(\vec{M}(t) \times \vec{B}(t))_z - \frac{M_z(t) - M_0}{T_1}\end{aligned}\tag{2.11}$$

2.2 Magnetic Resonance Imaging

Magnetic resonance imaging (MRI) is an imaging technique that utilizes material dependent magnetization density and its relaxation behavior to visualize detailed internal

structures of biological tissue. Magnetic field gradients cause magnetization at different locations to precess at different frequencies. Spatial encoding of magnetization can be obtained by providing gradients in three directions.

2.2.1 Data Acquisition

Transverse magnetization can be considered as

$$M_{x,y}(t) = e^{-i\omega t} e^{-\frac{t}{T_2}} M_{0\ x,y} \stackrel{\omega=\gamma B}{=} e^{-i\gamma B t} e^{-\frac{t}{T_2}} M_{0\ x,y} \quad (2.12)$$

This is a solution of the transversal components of equation 2.11. The magnetic field B in Eq. 2.12 can be considered a linear combination of a constant magnetic field B_0 and constant magnetic field gradients in all three spatial directions $B(x, y, z, t) = B_0 + xG_x(t) + yG_y(t) + zG_z(t)$. Including this in Eq. 2.12 gives:

$$M_{x,y}(x, y, z, t) = e^{-i\gamma B_0 t} e^{-i\gamma \int_0^t (xG_x(t') + yG_y(t') + zG_z(t')) dt'} e^{-\frac{t}{T_2}} M_{0\ x,y} \quad (2.13)$$

The measured MR signal $S(t)$ is given as a spatial summation of MR signal from every point in space.

$$S(t) = \int_x \int_y \int_z e^{-i\gamma B_0 t} e^{-i\gamma \int_0^t (xG_x(t') + yG_y(t') + zG_z(t')) dt'} e^{-\frac{t}{T_2}} M_{0\ x,y} dx dy dz \quad (2.14)$$

The aim in MRI is to convert the signal $S(t)$ into the spatial distribution of transversal magnetization $M_{x,y}(x, y, z, t)$. Therefore, the similarity of Eq. 2.14 to Fourier transformation is used and it can be rewritten to:

$$S(t) = \int_x \int_y \int_z M(x, y, z, t) e^{-i2\pi k_x x} e^{-i2\pi k_y y} e^{-i2\pi k_z z} dx dy dz$$

$$k_{x,y,z} = \frac{\gamma}{2\pi} \int_0^t G_{x,y,z}(t') dt' \quad (2.15)$$

When transversal magnetization is only localized in one slice, Eq. 2.15 can be simplified to a two dimensional Fourier transformation. To get an intuitive picture of the conversion of the temporally changing signal to the spatial magnetization distribution, the concept of k-space is most helpful. In MRI, the k-vector is navigated throughout the k-space along a sampling path by altering the different gradient parameters in time. In most imaging methods k-space is sampled line by line with constant velocity; i.e. during data sampling the gradient fields stay constant and the k-vector passes through the k-space with increasing time.

In conclusion, different spatial frequencies and phases that are induced by the gradient fields are utilized to localize the magnetization distribution in space.

2.2.2 Imaging

Conventionally, the x-direction is referred to read direction and the y-direction is referred to phase direction. In practice, the k-space is sampled in discrete steps. The MR signal generates a matrix of signal intensities for a discrete mesh of data points in k-space. To understand the conversion of the raw data from k-space, some features of Fourier transformation can be adopted, e.g. the larger the k-space is, the better the spatial resolution of the converted image becomes. And vice versa, the field of view (FOV) in the imaging space is defined with the sampling density in the k-space.

$$FOV_x = \frac{1}{\Delta k_x} \quad \text{for } G_x = \text{const} \quad \frac{2\pi}{\gamma G_x \Delta t}$$

$$\Delta x = \frac{1}{2k_{x \text{ max}}} \quad (2.16)$$

The acquired data are composed of the induced voltage in the RF coil and the phase of the precessing magnetization. Therefore, to convert the data from one plane in k-space into one plane in image space, a two dimensional complex Fourier transformation is used.

2.2.3 Pulse Sequence

A pulse sequence is a set of defined RF and gradient pulses, usually repeated many times during a scan session. An MR sequence controls the magnetization manipulation before and during data acquisition. In a sequence with periodically repeating RF pulses, the magnetization is approaching to a dynamically steady-state. This steady-state depends on the timing of inversion, excitation and relaxation.

Inversion Recovery

In this thesis an inversion recovery sequence will be of importance. An inversion recovery sequence is based on an RF pulse that inverts the z-magnetization before the magnetization is excited and the image is acquired. The magnetization can be sampled throughout its recovery to equilibrium. Inversion recovery sequences are suitable to look at T_1 based contrast. The time between inversion and data acquisition is called inversion time (TI). The time between two subsequent inversions is called repetition time (TR).

2.2.4 EPI

Data acquisition consists of an excitation pulse that is followed by changing gradients. The excitation is usually accompanied by a gradient in z-direction. A result of this so-called slice selective gradient is that only a thin slice of the sample is in resonance with the RF field. Therefore only that slice is excited. The gradients in x- and y-direction control dephasing and rephrasing of the precessing magnetizations, dependent on their location in the excited slice. In a classical line-by-line k-space acquisition, an excitation pulse is followed by a small dephasing gradient in y-direction. After that, a gradient

in x-direction dephases and rephases the magnetization associated with the sampling of a k-space line in k_x -direction. The rephasing with gradients induces so-called gradient echoes (GE). The whole procedure is repeated with different dephasing in y-direction, representing different lines in k-space.

Instead of measuring just one line in k-space after each excitation pulse, it is possible to acquire many lines. In echo planar imaging (EPI), k-space data are sampled throughout the k-space as long as the precessing magnetization in the transverse plane has not decayed away [Mansfield, 1977]. In EPI, the whole k-space can be acquired after a single excitation. A so-called sequence diagram of an EPI acquisition depicts the temporal interplay of RF field, gradient fields and data sampling of EPI acquisition (Fig.2.1).

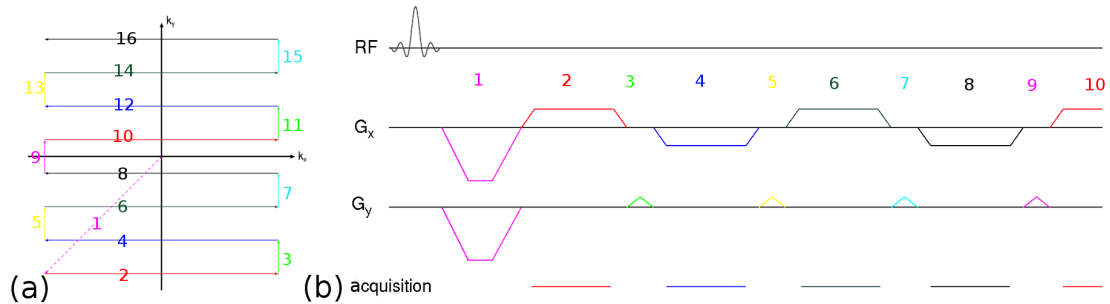


Figure 2.1: Sequence diagram and k-space data sampling in EPI. (a) depicts the trajectory in k-space in an EPI sequence. (b) depicts the corresponding RF pulse, the gradients and the readout. One can see that k-space data are sampled along lines in k_x -direction. Small blips in G_y drive the trajectory in k_y -direction.

The time it takes from the excitation pulse until the center of the k-space is reached is called echo time (TE). One of the biggest advantages in EPI is the possibility of fast speed with which large volumes are acquired. The induced voltage in the RF coil is a direct measure of the coherence of the precessing magnetization vectors. This voltage is sampled for a set of combination of x- and y-gradient moments, corresponding to points in k-space. The image is then reconstructed by means of Fourier transformation.

2.2.5 EPI Artifacts

Echo-planar imaging (EPI) is more sensitive to image artifacts than conventional imaging for two reasons. First, every second echo is acquired under a negative gradient. This can result in systematic phase errors between even and odd k-space lines. Second, the readout period in EPI is longer than in conventional imaging [Stehling et al., 1998].

Data points that are adjacent in read direction in k-space are sampled consecutively and the time difference between the sampling of these data points is relatively short. Data points that are adjacent in phase direction in k-space are not sampled consecutively and the time difference between the sampling of these data points is relatively long. During this long duration, even a small resonance frequency offset of magnetization can

accumulate a notable error in phase between acquisitions of different k-space lines. This makes EPI prone to off-resonance artifacts.

N/2 Ghosting N/2 ghosting (also known as Nyquist ghosting) is a problem unique to EPI. It is due to the fact that every second line in k-space is acquired under negative gradient. The alternation in scanning direction can lead to a systematic difference between even and odd lines in the k-space. A phase error that alternates between even and odd echoes in an EPI sequence can cause faint ghost images, shifted by half an image. Such phase errors in even or odd lines can be for example caused by current induction (eddy currents) in any conductive material within the gradient coils. The ghost appears only in the phase encoding direction, shifted by $N/2$ pixels, where N is the matrix dimension along the phase encoding direction. Fig. 2.2 shows schematically an extreme case of N/2 Ghost.

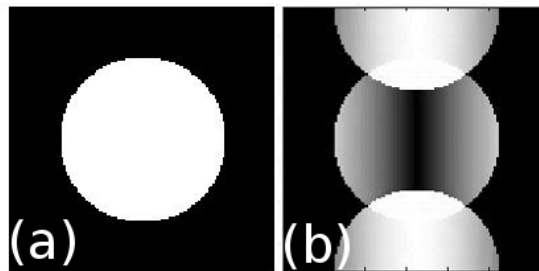


Figure 2.2: Simulated N/2 ghosting. The reference image is depicted in (a) and the ghost artifact is depicted in (b). To generate this image, every second line of the k-space data of Fig. 2.2 (a) is shifted by $\frac{1}{128}$ of the k-space. The matrix size is 128×128 . The simulation program is implemented in matlab (version 7.11, Mathworks, Natic, MA, USA).

In order to minimize N/2 Ghosting, the phase error between even and odd lines is usually determined during the scan.

T_2^* Blurring In EPI the MR image can not be considered as a snapshot of the distribution of transverse magnetization at one point in time. Some time is required to allow the applied gradients to induce local phase changes which correspond to the sampling in k-space. During this image acquisition T_2^* relaxation effects alter the signal. Since the important k-space data points are in the center of the k-space, it is reasonable to acquire the k-space data in the center of the k-space at the beginning of the sampling period. Since the size of the acquired k-space corresponds to the resolution in the image-space (see Eq. 2.16), the outer k-space lines contain the information of the high-resolution contrast. In sampling paths that acquire the outer k-space lines after the inner k-space lines, T_2^* relaxations causes loss of resolution in imaging space. An effective way to address this T_2^* -induced blurring is to restrict the acquisition of k-space data to a narrow time

window in which T_2^* decay is not substantial. The acquisition time can be reduced e.g. with higher gradients or so-called partial Fourier acquisition.

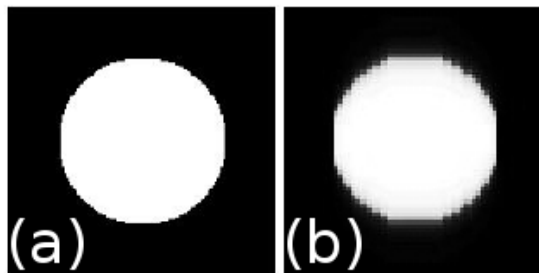


Figure 2.3: Simulated blurring due to T_2^* relaxation. The reference image is depicted in (a). Image (b) is generated with a simulated T_2^* decay of $T_2^* = \frac{1}{4} \times$ read-out duration. Simulation program is implemented in matlab (version 7.11, Mathworks, Natic, MA, USA).

T_2^* relaxation reduces the intensity of off-center k-space data points that are acquired at the end. Since the off-center data points in the k-space represent the regions of sharp contrast, Fig. 2.3 (b) has a lower spatial resolution.

Partial Fourier

A nice feature of Fourier transformation is the symmetry property. If the object is real, its Fourier transform is hermitian:

$$S(k_x, k_y, k_z) = S^*(-k_x, -k_y, -k_z) \quad (2.17)$$

Thus, only one half of k-space is needed to reconstruct a real object. In two dimensional k-space, theoretically only a quadrant of the sampled k-space is needed to fill the complete k-space. In reality unwanted phase shifts cause the reconstructed object to be complex, instead of being purely real. Such unwanted phase shifts can arise from motion, resonance frequency offsets, hardware group delays, eddy currents and receive B_1 field inhomogeneity [Bernstein et al., 2004]. Therefore, more than 50% of k-space is always sampled. In partial Fourier acquisition SNR is reduced up to a factor of $\frac{1}{\sqrt{2}}$. The reduction of noise without partial Fourier comes from the fact that noise is random. Noise from one half of k-space is independent of noise from the other half of the k-space, but the signal is the same in both segments of the k-space. In partial Fourier acquisition, noise from one half of k-space is copied with the signal to the second half of the k-space and will reduce the SNR when the image is created.

The advantage in partial Fourier acquisition is the reduced acquisition time. In partial Fourier acquisition the acquired slices per unit time can be increased up to a factor of 50% and TE can be reduced substantially.

Off-resonance Effects There are three phenomena that can be summarized as off-resonance effects: intra-voxel dephasing of magnetization vectors, chemical shift and image distortion [Stehling et al., 1998].

To begin with intra-voxel dephasing, magnetic susceptibility variations (e.g. at tissue-air interfaces) can cause a signal void in this region. A larger voxel lying in this intrinsic field gradient will include a wider range of frequencies, which will produce a shorter T_2^* . In contrast to the voxel dependent SNR considerations (see section 2.2.6) this intra-voxel dephasing effect suggests the use of thinner slices.

The chemical shift effect results from the different partial shielding of the nucleus by different electronic molecular orbitals of the chemical elements. For example, when placed in the same magnetic field B_0 , H nuclei in lipids feel a slightly different magnetic field than H nuclei in water. Consequently their Larmor frequency differs. In EPI, phase offsets from off-resonance effects are not reset before each phase encoding pulse (in contrast with conventional multi-shot acquisitions). Since the phase encoding gradient blips are spread throughout the data acquisition course, there is time for substantial unwanted phase offsets to accumulate. For EPI, chemical shift artifacts are thus predominant in the phase encoding direction. Due to this chemical shift, fat suppression is essential in EPI [Bernstein et al., 2004]. Off-resonant fat artifacts are often suppressed with a 90° RF pulse at the resonance of fat and a dephasing gradient prior to the image acquisition. Due to the susceptibility of the body, the magnetic field B_0 experiences local changes. Shim devices consisting of gradient coils in the scanner are used to maintain the homogeneity of the magnetic field. Even in a well-shimmed magnet, the human head will magnetize unevenly so that the B_0 magnetic field may differ from point to point. The corresponding small frequency differences result in spatial displacement of the signal in the resulting images. These distortions in EPI images occur mainly in phase encoding direction due to the long time difference between the sampling of k-space lines. The magnitude of the distortions in EPI images is proportional to the main magnetic field and to the total acquisition time. Thus the distortions can be minimized by decreasing the acquisition time. Another approach is to acquire the slices parallel to the brain base, in order to avoid magnetic inhomogeneities due to tissue dependent susceptibility variations.

2.2.6 Signal to Noise Ratio

The signal to noise ratio (SNR) is defined as $SNR := \frac{\text{mean signal value}}{\text{standard deviation of the signal}}$.

The magnetic field strength makes a direct impact on the signal quality of the acquired data. According to the Boltzmann distribution, the number of spins that contribute to the induced magnetization in an external field is approximately proportional to the main field strength. According to Faraday's law of induction, the voltage in the RF coil induced by the precessing magnetization is proportional to the frequency. Hence, signal increases with the square of the magnetic field. On the other hand, thermal noise increases linearly with frequency [Edelstein et al., 1986]. Consequently, $SNR \propto B$. This can explain the quest for higher magnetic field strengths in recent decades.

In fMRI studies, there are two primary sources of noise: thermal noise and physiological

noise. The class of noise that can be detected with a brain like phantom is called thermal noise. In MRI, a phantom is an artificial object of known size and composition that is imaged to test an MRI system or a sequence. Thermal noise comes about primarily from fluctuating stray currents in the sample, which create random currents in the detector coil (thermal noise) [Edelstein et al., 1986]. Thermal noise is completely caused by the experimental setup.

The additional signal fluctuation, which can be detected in a resting living brain, is called physiological noise. Physiological noise is primarily caused by the movement of the body due to respiration or heartbeat. In addition susceptibility variations due to neural activity in the resting brain can result in physiological noise. At 7 Tesla the physiological noise is dominated by changes of the magnetic field due to respiration movements.

In addition to SNR, temporal signal-to-noise ratio (tSNR) is a useful measure of image time course stability. It can be determined by dividing the mean of a time series by its standard deviation. SNR is proportional to the voxel volume, but tSNR is not directly proportional to the voxel volume [Murphy et al., 2007]. Typical values for SNR in common MRI images are around 90-100.

2.2.7 Specific Absorption Rate

Every RF pulse deposits energy in the body. The rate of energy deposition is called specific absorption rate (SAR). SAR is continuously monitored during an MR experiment to prevent any violations of legal limits. The energy of an RF pulse depends on the square of the RF amplitude and the electrical conductivity. Since the induced electric field in the tissue is $\propto \omega^2$, SAR increases with higher field strengths quadratically. Energy deposition results from induced currents in the tissue and is associated with heating of the tissue. EPI sequences are not significantly limited by SAR constraints because they acquire an entire slice after one excitation pulse.

2.3 Adiabatic Inversion

2.3.1 Resistance of Adiabatic Pulses Against B_1 -Inhomogeneities at High Fields

With the advent of ultrahigh magnetic fields, RF interactions with the human body become a critical challenge. When RF wavelength approaches the size of the target object, diffraction and interference effects of RF travelling waves emerge. For example, human head images acquired at 7 Tesla with a volume coil display a stronger signal intensity at the center than in the periphery [Vaughan et al., 2001]. For conventional RF pulses, the flip angle is directly proportional to the B_1 magnitude ($\theta = \gamma \int_0^T B_1(t) dt$ see Eq. 2.10).

Hence, the local dependence of the B_1 magnitude and the flip angle respectively influence the signal intensity, as well as the spatial dependence of steady-state of magnetization. The extent of the interference can be governed by dielectric properties.

Due to these inhomogeneities, the flip angle can vary strongly within the imaged sample.

In VASO it is essential to obtain full magnetization inversion independent of B_1 inhomogeneities. To achieve this, a B_1 -independent adiabatic inversion pulse is implemented and examined in this thesis.

Adiabatic inversion [Abraham, 1961] is a method of inverting magnetization by means of specific RF pulses. Adiabatic pulses are fundamentally different from conventional RF pulses used in MRI. Once the RF amplitude exceeds a certain threshold, the flip angle of this adiabatic inversion pulse is independent of B_1 . In contrast to non-adiabatic RF pulses, adiabatic pulses do not obey the relationship between the flip angle and the B_1 field amplitude, described by equation 2.10. Instead, the flip angle of an adiabatic pulse depends on how the B_1 field varies its amplitude and frequency (the phase respectively) during the pulse. An adiabatic inversion pulse duration is in the order of $5ms$ - $20ms$ [Conolly et al., 1991] [Hurley et al., 2010]. They are therewith much longer than conventional pulses, which are mostly shorter than $10ms$. Since adiabatic pulses last longer, they typically require much more RF power than their non-adiabatic counterparts. With this in mind, adiabatic inversion is accompanied with higher SAR values.

Adiabatic inversion is achieved by simultaneously modulating the amplitude and frequency of an RF pulse so that the orientation of the effective magnetic field B_{eff} changes its direction from $+\hat{z}$ to the $-\hat{z}$ axis. In an effective external magnetic field \vec{B}_{eff} , the magnetization precesses along the surface of a cone around the field direction (see equation 2.6). Due to an additional RF field, the direction of B_{eff} and hence the axis of the “cone of precession” can be altered. The “cone of precession” orients rather parallel to \vec{B}_0 if the irradiated RF field is below resonance, and rather anti-parallel if RF field is above resonance. Hence, in the rotating frame of reference, the frequency of an adiabatic inversion RF pulse starts with a large negative value (below resonance), gradually increases to 0 (on-resonance) and ends at a large positive value (above resonance), or vice versa. The frequency modulation function, often defined as

$$\Delta\omega \equiv \omega_{Larmor} - \omega_{RF} \quad , \quad (2.18)$$

behaves in the reversed way. In contrast, the amplitude modulation function begins with a value of 0, increases to its maximum, and decreases to 0 again at the end of the pulse. The two biggest advantages of adiabatic inversion are high inversion efficiency and comparatively high immunity against inhomogeneities of the magnetic field. These advantages suggest the application of adiabatic inversion pulses at ultra high fields, since field inhomogeneities can lead to artifacts and severe problems.

Phantoms

It is helpful to examine the performance of an RF pulse and its dependencies on magnetic and electric susceptibilities of the sample with so-called phantoms. Phantoms are man-made objects approximately in the shape of a human head with specially designed electrical and magnetic susceptibility properties. They are often made of spherical bottles filled with fluids.

In a phantom with high conductivity (high NaCl content respectively) the RF-field is damped and RF-fields of adjacent coil elements interfere more strongly than RF-fields of

opposing coil elements. This leads to a strong central brightening effect in samples with high conductivity [van de Moortele et al., 2005].

Oil has relatively small permittivity ϵ . This yields to relatively large RF-wave length λ :

$$\lambda \propto \frac{1}{n} \propto \frac{1}{\sqrt{\epsilon}} \quad , \quad (2.19)$$

where n denotes the refractive index. Apart from this, oil has very low conductivity and respectively the central bright effect is reduced. For this reason oil phantoms have been used in order to determine the behavior of the scanner independent of B_1 inhomogeneities. In order to examine the performance of the developed sequences in human like tissue, agar phantoms are used. Phantoms made of agar, NaCl and distilled water can be designed to have material-dependent properties similar to the human head.

2.3.2 Constrains for Adiabatic Inversion

In the laboratory frame the magnetization \vec{M} precesses around the effective magnetic field \vec{B}_{eff} on the surface of a cone. If this \vec{B}_{eff} changes its direction very slowly, the cone of precession follows the effective magnetic field.

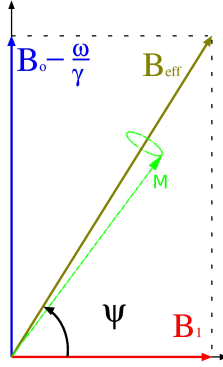


Figure 2.4: Visualization of ψ

In accordance to Fig. 2.4, the angle between \vec{B}_{eff} and \vec{B}_1 can be derived with

$$\psi = \arctan \left[\frac{B_0 - \frac{\omega}{\gamma}}{B_1} \right] = \arctan \left[\frac{B_{z\ eff}}{B_1} \right] \quad (2.20)$$

Adiabatic pulses operate under the adiabatic principle, which states that the magnetization vector \vec{M} follows the direction of the effective magnetic field \vec{B}_{eff} . This is only true if the direction of \vec{B}_{eff} does not change much during one period of precession of the magnetization around \vec{B}_{eff} [Bernstein et al., 2004]. This is known as the adiabatic condition.

$$\left| \frac{d\psi}{dt} \right| \ll \gamma \left| \vec{B}_{eff} \right| \quad (2.21)$$

The adiabaticity β is a measure of how the adiabatic condition is fulfilled.

$$\beta = \frac{|\gamma \vec{B}_{eff}|}{\left| \frac{d\psi}{dt} \right|} \quad (2.22)$$

The adiabatic condition is met for $\beta \gg 1$.

Furthermore, relaxation effects should be negligible for the duration of the adiabatic pulse τ . Since T_1 is always larger than T_2 we can write this condition as:

$$\tau \ll T_2 \quad (2.23)$$

2.3.3 Design of Adiabatic Inversion Pulses in MRI

In this MRI study, adiabatic pulses are utilized to affect the magnetization in a spatially restricted area. Several types of adiabatic pulsed have been designed so that the adiabatic condition is only met for a sharp band of resonance frequencies. If the pulse is accompanied with a gradient field, the sharp band corresponds to a sharp slab perpendicular to the gradient in which the magnetization is affected by the pulse.

Silver Pulse In 1984 Silver et al. [Silver et al., 1984] showed analytically that, above a critical power threshold, the magnetization is inverted over a relatively sharply defined bandwidth using hyperbolic secant shape as a driving function. This hyperbolic secant or sech pulse has the complex form

$$\tilde{B}_1(t) = B_1^0 (\text{sech}(\beta t))^{1+i\mu} = B_1^0 \text{sech}(\beta t) e^{i\mu \ln(\text{sech}(\beta t))} \quad (2.24)$$

or

$$\begin{aligned} B_1(t) &= B_1^0 \text{sech}(\beta t) \\ \phi(t) &= \mu \ln(\text{sech}(\beta t)) \\ \Delta\omega(t) &= -\mu\beta \tanh(\beta t) \end{aligned} \quad (2.25)$$

Equation 2.25 characterizes the RF field of an adiabatic pulse in the rotation frame of reference in cylindrical coordinates. B_1 denotes the transverse component of the effective magnetic field of the RF pulse, $\phi(t)$ denotes the orientation of B_1 in the transverse plane and $\frac{\Delta\omega(t)}{\gamma}$ denotes the z-component of the effective magnetic RF field. The parameters μ and β define the temporal and frequency dependent properties of the pulse.

VR Pulse A spatially selective RF pulse that is played concurrently with a time-varying gradient is called variable rate (VR) pulse [Conolly et al., 1988]. VR pulses are also known as variable-rate selective excitation (VERSE) pulses [Bernstein et al., 2004]. Since the SAR value of a pulse is proportional to the square of its B_1 amplitude (see section 2.2.7), the peak of the pulse typically contributes mostly to the total power deposition. VR pulses reduce the RF power deposition by decreasing the RF amplitude in the vicinity of the peak of the pulse. In order to maintain the adiabatic condition, the pulse is stretched in time. To maintain the consistent sharpness of the inversion profile of the pulse, the gradient amplitude is reduced in the stretched area of the RF pulse.

FOCI Pulse In 1996 it was shown that the sharpness of the inversion can be dramatically improved by modifying the secans hyperbolicus pulse shape of the amplitude [Ordidge et al., 1996]. Correspondingly, the gradient waveform is modulated during the selective inversion. With these so-called frequency offset corrected inversion (FOCI) pulses the inversion profile can be improved without increasing the RF power. The FOCI-optimized modulation functions are based on the standard hyperbolic secant pulse. The RF amplitude $B_1(t)$, the gradient strength $G(t)$ and the resonance frequency offset $\Delta\omega$ are obtained by multiplying the standard secant modulation functions with a shaping function $A(t)$.

$$\begin{aligned} B_1(t) &= A(t) * B_1^0 \operatorname{sech}(\beta t) \\ G(t) &= A(t) * G_s \\ \Delta\omega(t) &= -A(t) * \mu\beta \tanh(\beta t) \end{aligned} \tag{2.26}$$

G_s is the time constant slice selective gradient corresponding to a hyperbolic secant pulse. $A(t)$ reshapes all the modulation functions. $A(t)$ starts at high values at the beginning of the pulse, decreases halfway through the pulse and increases again in the second half of the pulse.

tr-FOCI Pulse In 2010 Hurley et al. [Hurley et al., 2010] combined the improved slice profile of FOCI pulses with a better B_1 insensitivity, associated with a good selective inversion efficiency. These numerically optimized adiabatic inversion pulses were tailored specifically for magnetization inversion at ultrahigh fields (7T), where large B_1 inhomogeneities can occur. Hurley et al. introduced a time resampling function $T(t)$ for optimization of the pulse. The time resampling function $T(t)$ is defined to be monotonically increasing:

$$\begin{aligned} B_1(t) &= A(t) \operatorname{sech}(\beta T(t)) \\ \Delta\omega(t) &= -A(t) \mu\beta \tanh(\beta T(t)) \\ G(t) &= A(t) G_s \end{aligned} \tag{2.27}$$

this leads to a bandwidth of

$$\Delta\omega_{max} = 2A(t=0) \mu\beta \tag{2.28}$$

Since the time dependence of the modulation functions are resampled (i.e. $B_1(t) \propto \operatorname{sech}(\beta t) \rightarrow B_1(T(t)) \propto \operatorname{sech}(\beta T(t))$), this pulse is called time resampled- (tr-) FOCI pulse. The precise modulation functions are extremely cumbersome and can be looked up in [Hurley et al., 2010].

It was shown that reducing the length T of the pulse, time resampled (tr)-FOCI pulses maintained a relatively sharp slab profile and relatively good resistance against RF inhomogeneities, compared to non-resampled FOCI pulses or hyperbolic secant pulses respectively [Hurley et al., 2010]. Thus, tr-FOCI pulses can maintain the same beneficial

features as non-resampled FOCI-pulses or hyperbolic secant pulses with reduced pulse durations and correspondingly low SAR values. Fig. 2.5 shows the shapes of the gradient and amplitude modulation functions as well as the frequency sweep of an inversion pulse with 200 mm slab thickness. This pulse has a duration of $5ms$.

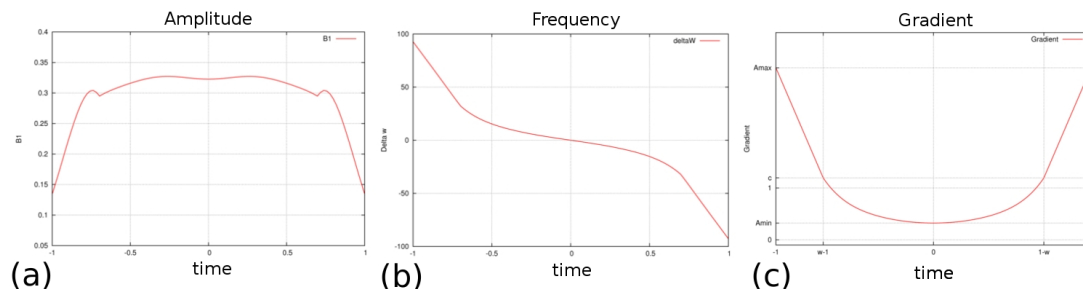


Figure 2.5: Modulation functions of a tr-FOCI pulse. Amplitude B_1 (a), frequency (b) and gradient (c). Function parameters are taken from [Hurley et al., 2010]

One can see in Fig. 2.5 (a) that the RF amplitude has a shape that is only remotely related to a hyperbolic secant pulse. The depicted RF shape is rather flat once it reaches a certain amplitude. The omission of a further increase in the amplitude is compensated for by increasing the pulse length. In order to keep the pulse bandwidth and the inversion slab thickness unchanged during the stretched period, the gradient (Fig. 2.5 (c)) is decreased simultaneously. Regarding the frequency sweep (Fig. 2.5 (b)), one can see that the modulation function is remotely based on a hyperbolic tangent function. It should be emphasized that the rate of change of the frequency offset is lower halfway through the pulse. At the center of the pulse, the RF frequency $\omega_{rf} = \omega_0 + \Delta\omega$ is close to the Larmor frequency ω_0 . Hence, the effective magnetic field B_{eff} in the rotating frame of reference consists only of the rather small B_1 contribution (Eq. 2.9). In order to fulfil the adiabatic condition (Eq. 2.21), the frequency offset change occurs relatively slowly along the middle of the pulse.

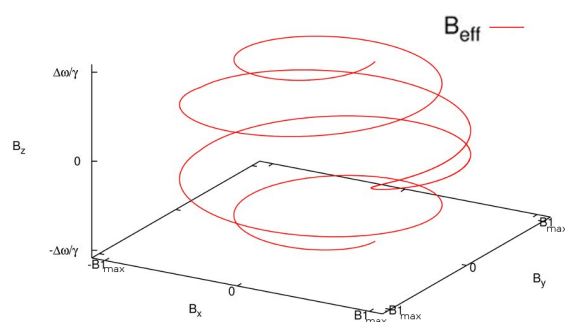


Figure 2.6: Trajectory of the effective magnetic field of the tr-FOCI pulse in the rotating frame of reference.

The temporal behavior of the magnetization and the inversion efficiency of this specific adiabatic inversion pulse (see Fig. 2.5) has been simulated. The simulation was done for two reasons, (a) to validate the implemented sampling functions and (b) to find a suitable set of pulse parameters that fulfil the requirements of this study. The simulated inversion profile is shown in Fig. 2.7 (a). For the sake of comparison, the simulated inversion profile of a hyperbolic secant pulse is depicted in Fig. 2.7 (b).

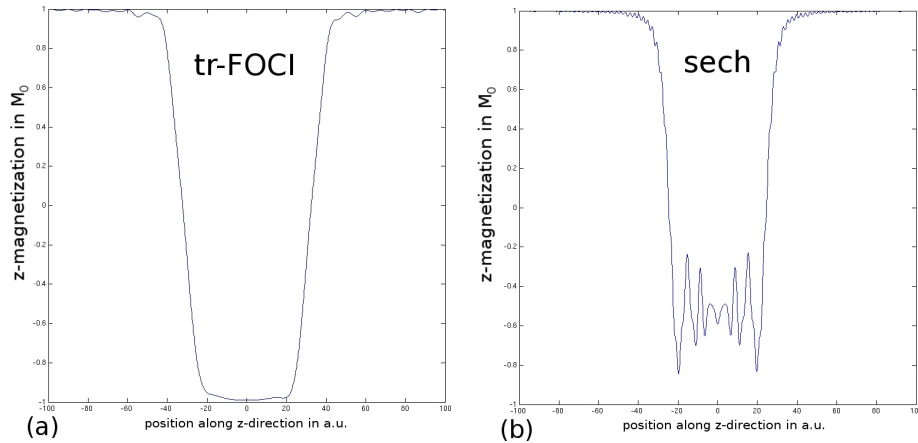


Figure 2.7: Simulated inversion profile of the tr-FOCI pulse in (a) and a hyperbolic secant pulse in (b). The abscissa is in arbitrary units and the ordinate is in units of M_0 . The simulation code used is based on the Bloch equations (Eq. 2.11) and written inhouse by Markus Streicher according to [Helgstrand et al., 2000].

It is apparent in Fig. 2.7 that the inversion efficiency is higher with the tr-FOCI pulse than with the secans hyperbolicus pulse. The maximum of the RF amplitude is the same for both pulses.

3 Physiological Basis

3.1 Neural Activity and Brain Metabolism

To understand the change of the physiological variables in an activated state, the basic biological mechanisms of neural activity and its constituents is discussed. The following section gives, a brief review of the relevant brain physiology, followed by a discussion of the mechanisms and indicators for neural activity. The focus is on the physiology that is important for fMRI, such as VASO.

3.1.1 Neurons

Neurons are the basic units of the brain for processing information. A neuron consists of three parts; a soma, dendrites and an axon. The soma is the cell body. It contains mitochondria and a nucleus. The dendrites are responsible for the reception of electrical impulses (action potentials) on synapses and the forwarding of these impulses to the soma. The axon transmits the action potentials from the soma to other neurons. A synapse is where the end of an axon (pre-synapse) comes into contact with a dendrite (post-synapse) of another neuron. At rest there is a potential difference ($\approx -70mV$) between the intracellular and the extracellular space of a neuron. This potential is caused by an imbalance of the ionic concentration between the intracellular and the extracellular space. So-called ion-pumps carry Na^+ and Ca^{++} from the cytoplasm into the extracellular space and K^+ from the extracellular space into the inside of the cells. After a transmitted action potential the ion-pumps are needed to restore the concentration gradient, so the neuron becomes excitable again.

3.1.2 Cerebral Blood Vessels

The blood flow through the capillaries provides the brain tissue with important nutrients such as O_2 and glucose. O_2 -enriched blood enters the vascular tree through the big arteries, the smaller arterioles and tiny capillaries. In the smaller vessels the blood releases nutrients and gathers byproducts such as CO_2 . The blood leaves the brain via the small venules and the larger veins. In capillaries the exchange of nutrients, byproducts and water occur. They have the dimension of red blood cells, so their diameter is about $\approx 8\mu m$. Capillaries are surrounded by the blood brain barrier consisting of endothelial cells.

The active control of dilation and constriction of the vasculature is fairly elaborate and not completely understood. Arteries and arterioles are surrounded with a coat of smooth

muscle cells that can cause the vasculature to constrict and dilate. The vascular resistance and flow of blood can be altered respectively. Capillaries are also believed to actively control blood flow and volume. Pericytes, which are apposed to capillaries and contain contractile proteins dilate and contract the vessel in response to different stimuli in the brain [Peppiatt and Attwell, 2004] [Harrison et al., 2002]. Astrocytes can cause smooth muscle cells to dilate with K^+ release that is triggered by synaptic activity [Gordon et al., 2011]. The coat of endothelial cells around the capillaries seem to play an important role in control of cerebral circulation by tonically releasing NO, which is important in maintaining vascular tone [Peppiatt and Attwell, 2004] [Anderson et al., 2006]. There are several vasoactive agents that change the flow rate of the vessels [Buxton, 2009]. In fMRI, CO_2 is a vasodilator that plays a special role. Artificially induced hypercapnia is often used to manipulate vasculature. CO_2 passes the blood brain barrier easily. It produces an acid environment, which causes dilation of brain arterioles. Hence breathing air with a moderate increased CO_2 concentration increases CBF and CBV without any significant change in metabolism [Chen and Pike, 2010a].

3.1.3 Perfusion of the Brain at Rest and During Activation

The understanding of the signals originating from noninvasive functional neuroimaging modalities such as fMRI relies on a profound knowledge of the cerebrovascular structure. Capillaries are often defined on the basis of a diameter threshold. Vessels with diameters $< 8\mu m$ are often considered to be capillaries [Weber et al., 2008] [Villringer et al., 1994] [Pawlik et al., 1981]. The capillary volume fraction in the cortex is in the range of 2.2% ($\pm 0.5\%$), dependent on the cortical layer. Values in this range were found with optical methods in cats [Pawlik et al., 1981], in rats [Villringer et al., 1994] and in macaques [Weber et al., 2008]. The local capillary density correlates strongly with the steady-state metabolic demand. The mean inter-capillary distance is approximately 20 – 30 μm [Pawlik et al., 1981]. The precise values of red blood cell velocity in the capillaries, measured with optical methods are not consistent throughout the literature. Villringer et al. found a blood cell velocity of $\approx 0.5mm/s$ and an increase to $\approx 0.8mm/s$ during hypercapnia in anesthetized rats. In unanesthetized rats a baseline value of $\approx 0.8mm/s$ was measured [Ivanov et al., 1981]. Pawlik et al. measures a mean red cell velocity of 1.5 mm/s [Pawlik et al., 1981]. This suggests that a capillary with a typical length of $\approx 0.5mm$ is completely refilled after $\approx 1s$.

Most results suggest that opening and closing of capillaries (capillary recruitment) is not a means for regulating cerebral blood flow. Pawlik et al. [Pawlik et al., 1981] showed that at least 90% of all visible microvessels are continuously perfused with red cells. Both Kuschinsky et al. [Kuschinsky, 1996] and Villringer et al. [Villringer et al., 1994] confirm that all existing capillaries are plasma perfused and suggest that the changes in blood cell velocity within this perfused capillaries are most important in adapting cerebral flow to different needs. However, Villringer reports an incomplete ($\approx 90\%$) congruence of existing plasma-perfused and blood cell-perfused capillaries [Villringer et al., 1994].

A capillary diameter increase from $4.9 \pm 0.3\mu m$ up to $5.9 \pm 0.1\mu m$ as a response to hypercapnia is measured by Duelli and Kuschinsky [Duelli and Kuschinsky, 1993]. Villringer et

al. measured only a vessel diameter increase from $5.3 \pm 0.8 \mu\text{m}$ to $5.7 \pm 0.8 \mu\text{m}$. These diameter increases correspond to a capillary CBV increase of $30 \pm 25\%$ or $16 \pm 24\%$, respectively. For local regulation of blood flow during activation, vessels larger than $100 \mu\text{m} - 200 \mu\text{m}$ are believed to be insignificant [Kuschinsky, 2000]. Lee et al. report that only arteries smaller than $\approx 50 \mu\text{m}$ and venules smaller than $\approx 80 \mu\text{m}$ contribute to stimulus-induced change in CBV [Lee et al., 2001]. The fact that changes in CBV are believed to be caused only by microvessels suggests that CBV has a good focal co-localization with the underlying neural activity. Recently, high resolution fMRI confirmed good focal co-localization with neural activity of CBV up to a resolution of $78 \times 78 \times 500 \mu\text{m}$ [Wang et al., 2011a].

3.2 Physiological Variables

There are several indirect MRI techniques for measuring neural activity. All are based on the assumption that local metabolic activity correlates strongly with neural activity. This thesis considers neural activity to be the energy consumption of brain tissue. Some of the most important physiological variables indicating neural activity in MRI are:

- Cerebral Blood Flow (CBF): Flow of cerebral blood in ml per gram tissue per minute.
- Cerebral Blood Volume (CBV): Volume of blood within the skull.
- Cerebral Metabolic Rate of Glucose (CMRGlc): Moles of glucose metabolized per gram of tissue per minute.
- Cerebral Metabolic Rate of O_2 (CMRO₂): Moles of O_2 metabolized per gram of tissue per minute.
- Oxygen Extraction Fraction (OEF): Fraction of delivered O_2 that leaves the blood.
- Oxygenation Level: Relative density of oxygenated hemoglobin in the blood.

CMRGlc

Blood delivers glucose to the brain. Glucose is transported in a passive way from the capillaries into the tissue through so-called facilitated diffusion. Glucose simply diffuses down the gradient from higher concentration in the blood to lower concentration in the tissue. CMRGlc can be measured in PET studies. Here radioactive nuclei are attached to glucose and injected into the blood stream. The radioactive nuclei can be traced inside the brain. There is a well-established connection between local activity and CMRGlc in stimulated regions in the brain.

CMRO₂

Blood delivers oxygen to brain tissue. Only a small fraction ($\approx 2\%$) of oxygen is transported as dissolved gas. The bulk of oxygen carried is bound to hemoglobin. These two pools of oxygen are in dynamic equilibrium. The oxygen delivered to the tissue comes from the dissolved fraction. The metabolic rate of oxygen can also be measured via PET scans. CMRO₂ can be indirectly measured through calibrated BOLD signal as well.

CBF

CBF delivers nutrients to the brain tissue. In the adult resting brain approximately $50ml$ blood flows through $100g$ of tissue per min . CBF can be controlled by the diameter of the vessels. CBF change in arterioles and capillaries is modulated by change of their cross-section. CBF in venules and veins on the other hand seem to be associated with increase of flow velocity [Hillman et al., 2007] and no change in diameter. The influence of the diameter of the vessels can also be considered in the cerebral vascular resistance (CVR). This CVR is dominated by the capillaries rather than by arterioles or venules. In addition to CVR, CBF is strongly dependent on the pressure difference (ΔP) between the arterial and the venous blood. CBF can be considered as:

$$CBF = \frac{\Delta P}{CVR} \quad (3.1)$$

Auto-regulation of CBF leads to a remarkably constant level of CBF, even if the pressure ΔP varies between $75 - 175mmHg$ [Buxton, 2009].

According to Hagen-Poiseuille's Law; CBF can be written as:

$$\widehat{\dot{V}} \text{ Volume per second} = \frac{\pi r^4 \Delta P}{8\eta l} \propto r^4 \quad (3.2)$$

Where ΔP is the pressure difference, η is the dynamic fluid viscosity and l denotes the length of the blood vessel [Krieger, 2010].

In the stimulated brain CBF increases with the increase in CMRGlc. However, this does not mean that there is a causal link. CBF seems to increase much more during activation than CMRO₂ [Fox, 1986]. CBF can be directly measured with arterial spin labeling (see section 4.1).

CBV

CBV of the healthy adult brain is about 4% of the whole volume inside the skull [Grubb et al., 1974]. Considering blood vessels as cylindrical pipes, CBV of one vessel can be estimated as

$$Vol \propto r^2 \quad (3.3)$$

Increase of neural activity correlates to a moderate increase in CBV [Buxton, 2010].

Compensation of Dynamic change in CBV The Monro-Kellie doctrine states that cranial compartments are incompressible and that total volume inside the cranium remains constant. Hence, volume increase of one compartment of the brain must be compensated by a decrease in volume of another cranial component [Kelly, 1824]. During Hypercapnia (6% CO₂ breathing gas) the cerebral volume of heamoglobin can increase by 30% [Rostrup et al., 2005]. This would imply a total CBV increase of $\approx 30ml$. It has been

shown that even a small bolus injection of fluid into cerebral spinal fluid (CSF) space of $4ml$ can cause a temporary doubling of intracranial pressure [Czosnyka et al., 2004], which poses a health risk. This strongly suggests that a functional increase in CBV is not only compensated by the volume of CSF. It has been proposed that the increase in CBV happens through exchange of water between the capillaries and the endothelial cells surrounding them [Turner and Thomas, 2007], as well as water exchange between intravascular space and tissue. Since endothelial cells occupy up to 20% of the volume inside the vessel wall, volume decrease of endothelial cells can result in CBV increase. This increase could be a result of the endothelial cells draining intracellular water under activation (or hypercapnia). Hence, CBV can increase without an increase of intracranial pressure. A model was recently introduced that explains the volume increase of the capillaries while the bulk volume remains constant, in reference to the permeability of the capillary walls [Krieger, 2010]. However, MRI measurements in humans during stimulation and during hypercapnia suggest that there is a minor change in CSF in the range of $\approx 10\%$ [Donahue et al., 2006] [Piechnik et al., 2009] [Scouten and Constable, 2008].

Connection between CBF and CBV

In the healthy brain CBV and CBF are believed to be well correlated [Grubb et al., 1974]. This correlation is potentially complicated. CBF does not only depend on CBV, but also on the blood velocity and the numbers of capillaries which are perfused. Technically, CBF can be increased by increasing the velocity or the number of capillaries perfused, without an increase in CBV.

To deduce an analytical connection between CBF and CBV, we can combine equations 3.2 and 3.3:

$$\begin{aligned} & \overbrace{\text{CBF} \propto r^4}^{\text{Eq. 3.2}}, \overbrace{\text{CBV} \propto r^2}^{\text{Eq. 3.3}} \\ \Rightarrow \frac{\text{CBF}_{act}}{\text{CBF}_{rest}} &= \left(\frac{r_{act}}{r_{rest}}\right)^4 = \left(\left(\frac{r_{act}}{r_{rest}}\right)^2\right)^2 = \left(\frac{\text{CBV}_{act}}{\text{CBV}_{rest}}\right)^2 \\ &\Rightarrow \frac{\text{CBV}_{act}}{\text{CBV}_{rest}} = \left(\frac{\text{CBV}_{act}}{\text{CBV}_{rest}}\right)^{\frac{1}{2}} \end{aligned} \quad (3.4)$$

The classic paper of Grubb et al. [Grubb et al., 1974] is still the primary reference for the quantitative relationship between CBF and CBV changes. They found an empirical correlation between CBF- and CBV-changes for rhesus monkeys:

$$\text{CBV} = 0.8 \cdot \text{CBF}^{0.38} \quad (3.5)$$

This correlation is likely different in arteries, capillaries and venules [Lee et al., 2001] [Chen and Pike, 2010b]. The blood flow regulation mechanism of capillaries via pericytes controls CBF by increasing vascular resistance at few sites along the capillaries by throttling [Peppiatt and Attwell, 2004] [Harrison et al., 2002]. This regulation of CBF is consistent with the observation that CBF increases substantially, while CBV increases moderately.

Possible Explanation for the Substantial Increase in CBF The phenomenon that a brief neural stimulus produces a stronger increase of CBF than the increase in CMRO_2 lies at the heart of many functional neuroimaging techniques, and yet there is no consensus of the mechanisms involved. In [Buxton, 2010] Buxton describes a speculative mechanism that is consistent with experimental results. Here, the large increase of CBF is a result of the attempt to keep the partial pressure of oxygen in tissue at a constant level, despite an increase in CMRO_2 [Buxton, 2010].

OEF

OEF denotes the relative extraction of delivered O_2 . It is correlated with CMRO_2 and CBF in accord with equation 3.6.

$$\text{CMRO}_2 = \text{OEF} \cdot \text{CBF} \cdot \overbrace{[\text{O}_2]_a}^{\text{units of mole}} \quad (3.6)$$

In the human adult brain, the figure for OEF lies around 40%. While CBF increases with neural activity substantially and CMRO_2 increases only moderately, OEF decreases with neural activity.

Oxygenation

BOLD signal is the most prevalent MRI measure for functional studies. It is considered to be a combination of CMRO_2 , CBF and CBV with the deoxyhaemoglobin dilution model [Hoge et al., 1999].

3.3 Hyperoxia and Hypercapnia

Hypercapnia or hyperoxia can be evoked by breathing gas mixtures containing high fractions of CO_2 or O_2 respectively. Hypercapnia and hyperoxia have been used in calibration of fMRI for estimation of neural activation-induced changes in CMRO_2 [Mark et al., 2011]. CO_2 is a vasodilator (see section 3.1.2) and an increase in partial pressure of CO_2 in arterial blood has traditionally been used to increase CBF without affecting brain metabolism. In this work the focus lies on hyperoxia, since it is particularly useful in studies attempting to analyze BOLD-induced MRI-signal responses. Changes in deoxyhaemoglobin concentration during hyperoxia are often expected to occur independent of CBF, CBV and metabolism [Mark et al., 2011] [Bulte et al., 2007] [Chiarelli et al., 2007]. The underlying assumption of hyperoxia experiments is that fixed concentrations of inspired gas produce reliable iso-capnic (i.e., constant partial pressure of CO_2 in blood) changes in partial pressure of O_2 [Bulte et al., 2007]. This assumption is not always valid since the partial pressure of O_2 and CO_2 are both functions of ventilation. Furthermore, a multitude of mild physiological and biochemical effects have been shown. Hyperoxia can alter the acidity of blood, the binding of CO_2 and O_2 with haemoglobin as well as induce changes in ventilation and CBF [Bulte et al., 2007]. Many of these

physiological effects can be ignored for the purposes of using hyperoxia to estimate CBV [Bulte et al., 2007]; Others however, can not be ignored. For example, one characteristic physiological response to hyperoxia is a reduction in end-tidal partial pressure of CO_2 , which results in a mild hypocapnia. This decrease in the partial pressure of CO_2 is accompanied by vasoconstriction in the arterioles and a reduction of CBF and CBV respectively [Mark et al., 2011] [Bulte et al., 2007] [Chiarelli et al., 2007].

4 fMRI Methods: ASL and BOLD

Although it is laborious to localize neural activity without placing electrodes directly in the brain, the local response to neural activity can be visualized with functional magnetic resonance imaging. fMRI techniques utilize the change of magnetization due to changes of CBV, CBF and oxygenation level. In this thesis, changes in CBV are of special interest. Since changes in CBF and oxygenation can confound the fMRI measurements of CBV, they are discussed here.

4.1 MRI Techniques to Measure Perfusion

There are currently two established classes of MRI techniques that provide perfusion measurements in the resting brain; bolus tracking and arterial spin labeling (ASL).

Bolus tracking uses exogenous contrast agent, commonly gadolinium compounds, to alter local relaxation times. In arterial water, gadolinium reduces the T_1 of local magnetization. Thus, on T_1 weighted images gadolinium can increase the local MR signal. Apart from gadolinium, MION is often used to quantify CBV. It consists of Fe nanoparticles that are traceable by their susceptibility properties.

In ASL, arterial water is non-invasively tagged with magnetization inversion before it arrives to the tissue in the imaging slice. By comparing the images made after such tagging, with a control image of the same slice without the tagging, the perfusion can be assessed. There are two commonly used classes of ASL methods; continuous arterial spin labeling (CASL) and pulsed arterial spin labeling (PASL).

The first ASL technique proposed by Detre et al. [Detre et al., 1992] belongs to the CASL class. In CASL, blood magnetization within the large brain-feeding arteries is tagged with adiabatic inversion by means of an additional RF antenna. Labeling duration is several seconds. There are two major problems with CASL techniques: subtraction artifacts due to magnetization transfer effects, and decay of the magnetization of blood water as it travels from the place of labeling to the imaging slice.

In PASL, the labeling bolus is tagged outside the imaging slice with a short RF pulse $1 - 2sec$ before the image is acquired. A control image is acquired interleaved without such tagging. The signal difference between the two images is used to quantify the tagged blood that has flowed in the imaging slice during the $1 - 2sec$ perfusion period.

The two approaches, contrast agent tracking and ASL are quite different, as they measure different physiological variables. ASL provides only a measurement of CBF, while techniques based on exogenous contrast agents are also capable of measuring CBV.

4.2 BOLD

BOLD contrast is the MRI contrast caused by changes in blood deoxyhemoglobin. The functional effect of oxygenation of blood on the MR signal was first discovered in 1990 by Ogawa and colleagues [Ogawa et al., 1990]. BOLD fMRI has become the favored method for neuroscientific investigations of the working brain. The BOLD effect arises from two mechanisms, one biophysical and one physiological. (a) The paramagnetic deoxyhemoglobin produces magnetic field gradients around and through the blood vessels that decrease the MR signal due to induced magnetic field inhomogeneities and a corresponding dephasing of precessing magnetization. (b) Although the increase of local CMRO_2 is accompanied by an increase of deoxyhemoglobin, the local CBF increase is by far the dominant contribution. This leads to a deoxyhemoglobin washout much greater than in the resting state. Thus, brain activation is characterized by a fall in the local concentration of deoxyhemoglobin associated with an MR signal increase. The BOLD effect is not a direct measure of neural activity but rather depends on the blood flow and energy metabolism changes that arise from neural activity.

Since BOLD contrast is also a susceptibility effect, the contrast is increasing with higher magnetic field strengths. One of the most severe constraints on the spatial resolution of BOLD contrast fMRI is the draining vein problem. Activity-related changes in oxygenation are not confined to the site of activation. Changes in blood oxygenation arising from local brain activity-related changes in blood flow propagate downstream in veins and can give rise to spurious activation at sites remote to the neuronal activity [Turner, 2002]. The BOLD effect is most pronounced on GE-images, indicating that the effect is primarily an increase of the local value of T_2^* . At higher fields the intravascular blood signal is suppressed because T_2 of venous blood shortens with increasing field strength [Buxton, 2009]. Although the BOLD contrast is the favored fMRI technique, CBF and CBV approaches are finding wider appeal because these methods are less affected by confounding factors than BOLD.

4.2.1 Time Course of the BOLD Response

During neural activation BOLD signal follows a unique evolution in the shape of Fig. 4.1. The precise shape of this hemodynamic response function is dependent on the activated brain area and the stimulation paradigm [Chen and Pike, 2009] as well as the cortical depth and the vascular compartment (arteries, capillaries or veins) [Kim and Kim, 2010].

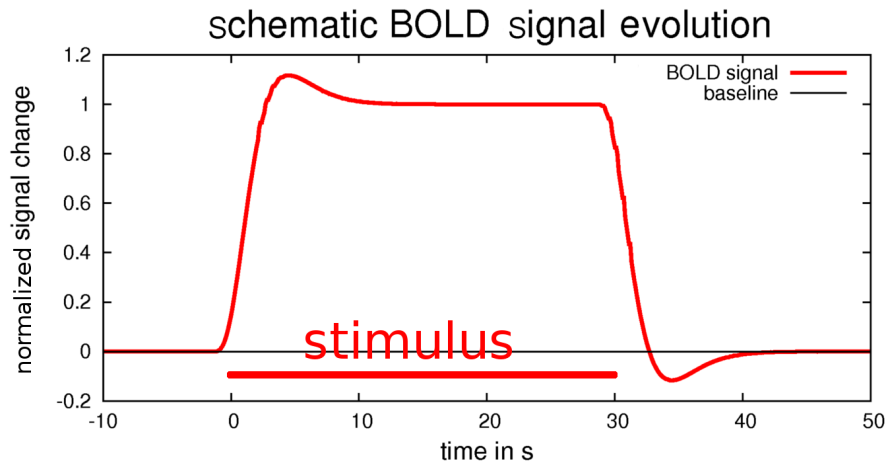


Figure 4.1: Schematic evolution of BOLD signal during neural activity. The response function is modeled for a stimulus of 30s. Note the relatively late peak ≈ 6 s after the stimulus inception and the post stimulus undershoot after the cessation of the stimulus.

During the first few seconds of after the beginning of the stimulus the BOLD signal does not increase substantially. Some studies even report a small initial dip [Buxton, 2010]. The maximum is typically reached after about 5-8 seconds [Chen and Pike, 2009]. After stimulus cessation, the main response is followed by a pronounced post stimulus undershoot. The post stimulus undershoot (and tentatively the initial dip as well) have been suggested to result from different evolution of CBF, CBV and $CMRO_2$ changes [Chen and Pike, 2010b]. The increases in CBV or $CMRO_2$ without increase in CBF result in BOLD signal decrease and vice versa. Hence the post stimulus undershoot can be explained by sustained elevated CBV or prolonged oxygen consumption. Some studies suggest that the origin of the post stimulus BOLD undershoot result from the fast recurrence to baseline in CBF, while CBV remains elevated after cessation of the stimulus (at least in the venous compartment) [Mandeville et al., 1999] [Buxton et al., 1998]. This mismatch of CBF and CBV would result in the accumulation of deoxyhaemoglobin in the vessels following associated with a BOLD undershoot. Other studies suggest that the undershoot is due to sustained elevation in oxygen consumption [Poser et al., 2011] [Schroeter et al., 2006] [Dechent et al., 2010].

There is currently no consensus on whether the post stimulus BOLD undershoot is a neural, vascular or metabolic effect.

5 VASO

5.1 CBV Based fMRI

CBV plays an important role in recent neuroscientific research. The knowledge of the exact behavior of CBV is essential to understand the widely used BOLD contrast [Buxton, 2010]. Detectable CBV changes may also be better localized to the site of neural activity [Turner, 2002]. A robust change in blood oxygen saturation can be seen in the venous drainage system $\approx 3mm$ distant from the area of activity, without any detectable change in blood volume [Kennerley et al., 2010].

Apart from VASO there are other MRI methods that quantify changes in CBV. Contrast agents such as gadolinium compounds or MION are often used to determine blood volume in animals. Apart from that, venous refocusing for volume estimation (VERVE) is a non-invasive MRI based method for measuring changes in deoxygenated blood volume [Stefanovic and Pike, 2005]. VERVE isolates the deoxygenated blood signal by exploiting the dependence of transverse relaxation rate in deoxygenated blood on refocusing intervals in spin echo sequence.

5.2 VASO

fMRI based on vascular space occupancy (VASO) detects CBV changes without the need for exogenous contrast agents [Lu et al., 2003]. This method is based on the idea that when CBV increases, it has to replace something else. Changes in CBV can be assessed through changes in the remaining extravascular water signal (see Fig. 5.1). The VASO contrast is accomplished by eliminating the blood signal in a way that is independent of blood oxygenation and blood flow.

The blood signal is nulled in the following way: At first a non-selective 180° inversion pulse inverts the longitudinal magnetization. After that the inverted magnetization returns exponentially to equilibrium with the longitudinal relaxation time constant T_1 . Since T_1 is different in blood and in tissue, the point at which the magnetization crosses through zero differs. At the time when $M_{blood}(TI) = 0$, the remaining tissue magnetization is excited with a 90° pulse. A sequence diagram and the corresponding steady-state z-magnetization of blood, GM and CSF is depicted in Fig. 5.2.

The technique is performed independent of blood flow by inverting magnetization in a spatially non-selective manner. Since T_1 depends on the magnetic field, blood T_1 must be determined to adjust TI for blood nulling at the corresponding field strength. As T_1 is independent of the oxygenation level, the VASO contrast is based on both arteriolar and venous CBV. The SNR for VASO is smaller than for BOLD, but slightly higher

than for PASL approaches at field strengths $< 7T$ [Lu et al., 2003]. It is important to point out that VASO-fMRI depends on a single physiological parameter (CBV), while BOLD-fMRI depends on multiple parameters. The VASO approach is believed to show good localization to grey matter, while BOLD can show many voxels outside of grey matter [Kim and Bandettini, 2010] [Donahue et al., 2006].

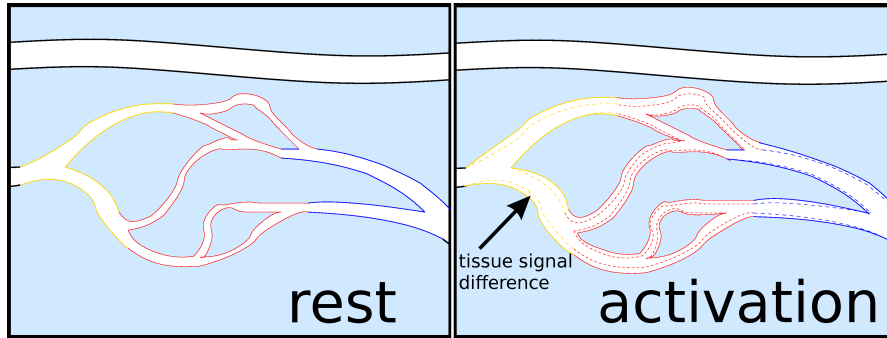


Figure 5.1: Vascular origin of VASO. Tissue is colored in blue. Blood is not colored to indicate that its signal is nulled during data acquisition. VASO signal is characterized by tissue signal decrease upon vasodilation. Signal change is believed to arise exclusively from the small vessels in a voxel.

One of the biggest drawbacks in VASO is the limited volume coverage. Since blood is only nulled for a single time point, only one excitation pulse can be played out during that point. Hence, VASO is not amenable to multi-slicing without further effort.

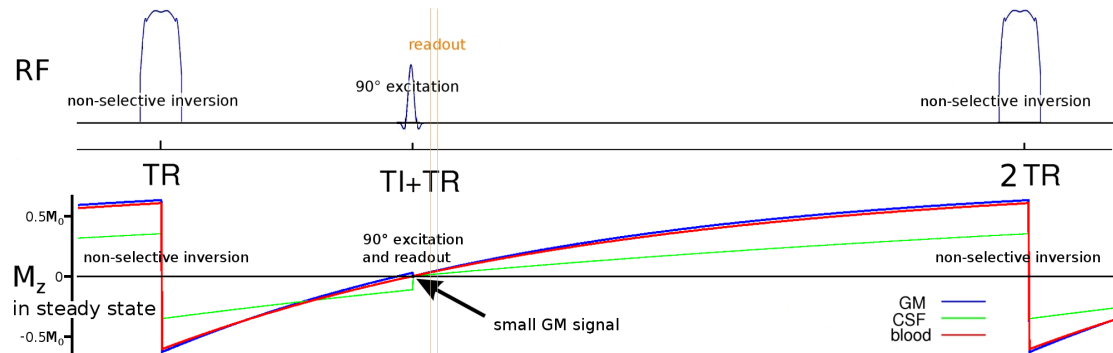


Figure 5.2: Sequence diagram of traditional VASO and the corresponding steady-state z-magnetization of GM, CSF and blood. The functional contrast is based on changes of the residual tissue signal at the blood nulling point (arrow).

In the past decade VASO was further investigated and adapted for several purposes in

many studies [Donahue et al., 2006] [Wu et al., 2007] [Hua et al., 2009] [Hua et al., 2011b] [Donahue et al., 2009b] [Jin and Kim, 2008] [Shen et al., 2009] [Scouten and Constable, 2007] [Poser and Norris, 2011] [Lu, 2008] [Lu and van Zijl, 2005] [Lu et al., 2004] [Donahue et al., 2010] [Donahue et al., 2009a] [Cohalan, 2009] [Lu et al., 2005] [Hua et al., 2011a] [Yang et al., 2004] [Scouten and Constable, 2008] [Hua et al., 2011c] [Tuunanen et al., 2006] [Poser and Norris, 2007].

5.2.1 Components of Cerebral Blood Volume

Components Within the Blood In order to compare VASO signal changes with other methods of measuring CBV, the components of CBV (i.g. plasma, heamoglobin or both) must be considered. Injected intravascular paramagnetic contrast agents that remain in circulation over several hours allow CBV measurements [Mandeville et al., 1998]. Since these MRI contrast agents are entirely plasma borne, the corresponding signal reflects changes in plasma volume CBV_p . Optical methods, on the other hand, can measure the volume of haemoglobin CBV_h [Hillman et al., 2007]. VASO signal change reflects the change of nulled blood. Because the reference blood T_1 corresponds to the total blood, VASO contrast is expected to measure changes in total blood volume CBV_t , consisting of plasma and cells. Early optical studies report that heamoglobin concentration might vary in a minority of the capillaries ($< 10\%$) [Villringer et al., 1994] [Pawlik et al., 1981]. Hence, the idea that blood plasma volume and red cell volume might not completely correlate during functional brain activation must be considered. For this reason, CBV_h measurements were recently compared with CBV_p measurements [Herman et al., 2009]. CBV_p measurements with MRI using a paramagnetic iron oxide contrast agent were taken in rats and compared with CBV_h measurements taken with laser-Doppler flowmetry. Even in sub-millimeter resolution (voxel size $0.04mm \times 0.04mm \times 2mm$), excellent correlations between CBV_p - and CBV_h -dynamics were found, independent of cortical depth. It is suggested that CBV measurements from either method could be used to reflect dynamic changes in CBV_t and vice versa [Herman et al., 2009]. Spatial resolution that is much higher than available with MRI may be needed for differentiating between the different branches in micro vasculature. Recently Uh et al. [Uh et al., 2011] compared VASO MRI with a radio tracer based positron emission tomography technique. The results show a high correlation between CBV changes measured with VASO MRI and CBV changes measured with PET, both in location and absolute values of CBV change. Moreover, Lin et al. [Lin et al., 2011] showed strong compliance of CBV changes measured with VASO and with contrast agent-based method (Gd DTPA) for different visual stimuli.

Size of Vessels that can Dynamically Change their Diameter Vessels larger than $100\mu m - 200\mu m$ are believed to be negligible for local regulation of blood flow during activation [Kuschinsky, 2000]. Only smaller intra-parenchymal vessels are influenced by neurovascular coupling. Harrison et al. showed with electron microscopy studies that only very small vessels are capable of expanding or contracting [Lee et al., 2001]. Only

arterioles with diameters below $\approx 80\mu m$, capillaries and some of the smallest venules (diameter $< 100\mu m$) comprise the vessels that change their volume and flow during activity.

5.2.2 VASO at High Fields

There are two major challenges for VASO at high fields. First, blood T_1 and grey matter T_1 converge at high fields despite increase in both. This results in a very small tissue signal at the blood nulling point. Second, increasing BOLD effect at high fields can counteract the VASO signal change. Gradient echo BOLD is known to have both intravascular and extravascular contributions. Since the blood signal is nulled in VASO experiments, only the extravascular BOLD effect can contribute to the VASO contrast. The extravascular part of the BOLD signal is believed to increase with high fields [Kim and Bandettini, 2010], compared to the intravascular counterpart. This extravascular BOLD effect tends to diminish the VASO signal, especially at large TE. When the extravascular BOLD changes outweigh CBV effects at very long TE, the VASO signal change may even become positive [Lu and van Zijl, 2005].

5.2.3 ASL and Steady-State Effect

Although blood magnetization was assumed to be in steady-state in the initial VASO-paper [Lu et al., 2003], this may not be completely true. If TR is too long, or the inversion volume thickness is too small (e.g. due to small extent of the transmission coil), some of the blood that enters the imaging slice will be fresh and rather than in steady-state. Due to the substantial CBF increase during activation, more of that fresh blood, which is not in steady-state, enters the imaging slice. Considering that fresh blood has been inverted only once or twice, this ASL effect would cause an overestimation of the VASO contrast [Donahue et al., 2006] [Donahue et al., 2009b]. As the difference of the steady-state signal of blood water and tissue water is larger at short TR, the fresh-blood effect appears primarily at short TR.

5.2.4 Dependencies of blood T_1 on VASO

VASO measures the relative change of nulled blood. The VASO method is based on the assumption that the total blood is nulled due to its unique T_1 [Lu et al., 2003]. Literature values for T_{1blood} at 7 Tesla are given in Table 5.1. In this study the value of $T_{1blood} = 2100ms$ is assumed.

Reference	[Rooney et al., 2007]	[Dobre et al., 2006]	[Francis et al., 2008]
$T_{1\text{ blood at 7 T}}$	2587(± 283)	2212(± 53)	1950

Table 5.1: Literature values of blood T_1 at 7 Tesla in ms . $2100ms$ seems to be an acceptable representative value.

Total blood volume is referred to as the sum of both blood plasma volume and the blood hemoglobin volume in arteries, arterioles, capillaries, venules and veins independent of their hematocrit. In the following the dependencies of blood T_1 is considered to ensure that all blood compartments are nulled simultaneously.

Hematocrit The hematocrit measures the volume of red blood cells compared to the total blood volume. The normal hematocrit for men is 40% to 54%; for women it is 36% to 48% [Billett, 1990]. Hematocrit does not only change between subjects but also within subjects. Thin capillaries with small diameters could be too narrow during rest for red blood cells to flow through. During vasodilation these capillaries can become large enough for hematocrit to increase. Kuschinsky et al. [Kuschinsky, 1996], Pawlik et al. [Pawlik et al., 1981] and Villringer et al. [Villringer et al., 1994] report on a negligible fraction of capillaries ($< 10\%$), that show such behavior. Data in [Herman et al., 2009] indicate that hematocrit level is not affected during functional activation. Hillman et al. [Hillman et al., 2007] report a tendency of hematocrit to increase ($6.4\% \pm 8.6\%$) in the venous compartment. Higher hematocrit is believed to decrease the blood T_1 [Lu et al., 2004], [Dobre et al., 2006]. This means that the blood nulling time may differ in men and women. Lu et al. [Lu et al., 2004] report a hematocrit dependent T_{1blood} change of $\approx 150ms$ at 3T for the range of hematocrit values 36% - 50%. The only study determining the dependence of the hematocrit level on blood T_1 at 7 Tesla is [Dobre et al., 2006]. In this study Dobre et al. report that a significant longer blood T_1 was observed only for blood with a lower hematocrit content than 30%.

In conclusion, although hematocrit varies between subjects, the corresponding change in blood T_1 is negligible at 7 Tesla.

Oxygenation Blood T_1 is known to be less sensitive to oxygenation than T_2^* or T_2 . However, it is controversial whether there is a significant difference between arterial and venous blood T_1 .

Lu et al. reports that blood T_1 at 1.5 Tesla is $1355 \pm 38ms$ for fully oxygenated and $1390 \pm 44ms$ for 47% oxygenated blood [Lu et al., 2003], which is not a significant difference. Independence of blood oxygenation to T_1 has been reported from Brooks et al. at this field strength [Brooks and Chiro, 1987]. At 3 Tesla Lu et al. reports that blood T_1 is $1664 \pm 14ms$ (arterial) and $1584 \pm 5ms$ (venous) at a typical human hematocrit of 0.42 [Lu et al., 2004]. It must be pointed out that Lu et al. state that at 1.5T oxygenated blood has shorter T_1 than deoxygenated blood [Lu et al., 2003]. Furthermore, they claim that this relationship is turned around at 3T [Lu et al., 2004]. Dobre et al. reports in a study determining blood T_1 at 4.7, 7.0 and 9.4 Tesla that there is no significant difference of T_1 larger than $50ms$ [Dobre et al., 2006].

A potential decrease of blood T_1 of approx. $50ms$ in the venous compartment could lead to a positive blood signal with a magnetization of $\approx 2.3\%$ (estimates with T_1 of $2100ms$ and equation $M(TI) = M_0 - e^{-\frac{TI}{T_1}} (M_0 - M(t = T))$). This would lead to an VASO underestimation of $\approx 10\%$ (assuming a common CBV change of $\frac{\Delta CBV}{CBV_{rest}} = 25\%$

according to Tab. 5.3) in the venous compartment.

In conclusion, blood might vary in the order of $\approx 50ms$ dependent on its oxygenation. But, this variation is negligible compared to the uncertainty of the literature values of blood T_1 (see Tab. 5.1).

Acquisition Window The number of slices is limited by the allowed acquisition time. Most VASO studies acquire only a single slice. Scouten et al. acquires three slices per inversion in her Whole-Brain MAGIC method at 3 Tesla [Scouten and Constable, 2007]. At 7 Tesla however, blood T_1 is $\approx 25\%$ larger [Rooney et al., 2007] [Dobre et al., 2006], hence the acquisition time window when blood is approximately nulled increases for 7 Tesla.

Estimation of the Maximum Number of Acquired Slices: The relative blood signal can be written as

$$\begin{aligned} M(TI + \Delta T_a) &= M_0 - e^{-\frac{TI + \Delta T_a}{T_{1blood}}} (M_0 - M(t=0)) = xM_0 \\ M(TI - \Delta T_b) &= M_0 - e^{-\frac{TI - \Delta T_b}{T_{1blood}}} (M_0 - M(t=0)) = -xM_0 \end{aligned} \quad (5.1)$$

the total acquisition window ΔT is given as $\Delta T = \Delta T_a + \Delta T_b$

x denotes the tolerable error in blood signal (\propto magnetization). Equation 5.1 can be rearranged to

$$\Delta T = T_{1blood} [\ln(1+x) - \ln(1-x)] \underbrace{\approx}_{\text{Taylor expansion}} T_{1blood} 2x + \mathcal{O}(x^3) \quad (5.2)$$

Let's consider a blood signal of 5% ($x=0.05$). In this case the error in ΔCBV would be 1.25% (assuming a common CBV change of $\frac{\Delta CBV}{CBV_{rest}} = 25\%$ according to Tab. 5.3). For this x -value the acquisition window ΔT of equation 5.2 is 210ms. During this acquisition window, four slices with an echo spacing of 59ms can be acquired. Echo spacing denotes the time it takes to acquire one slice with the acquisition parameters used in this study (see more in chapter 7).

5.2.5 Quantification of CBV Change from VASO Signal Changes

The VASO data can be calibrated to determine the changes in total cerebral blood volume from the relative VASO signal change.

Partial Volume Effect In the calibration of the VASO data, no changes in volume fraction of CSF between activation and baseline are assumed. Knowledge of the composition of each activated voxel is essential in accurate $\frac{\Delta CBV}{CBV_{rest}}$ determination. In other words, in an activated voxel that is only partly filled with GM, the CBV change can be calculated, if the relative GM signal contribution of that voxel is known. The GM signal contribution of a voxel depends on the GM volume in the voxel, GM z-magnetization and water

proton density of GM. The relative signal contribution of GM, WM, and CSF in a voxel can be assessed by means of separately acquired images with differing T_1 based contrasts (see section 5.5).

Cerebral Blood Volume at Rest The calculation of $\frac{\Delta CBV}{CBV_{rest}}$ from $\frac{\Delta VASO}{VASO_{rest}}$ within a two-compartment-model is highly sensitive to CBV_{rest} [Scouten and Constable, 2007]. The values of the literature are in the range between $3.8 \frac{ml}{100ml}$ and $7.1 \frac{ml}{100ml}$ (see Tab. 5.2). In this range it is possible that the true value of CBV_{rest} is underestimated by 30%. Computer simulations show that a corresponding error of $\approx 50\%$ in $\frac{\Delta CBV}{CBV_{rest}}$ for this underestimation [Scouten and Constable, 2007] [Wu et al., 2007]. Interestingly, simulations in these studies suggest that if CBV_{rest} must be estimated, it is better to overestimate this value, as the simulated error in $\frac{\Delta CBV}{CBV_{rest}}$ is more forgiving in that direction. However, it is clear that any error in the estimation of CBV_{rest} will have a significant impact on the calculation of $\frac{\Delta CBV}{CBV_{rest}}$ from VASO measurements.

Reference	CBV_{rest}	Comment
[Bulte et al., 2007]	3.93 (± 0.9)	using hyperoxic MRI contrast
[Gu et al., 2006]	4.5 (± 1.5)	multiexponential T_1 -fit
[Giovacchini et al., 2002]	5.5 (± 0.6)	^{11}CO PET Average in GM
[Giovacchini et al., 2002]	7.1 (± 1.2)	^{11}CO PET in the occipital association
[Ito et al., 2004]	3.8 (± 0.7)	^{15}O PET in the whole cerebral cortical region
[Donahue et al., 2006]	5.5	comparison of four studies
[Lu et al., 2005]	5.5 (± 0.2)	VASO in combination with Gd-contrast agent in whole cortical grey matter
[Engvall et al., 2008]	4.2 (± 0.3)	^{99m}Tc -RBC SPECT in whole brain
[Engvall et al., 2008]	6.2 (± 0.8)	^{99m}Tc -RBC SPECT in occipital lobe

Table 5.2: Literature values of the cerebral blood volume at rest in $ml/100mlGM$

It is important to note, that these numbers refer to the whole blood volume in the grey matter, i.e. arteries, arterioles, capillaries, venules and veins. Dependent on the definition of the different vessel compartments, only arterioles, capillaries and venules change their volume and flow. Any numbers in CBV change $\frac{\Delta CBV}{CBV_{rest}}$ must be related to a number in CBV fraction at rest. Weber et al. showed with optical methods in macaques that the microvessels smaller than $\approx 12\mu m$ contribute only $\approx 2.22\% \pm 0.32\%$ to the grey matter volume in V1 in the visual cortex [Weber et al., 2008].

The literature values of $\frac{\Delta CBV}{CBV_{rest}}$ are collected in Tab. 5.3

Reference	ΔCBV	reference CBV_{rest}	Comment
[Donahue et al., 2009a]	17%($\pm 7\%$)	5.5 %	VASO-Flair with flashing checkerboard ($f = 8Hz$)
[Vafaee and Gjedde, 2004]	21%($\pm 5\%$)	-	^{11}CO PET with flashing checkerboard ($f = 8Hz$)
[Cohalan, 2009]	24%($\pm 12\%$)	5.5%	VASO with flashing checkerboard ($f = 8Hz$)
[Lu et al., 2003]	46%	4.6%	VASO with flashing checkerboard ($f = 8Hz$)
[Gu et al., 2006]	33%($\pm 12\%$)	4.5 %	TI-fit with flashing checkerboard (b-w , $f = 8Hz$)
[Ito et al., 2001]	21%($\pm 5\%$)	3%	with flashing checkerboard ($f = 8Hz$)
[Belliveau et al., 1991]	32%($\pm 10\%$)	-	Gd-contrasts with flashing checkerboard ($f = 7.8Hz$)
[Frank et al., 1994]	23.5%($\pm 14\%$)	-	Gd-contrast with flashing checkerboard ($f = 8.8Hz$)
[Pears et al., 2003]	28%($\pm 7\%$)	4%	Gd-contrast with flashing checkerboard ($f = 8Hz$)
[Piechnik et al., 2009]	30%($\pm 7\%$)	4%	multiexponential T2 Fit with flashing checkerboard ($f = 10Hz$)
[Wu et al., 2007]	40%($\pm 5\%$)	6%	variant form of VASO with flashing checkerboard (b-w , $f = 8Hz$)
[Hua et al., 2011b]	58%($\pm 7\%$)	1.1 %	change in CBV, that enters the imaging slice during 2s with flashing checkerboard (b-w , $f = 8Hz$)

Table 5.3: Literature values of the relative change in cerebral blood volume in %.

5.3 BOLD-Corrected VASO

Extravascular BOLD signal increase during activation counteracts the VASO contrast and results in an underestimation of VASO signal change. At magnetic field strengths up to $3T$, this contamination can be circumvented with $TE < 10ms$. It is technically not easy to use a shorter TE to circumvent BOLD contamination at $7T$ without further ado.

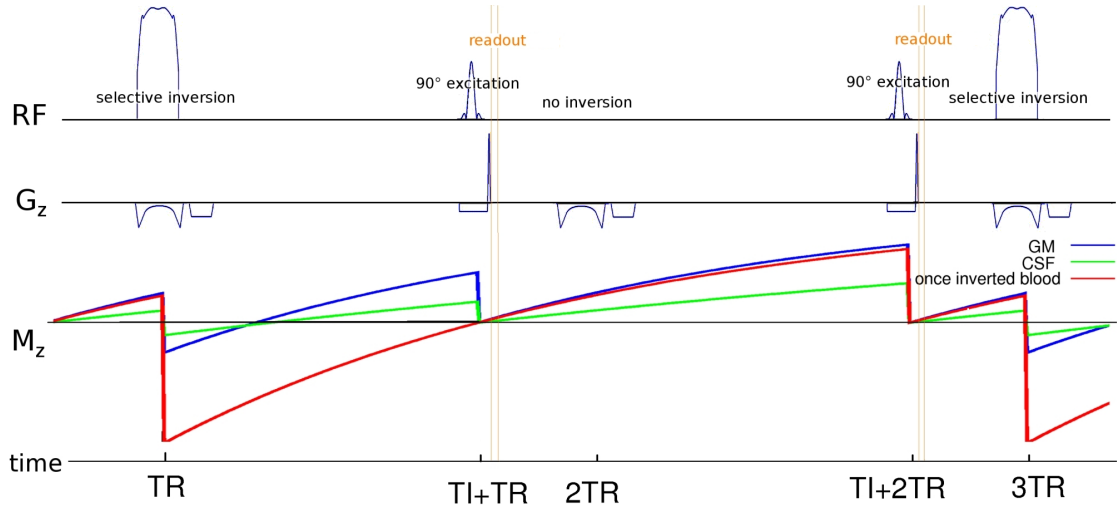


Figure 5.3: VASO Sequence diagram that can account for BOLD contamination with the corresponding steady-state z-magnetization of GM, CSF and blood. The fact that the inversion pulse is played out with a slab-selective gradient is discussed in section 5.4.2.

Here, a BOLD correction scheme is presented that is based on a sequence that acquires VASO and BOLD contrast interleaved. Fig. 5.3 depicts a VASO sequence diagram where the inversion pulse is played out only every second TR. In this way, two different contrasts are acquired interleaved. The first image is acquired when blood is nulled (bn). This represents the VASO image with a small BOLD contamination. The second image is acquired while blood is not-nulled (bnn), representing pure BOLD contrast. By assessing the BOLD effect in the second image, the BOLD contamination of the first image can be cancelled out.

Underlying Model

Here, a model is developed that can correct the BOLD effect in the VASO signal without the necessity to determine the activation state. This means that the T_2^* -dependence is cancelled out in all voxels independent of their activation state. In this method, it is assumed that the change of the ratio of the signal intensity with and without previous inversion is proportional to the change in CBV. This assumption is only valid, if both of the following are true: (a) T_2^* is the same in consecutive acquisitions. This implies that T_2^* is equal in both the blood-nulled image and in the blood-not-nulled image. (b) The z-magnetization at the time of the acquisition of the blood-not-nulled image is independent of neural activity. In other words, activation-dependent signal change in the image without previous inversion is only dependent on oxygenation-induced T_2^* changes. To explore the validity of these assumptions, theoretical signal contributors are considered below.

Let's consider the distribution of the signal arising from parenchyma. Parenchyma consists of grey matter and small vessels. The signal can be expressed

$$\begin{aligned}
S &\propto V_b \rho_b \frac{M_z b(TI)}{M_0} e^{-\frac{TE}{T_2^* b}} + V_{gm} \rho_{gm} \frac{M_z gm(TI)}{M_0} e^{-\frac{TE}{T_2^* gm}} = \\
&= \left[V_b \rho_b \frac{M_z b(TI)}{M_0} C + V_{gm} \rho_{gm} \frac{M_z gm(TI)}{M_0} \right] e^{-\frac{TE}{T_2^* gm}} \quad (5.3) \\
&\quad \text{with } C = e^{TE \left(\frac{1}{T_2^* gm} - \frac{1}{T_2^* b} \right)}
\end{aligned}$$

The terms of equation 5.3 are listed in table 5.4.

Symbol	Name	Value	Reference
V_b	cerebral blood volume	$0.055 \frac{ml}{ml}$	representative value from table 5.2
V_{gm}	volume of grey matter	$1 - 0.055 = 0.945 \frac{ml}{ml}$	-
ρ_b	water proton density of blood	$0.87 \frac{ml}{ml}$	[Donahue et al., 2009b]
ρ_{gm}	water proton density of grey matter	$0.891 \frac{ml}{ml}$	[Donahue et al., 2009b]
ρ_{par}	water proton density of parenchyma	$0.89 \frac{ml}{ml}$	[Donahue et al., 2009b]
$T_{1 b}$	blood T_1 at 7T	$2100ms$	representative value from table 5.1
$T_{1 gm}$	grey matter T_1 at 7T	$1900ms$	representative value from table 6.1
TI	inversion time, blood nulling time	$1455ms$	$T_{1 b} \ln(2)$
$T_2^* b$	T_2^* in vessel region at rest at 7T	$12.8ms$	[Yacoub et al., 2001]
$T_2^* gm$	T_2^* in grey matter at rest at 7T	$25.1ms$	[Yacoub et al., 2001]
ΔR_b	change of inverse T_2^* in vessel region due to BOLD at 7T	$1.43ms^{-1}$	[Yacoub et al., 2001]
ΔR_{gm}	change of inverse T_2^* in grey matter due to BOLD at 7T	$1.46ms^{-1}$	[Yacoub et al., 2001]

Table 5.4: assumed values in the BOLD-corrected model

We consider the longitudinal magnetization of blood and grey matter with and without previous inversion. According to the Bloch equation (2.11) the longitudinal magnetiza-

tion is given by:

$$\frac{M_z(TI)}{M_0} = 1 - e^{-\frac{TI}{T_1}} \left(1 - \frac{M_z(0)}{M_0} \right) \quad (5.4)$$

In the steady-state of an inversion recovery sequence, grey matter magnetization with foregone inversion (bn) is given by

$$\frac{M_z^{bn}(TI)}{M_0} = 1 - 2e^{-\frac{TI}{T_1}} + e^{-\frac{TR}{T_1}} \quad (5.5)$$

Blood magnetization at TI after inversion is 0 by design. Without previous inversion (bnn), grey matter or blood magnetization are given by

$$\frac{M_z^{bnn}(TI)}{M_0} = 1 - e^{-\frac{TR}{T_1}} \quad i \in \{b, gm\} \quad (5.6)$$

To get a BOLD-corrected VASO contrast the blood-nulled signal is normalized with the blood-not-nulled signal.

$$\frac{Signal^{bn}}{Signal^{bnn}} \stackrel{\text{Eq. 5.3}}{=} \frac{V_{gm} \rho_{gm} M_z^{bn}(TI) e^{-\frac{TE}{T_2^{*gm}}}}{\left[V_b \rho_b M_z^{bnn}(TI) C + V_{gm} \rho_{gm} M_z^{bnn}(TI) \right] e^{-\frac{TE}{T_2^{*gm}}}} \quad (5.7)$$

Now $e^{-\frac{TE}{T_2^{*gm}}}$ cancels out. To obtain an expression only dependent on V_b , $V_{gm} \rho_{gm}$ is rewritten as

$$V_{gm} \rho_{gm} = V_{par} \rho_{par} - V_b \rho_b \quad (5.8)$$

so that equation 5.7 becomes:

$$\frac{Signal^{bn}}{Signal^{bnn}} = \frac{(V_{par} \rho_{par} - V_b \rho_b) M_z^{bn}(TI)}{V_b \rho_b M_z^{bnn}(TI) C + (V_{par} \rho_{par} - V_b \rho_b) M_z^{bnn}(TI)} \quad (5.9)$$

The blood volume change is assumed to arise only from water exchange between grey matter tissue and blood water. Hence, V_{par} is assumed to be independent of functional activation. The parenchyma fraction in the voxel V_{par} can be determined with a high-resolution grey matter mask or with the methods discussed in section 5.5. Equation 5.9 can be rearranged to:

$$\frac{Signal^{bn}}{Signal^{bnn}} = \frac{\rho_{par} - \frac{V_b}{V_{par}} \rho_b}{\rho_{par} \frac{M_z^{bnn}(TI)}{M_z^{bn}(TI)} + \frac{V_b}{V_{par}} \rho_b \left(C \frac{M_z^{bnn}(TI)}{M_z^{bn}(TI)} - \frac{M_z^{bnn}(TI)}{M_z^{bn}(TI)} \right)} \quad (5.10)$$

Therewith, the theoretical VASO-contrast is:

$$\Delta \frac{S^{bn}}{S^{bnn}} = \frac{S^{bn \text{ act}}}{S^{bnn \text{ act}}} - \frac{S^{bn \text{ rest}}}{S^{bnn \text{ rest}}} = \quad (5.11)$$

$$\frac{\rho_{par} - \frac{V_b^{act}}{V_{par}} \rho_b}{\rho_{par} \frac{M_z^{bnn}(TI)}{M_z^{bn}_{gm}(TI)} + \frac{V_b^{act}}{V_{par}} \rho_b \left(C^{act} \frac{M_z^{bnn}(TI)}{M_z^{bn}_{gm}(TI)} - \frac{M_z^{bnn}(TI)}{M_z^{bn}_{gm}(TI)} \right)} - \frac{\rho_{par} - \frac{V_b^{rest}}{V_{par}} \rho_b}{\rho_{par} \frac{M_z^{bnn}(TI)}{M_z^{bn}_{gm}(TI)} + \frac{V_b^{rest}}{V_{par}} \rho_b \left(C^{rest} \frac{M_z^{bnn}(TI)}{M_z^{bn}_{gm}(TI)} - \frac{M_z^{bnn}(TI)}{M_z^{bn}_{gm}(TI)} \right)}$$

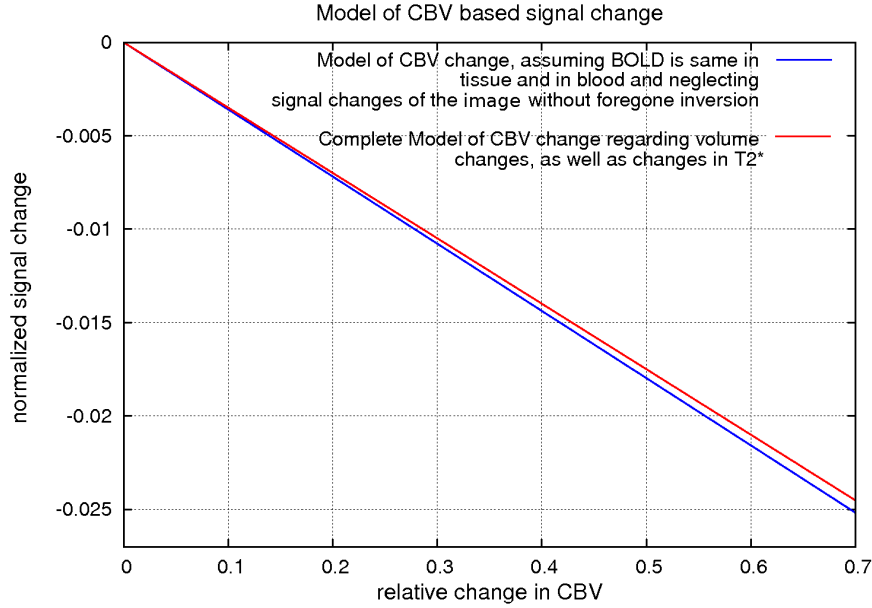


Figure 5.4: Model based connection between BOLD-corrected VASO signal change and change in CBV.

Figure 5.4 shows that under the aforementioned assumptions CBV is underestimated by $\approx 2.5\%$. In the range of physiologically possible CBV changes (0 to 40%) the BOLD-corrected signal change is in a linear range. De facto, one can get a BOLD-corrected VASO signal if one divides the signal intensity with nulled blood by the signal without nulled blood. This signal ratio is proportional to changes in CBV (blue curve in Fig. 5.11). Minimal higher order corrections can be done after the determination of the signal change. These higher order corrections contain estimated values of T_2^* that are needed in the C -terms of Eq. 5.11.

5.4 Slab-Selective VASO

5.4.1 Steady-State Considerations in Traditional VASO at High Fields

One of the biggest challenges in VASO is the small SNR. Even for long TR, the GM z-magnetization is very low at the blood nulling point due to similar GM T_1 and blood T_1 . This problem gets worse with high magnetic fields. Here T_1 values of blood and tissue converge, despite the increase in T_1 . For example, the relative difference in T_1 at 3T is $\approx 26\%$ [Donahue et al., 2006] and at 7T the relative difference in T_1 is only $\approx 18\%$ [Rooney et al., 2007]. Since short TR results in saturation of z-magnetization, SNR becomes even smaller for higher temporal resolution. The steady-state z-magnetization of GM, CSF and blood at the blood nulling point are depicted in Fig. 5.5 (b) for a reasonable range of TR (solid lines).

Several methods are described in the literature that can increase GM z-magnetization in VASO. Wu et al. developed a VASO variant with not-nulled blood [Wu et al., 2007]. In that method, CNR increases up to 160% caused by longer inversion times. On the down side, CBV has to be reconstructed in a non-linear way by means of literature values of relaxation times and proton densities. Donahue et al. [Donahue et al., 2010] and Hua et al. [Hua et al., 2011b] [Hua et al., 2011c] developed an inflow based VASO (iVASO) variant that is similar to PASL. In this variant, blood outside of the imaging slice is labeled and the image is acquired when this labeled blood is nulled. Therewith, only the blood volume that enters the imaging slice during TI can be determined. In that method, an SNR increase of $\approx 334\%$ is reported [Hua et al., 2011b]. Jin and Kim [Jin and Kim, 2008] developed a slab inversion VASO variant in cats at 9.4T. In this study TI is optimized to increase SNR and is chosen to be smaller than blood transit time. Therefore blood is not completely nulled. A huge SNR increase is reported with this method. However, the signal change does not reflect changes in CBV, but a mixture of CBF and CBV. Shen et al. [Shen et al., 2009] developed a VASO variant that is based on nulling extravascular GM signal and report about an fMRI signal increase of $\approx 250\%$. It has been shown that VASO signal maybe influenced by factors other than CBV changes, depending on the imaging parameters that are used [Donahue et al., 2006] [Donahue et al., 2009b] [Scouten and Constable, 2008] [Lu and van Zijl, 2005]. Donahue et al. showed that in the case when $TR < 5s$ and when no body coil is available for RF transmission, flow related effects contribute significantly to the VASO signal change. Flow effects result from blood spins whose magnetization have not reached steady-state [Donahue et al., 2006]. This problem is even worse at high fields due to long TI. To alleviate the signal contamination in VASO caused by fresh blood inflow, a non-selective saturation (90 RF pulse followed by spoiler gradients) can be applied after each readout [Lu, 2008]. On the other hand, this forced steady-state can be hampered at high fields due to large B_1 -inhomogeneities.

5.4.2 Slab-Selective VASO

Here a VASO variant is described that can increase SNR substantially by intentionally keeping stationary tissue in a steady-state other than flowing blood. It is exploited that

the blood transit time from the arteries in the neck to the microvessels of the imaging slice is comparable to the blood nulling time at 7T. The only simple change compared to traditional VASO is that the inversion pulse is accompanied with a slab-selective gradient. The inversion slab thickness and TR are adjusted in a way that all blood in the microvessels of the imaging slice has been inverted only once. To be in control of blood z-magnetization despite variable blood transit times, special attention has to be given on the choice of inversion slab thickness. It has to be thick enough that no fresh (not inverted) blood coming from outside of the inversion slab is flowing into the microvessels of the imaging slice during TI . On the other hand, it should not be so thick that the blood entering the imaging slice has been inverted twice. Furthermore, TR has to be longer than the time that blood stays within the imaging slice. Otherwise, blood spins that experienced the excitation pulse of the previous readout would be in a different steady-state than blood that didn't experience that pulse and so it would not be nulled at the acquisition time. Since only vessels with a diameter below $100\mu m$ are involved in local regulation of blood volume [Lee et al., 2001], it is sufficient to regard only the microvessels of the imaging slice.

The big advantage in this approach is that the blood nulling time (TI) of once-inverted blood is very long. This gives the tissue z-magnetization more time to relax to higher values before the image is acquired. The result is a higher MR signal. Fig. 5.5 (a) and (b) depict the z-magnetization of GM, blood and CSF in the slab-selective approach.

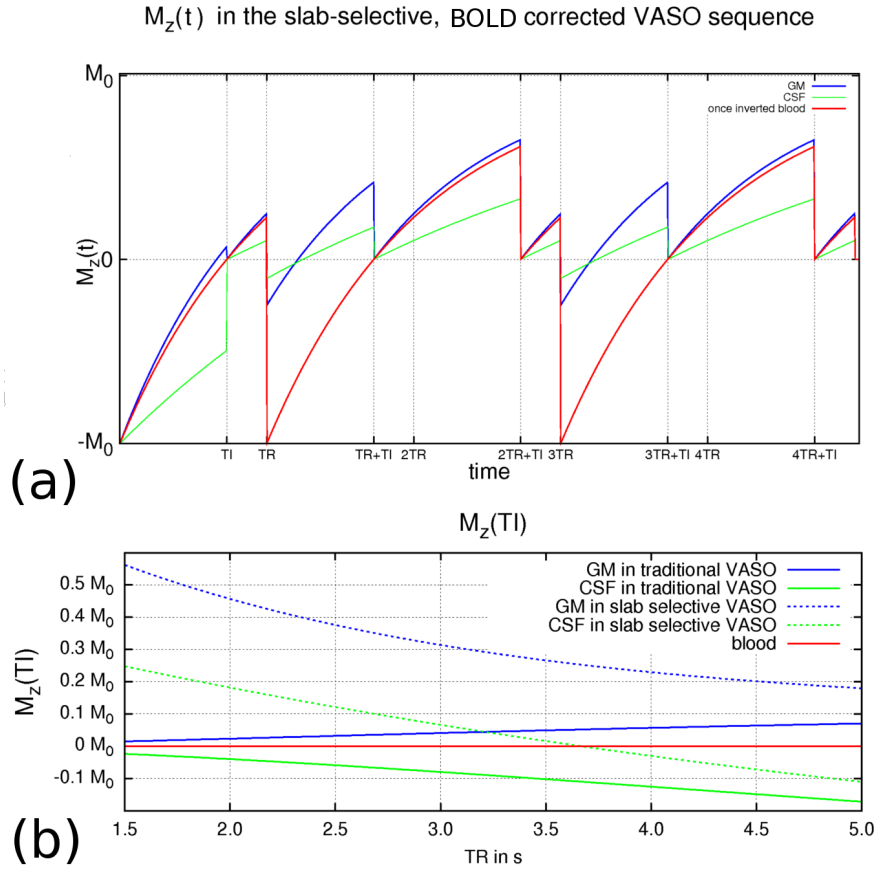


Figure 5.5: (a) The z-magnetization of GM, blood and CSF during the slab-selective sequence. Note that only once-inverted blood is considered. The compartment of the depicted blood z-magnetization is replaced at each time of inversion ($2TR$). Consequently, the absolute value of blood z-magnetization is not the same before and after inversion. (b) depicts the steady-state z-magnetization of GM, blood and CSF at the blood nulling point of steady-state blood in traditional VASO (solid lines) and at the blood nulling point of once-inverted blood in slab-selective VASO (dashed lines). GM z-magnetization is generally larger in slab-selective VASO. For short TR , the relative GM magnetization increase is up to 1000% compared to traditional VASO. T_1 values used in the calculations are 1.9s, 2.1s and 4s for GM, blood and CSF (representative values from Tab. 6.1)

The comparison of z-magnetization in traditional VASO with slab-selective VASO in Fig. 5.5 shows an immense GM signal increase in z-magnetization for slab-selective VASO. The available z-magnetization is directly proportional to the signal. A signal increase of $\approx 1000\%$ is confirmed in pilot studies for $TR = 1.5s$ (see Fig.5.6).

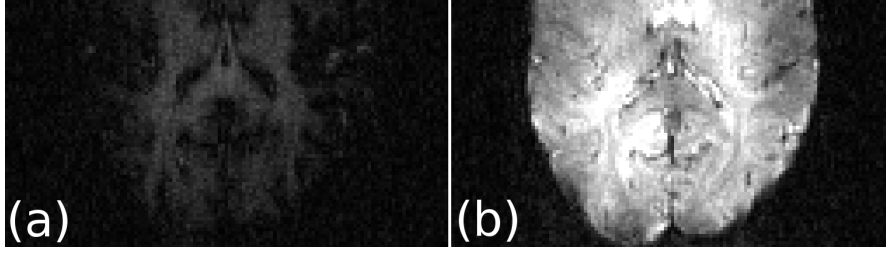


Figure 5.6: (a) EPI image acquired with traditional VASO with nulled steady-state blood. (b) EPI image acquired with slab-selective VASO with nulled blood that has been inverted only once. These unaccelerated EPI images are obtained at 7T in pilot measurements, with 1.5 mm isotropic spatial resolution, echo time $TE = 19ms$. Both images are acquired with the same scale factor and the same repetition time of $TR = 1.5s$. The blood nulling time for steady-state blood is $TI = 604ms$ (a). The blood nulling time for once-inverted blood is $TI = 1328ms$ (b). It can be seen that the GM signal is much higher in the slab-selective VASO.

5.4.3 Transit Times of Blood

To ensure that all blood in the small vessels of the imaging slice is nulled, it is crucial to know the physiologically time that blood needs to perfuse a certain slice within the brain. The transit time is often divided into two parts. δt is the time needed for blood to reach the region of interest and δ_a is the time for blood to traverse the arterial compartment in region of interest before reaching capillaries. Since in this study visual stimulation is used, the transit times to the occipital lobe are of special interest. The transit time to the occipital lobe is $\approx 900ms - 1300ms$ (see Tab. 5.5).

Reference	δt	Comment
[Wong et al., 1997]	1000ms – 1300ms	Gap between tag and imaging slice is 1cm
[Figueiredo et al., 2005]	960ms \pm 170ms	Gap between tag and imaging slice is 1 – 3cm
[MacIntosh et al., 2010]	935ms \pm 108ms	Gap between tag and imaging slice is 4cm.
[Chen et al., 2011]	1100ms – 1400ms	In occipital lobe. Gap between tag and imaging slice is 4.5cm.

Table 5.5: Literature values of the time blood needs to arrive at the region of interest. After this time δt the blood begins to fill the imaging slice.

The time δ_a to reach the capillary compartment in the region of interest takes approximately an additional 400ms – 500ms [Hall et al., 2011], [Francis et al., 2008]. These

numbers suggest that the inversion time TI in VASO should not exceed $\delta t + \delta_a \approx 1000ms + 500ms = 1500ms$. Mildner claims that it takes $> 2s$ for blood to flow from the circle of Willis to the small vessels, which change volume in response to activity [Mildner et al., 2010]. In a recent study, Chen et al. [Chen et al., 2011] measured blood arrival times to the microvessels of the occipital lobe of $\approx 1.6s$ for a gap of $4.5cm$ and $\approx 1.5s$ of a gap of $3cm$.

These numbers suggest that for inversion times TI above $\approx 1500ms$ fresh (not-inverted) blood would enter small dynamic vessels. The equilibrium z-magnetization of this blood increases the MR signal. Due to substantial CBF increase during activity, more fresh blood would enter the imaging slice and result in a further signal increase during activation. This signal increase during activation would counteract the negative VASO contrast. Therefore, the measured VASO-contrast would underestimate the change in CBV in this case.

In conclusion, to circumvent CBF contamination of the VASO contrast in the occipital lobe, blood nulling time must be smaller than $\approx 1.5s$ and the inversion slab must come down to the circle of Willis.

Considering the structure and the velocities of blood (see section 3.1.3), the mean residence time of water in a capillary is less than 1 second. This suggests that during a TR of $\approx 1.5s$ the entire blood in the microvessels is expected to be replaced.

5.4.4 Nulled CSF

VASO is based on the assumption that CBV increase is compensated by GM volume decrease. However, it has been shown that functional changes in CSF volume can have a significant impact on the conventional blood-nulled VASO signal [Piechnik et al., 2009], [Scouten and Constable, 2008], [Donahue et al., 2009a]. These studies show that partial CSF volume can show dynamic changes in voxels containing activated tissue.

In traditional VASO, where steady-state blood is nulled, CSF z-magnetization is negative and GM z-magnetization is positive. If there is a notable decrease of CSF volume fraction in a voxel, the relative VASO signal change is expected to be smaller than in a voxel containing GM only, leading to an underestimation of relative change in CBV. For further discussion on the topic see section 8.10. The mechanism behind the dynamic change of CSF volume is not completely understood. It is not clear where the CSF volume that leaves the voxel goes. It has been shown that even a small bolus injection of fluid into CSF space of $4ml$ can cause a temporary doubling of intracranial pressure [Czosnyka et al., 2004] according to Monro-Kellie doctrine (see section 3.2). This suggests that dynamic change in CSF is not associated with CSF inflow or outflow of the cranium.

A favorable feature in slab-selective VASO is that the mentioned CSF contamination can be circumvented by nulling both compartments blood and CSF. Since stationary CSF is in steady-state and flowing blood has been inverted only once, there is a repetition time TR where both blood and CSF are nulled. This is also represented by the fact that CSF z-magnetization in Fig. 5.5 (b) crosses the abscissa at $TR \approx 3.5$. The magnetization evolution for this set of parameters is depicted in Fig. 5.7

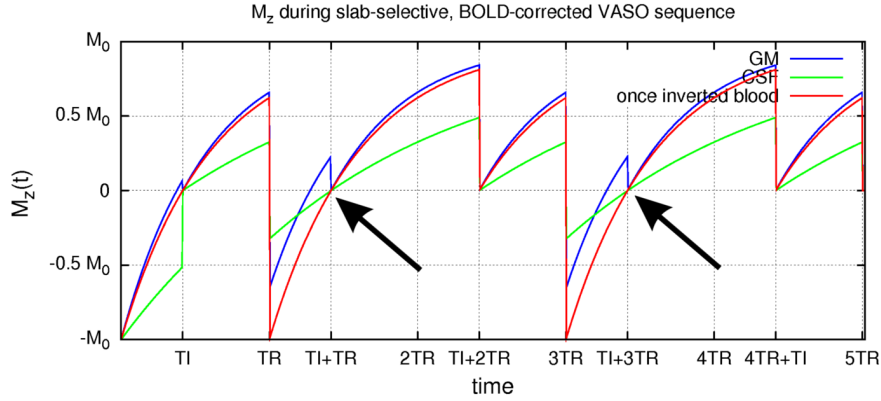


Figure 5.7: The evolution of GM, blood and CSF z-magnetization for a set of TR and TI where both blood and CSF are nulled. Note the image acquisition at $TI + TR$ and $TI + 3TR$ (arrows). The relative VASO signal change in such a sequence is directly proportional to changes in CBV, independent of possible CSF contamination.

In the case of lower TR, CSF z-magnetization is above zero and smaller than GM z-magnetization in the slab-selective sequence (see Fig. 5.5 (b)). Since the proton density is higher in CSF than in GM [Scouten and Constable, 2008], the relative signal is comparable in GM and in CSF. In other words, $1ml$ of CSF gives similar signal intensities as $1ml$ of GM at the blood nulling time. Therefore, if a part of CSF volume in a certain voxel is replaced with GM volume during activation, it does not result in a substantial signal difference. In traditional VASO, however, GM signal is positive while CSF signal is negative. This is associated with a larger impact of functional change in CSF volume on the VASO signal. Hence, slab-selective VASO is less susceptible to CSF contamination compared to traditional VASO for any set of sequence parameters.

5.5 Determination of GM Fraction of a Voxel in the BOLD-Corrected VASO Sequence

5.5.1 Introduction

To determine the relative change in $\frac{\Delta CBV}{CBV_{rest}}$ from the relative VASO signal change $\frac{\Delta S}{S_{rest}}$ of a certain voxel, the amount of blood volume in the voxel CBV_{rest} must be known. VASO detects CBV changes in grey matter and the CBV_{rest} fraction in grey matter can be taken from the literature (see Tab. 5.2). Hence, in order to determine the relevant CBV_{rest} in a voxel, the GM fraction within that voxel must be estimated.

Various segmentation algorithms have been proposed to make binary or non-binary (fractional volume or probability) maps for different brain tissue types, such as GM.

Some VASO-studies use binary masks with the same resolution as the functional images [Donahue et al., 2010] [Hua et al., 2009]. In [Cohalan, 2009] high resolution anatomical images are used to construct a threshold-based high resolution binary GM mask. The GM volume fraction is then determined by comparing the GM mask with the functional low resolution image. In this scheme the GM fraction is determined by looking at how many GM voxels from the high resolution image overlap with one voxel of the low resolution functional image. Most of the VASO studies do not determine CBV changes, but rather look only at signal changes, which are proportional to changes in CBV and the corresponding z-scores. This ignores the constant of proportionality for quantification of CBV changes [Scouten and Constable, 2007] [Lu et al., 2003] [Donahue et al., 2009b] [Donahue et al., 2006] [Donahue et al., 2009a] [Lu and van Zijl, 2005] [Yang et al., 2004] [Poser and Norris, 2011] [Scouten and Constable, 2008] [Jin and Kim, 2008].

One big issue in generating a GM mask at 7T is that the functional EPI-images are distorted and blurred due to B_0 inhomogeneities and T_2^* relaxation effects (see also section 2.2.4). Hence, a grey matter voxel in a GM mask, derived from a high resolution anatomical image, may not overlap with a grey matter voxel of the functional image (see Fig. 5.8).

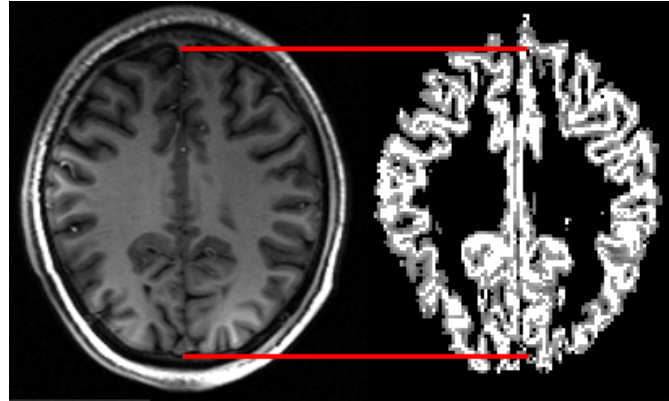


Figure 5.8: Anatomical T_1 -weighted image with no detectable distortions (left) and a GM mask derived from an EPI image with distortions (right). The EPI image is acquired with the same acquisition parameters as the functional data. It is apparent that not all GM voxels of the EPI GM mask (right) overlap with the GM in the high resolution of the anatomical image (left).

The simplest way to avoid the varying distortion level in images is to generate the GM mask with acquisition parameters identical to the functional images. In this way, the GM mask would have distortions identical to the functional image.

Here, a simple GM segmentation method based on quantitative longitudinal relaxation time T_1 is developed.

5.5.2 Theoretical Signal Composition at the Blood-Nulling Point

To understand the dependencies and the effect of GM mask generation, a mathematical description of the signal composition is introduced. The signal composition of an inversion recovery sequence at the inversion time TI can be considered in a three compartment model as:

$$S(TI) \propto \rho_{wm} V_{wm} M(TI)_{wm} e^{-\frac{TE}{T_2^*_{wm}}} + \rho_{gm} V_{gm} M(TI)_{gm} e^{-\frac{TE}{T_2^*_{gm}}} + \rho_{csf} V_{csf} M(TI)_{csf} e^{-\frac{TE}{T_2^*_{csf}}} \quad (5.12)$$

Where ρ_i denotes the proton density, V_i denotes the volume fraction in a voxel and $M(TI)_i$ denotes the z-magnetization of the compartment $i \in \{wm, gm, csf\}$. To simplify the terms, Eq. 5.12 is rewritten as:

$$S(TI) \propto U_{wm} M(TI)_{wm} + U_{gm} M(TI)_{gm} + U_{csf} M(TI)_{csf} \text{ with } U_i = \rho_i V_i e^{-\frac{TE}{T_2^*_{i}}} \quad (5.13)$$

The desired quantity is the relative signal fraction of GM $S(TI)_{gm}$.

$$S(TI) = S(TI)_{wm} + S(TI)_{gm} + S(TI)_{csf} \quad (5.14)$$

It is often useful to consider normalized signals. The signal intensity can be normalized with the maximum possible signal intensity S_0 with fully relaxed z-magnetization.

$$\frac{S(TI)}{S_0} = U_{wm} \frac{M(TI)_{wm}}{M_0} + U_{gm} \frac{M(TI)_{gm}}{M_0} + U_{csf} \frac{M(TI)_{csf}}{M_0} \quad (5.15)$$

$$U_{wm} + U_{gm} + U_{csf} = 1$$

Steady-State z-Magnetization

The steady-state magnetization in the proposed VASO-sequence can be calculated in dependence of flip angle α , inversion efficiency ξ , inversion time TI , repetition time TR and the longitudinal relaxation times T_1_{wm} , T_1_{gm} and T_1_{csf} . Figure 5.9 depicts the steady-state magnetization for a flip angle of $\alpha = 90^\circ$ schematically.

The relaxation of z-magnetization can be calculated with the Bloch equation (Eq. 2.11).

$$M(t)_i = M_0 - e^{-\frac{t}{T_1}_i} (M_0 - M(t=0)_i) \text{ with } i \in \{WM, GM, CSF\} \quad (5.16)$$

The z-magnetization after TR is then:

$$e^{-\frac{TI}{T_1}_i} \left\{ 1 + \chi_i \left[1 - e^{-\frac{TR-TI}{T_1}_i} \left(1 - \cos(\alpha) \left\{ 1 - e^{-\frac{TR}{T_1}_i} [1 - \cos(\alpha) M(TI - 2TR)_i] \right\} \right) \right] \right\} \frac{M(TI)_i}{M_0} = 1 - \quad (5.17)$$

χ_i denotes the ratio between the z-magnetization before inversion to the z-magnetization after inversion. It is associated to the inversion efficiency ξ by Eq. 6.1 assuming the

adiabatic condition is met, $\chi_i \approx e^{-\frac{\text{pulse duration}}{T_2^i}}$ (see section 6.1.5). χ is usually close to 1. In steady-state $M(TI + 2TR)_i = M(TI)_i$. With this, Eq. 5.17 can be expanded to

$$\begin{aligned} & \frac{M(TI)_i}{M_0} \left[1 + \chi_i \overbrace{\cos(\alpha)^2}^{\ll 1} e^{-\frac{2TR}{T_1^i}} \right] = \\ & = - \underbrace{(1 + \chi_i) e^{-\frac{TI}{T_1^i}} + 1 + \chi_i e^{-\frac{TR}{T_1^i}}}_{\text{no } TI\text{-dependence}} + \cos(\alpha) \left(e^{-\frac{2TR}{T_1^i}} - e^{-\frac{TR}{T_1^i}} \right) \end{aligned} \quad (5.18)$$

The flip angle α is desired to be $\approx 90^\circ$. Due to B_1 inhomogeneities this angle will vary around 90° . Therefore $\cos(\alpha)^2$ is expected to be much smaller than 1.

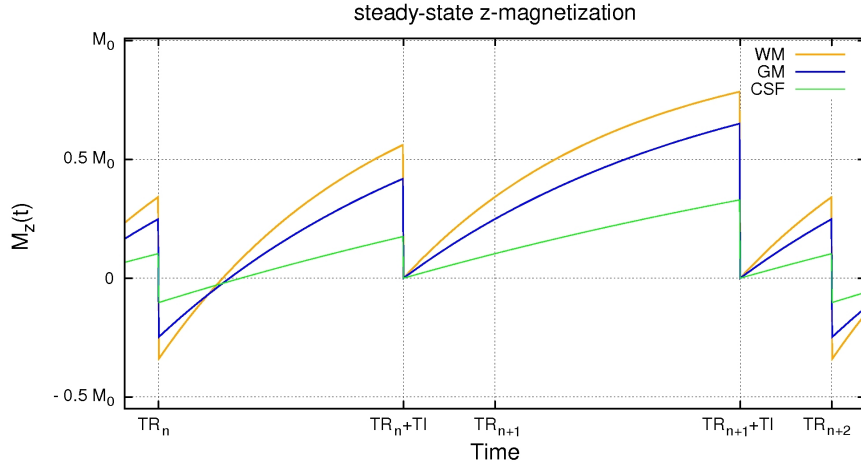


Figure 5.9: WM, GM and CSF steady-state z-magnetization in the proposed VASO sequence.

Figure 5.10 depicts the expected value of the z-magnetization described by Eq. 5.18 as a function of TI for WM, GM and CSF. Since the MR signal is proportional to the absolute value of the z-magnetization, the absolute values of the z-magnetization are depicted. Equation 5.18 can be rearranged to create a form similar to exponential decay.

$$\frac{M(TI)_i}{M_0} = - \frac{1 + \chi_i}{1 + \chi_i \cos(\alpha)^2 e^{-\frac{2TR}{T_1^i}}} e^{-\frac{TI}{T_1^i}} + \underbrace{F(TR, \alpha, T_{1i}, \chi_i)}_{\text{no } TI\text{-dependence}} \quad (5.19)$$

In the style of [Shin et al., 2010] a T_1^* is introduced.

$$\frac{M(TI)_i}{M_0} = -e^{-\frac{TI}{T_{1i}^*}} + F(TR, \alpha, T_{1i}, \chi_i)$$

$$\text{with } \frac{1}{T_{1i}^*} = \frac{1}{T_{1i}} + \ln \left(\frac{1 + \chi_i \cos(\alpha)^2 e^{-\frac{2TR}{T_{1i}}}}{(1 + \chi_i)TI} \right) \quad (5.20)$$

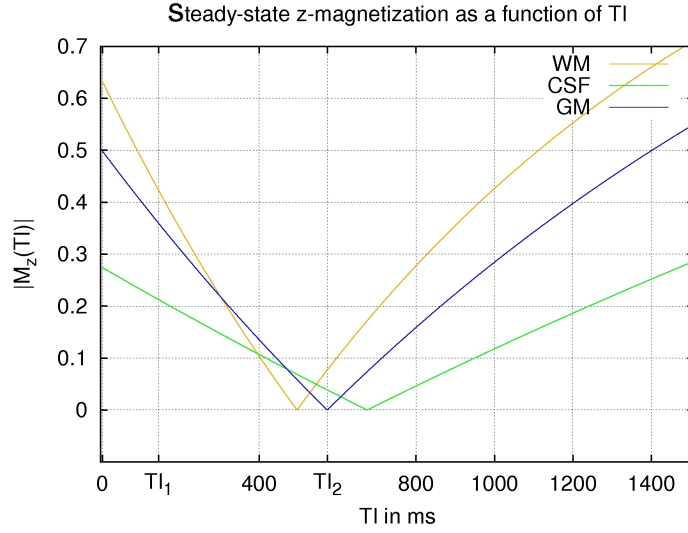


Figure 5.10: Absolute value of the z-magnetization in the proposed VASO-sequence as a function of TI . In this figure α is assumed to be 90° . According to Eq. 5.18 a flip angle $\alpha \neq 90^\circ$ would only lead to a constant horizontal offset of the depicted curves. TI_1 and TI_2 denote a set of inversion times that are associated with the same ratio of $\frac{|M(TI)_{wm}|}{|M(TI)_{csf}|}$.

5.5.3 A Simple Fast Way of Determining GM Fraction

The notable feature of Eq. 5.18 is that TI -dependence can be completely separated from the dependence of TR and α . The normalized signal difference of compartment i is only dependent on TI .

$$\frac{S(TI_1)_i - S(TI_2)_i}{S(TI_1)} = \frac{M(TI_1)_i - M(TI_2)_i}{M(TI_1)} = \frac{\Delta M_i}{M(TI_1)} \stackrel{\text{Eq. 5.18}}{=} \frac{e^{-\frac{TI_1}{T_{1i}}} - e^{-\frac{TI_2}{T_{1i}}}}{e^{-\frac{TI_1}{T_{1i}}}} \quad (5.21)$$

This fact can be employed to generate GM-masks without any knowledge of the flip angle α or the inversion efficiency χ_i . The inversion times used can be optimized to take advantage of the fact that only a GM-mask is needed and not a WM-mask or a CSF-mask. The idea is that the WM- or CSF-fraction in the voxel could have the same

relative signal change, while the GM-induced signal change is maximized. Let's consider the two inversion times TI_1 and TI_2 , which are depicted in Fig. 5.10. At both inversion times, the ratio of the two compartments is the same.

$$\frac{|M(TI_2)_{wm}|}{|M(TI_1)_{wm}|} = \lambda = \frac{|M(TI_2)_{csf}|}{|M(TI_1)_{csf}|} \quad (5.22)$$

Grey matter, on the other hand, has a different relative signal change $\frac{|M(TI_2)_{gm}|}{|M(TI_1)_{gm}|} < \frac{|M(TI_2)_{wm,csf}|}{|M(TI_1)_{wm,csf}|}$. A sample image of the relative signal change is depicted in Fig 5.11.



Figure 5.11: An example of the relative signal change is depicted. One can see how GM stands out from WM and CSF.

To determine the GM fraction of a voxel, the full three-compartment-model (Eq. 5.13) is considered.

$$\frac{\Delta S}{S_0} = \frac{S(TI_1) - S(TI_2)}{S_0} = \frac{U_{gm}\Delta M_{gm} + U_{wm}\Delta M_{wm} + U_{csf}\Delta M_{csf}}{M_0} \quad (5.23)$$

Since TI_1 and TI_2 are chosen in a way that $\frac{\Delta M_{wm}}{M_0} = \frac{\Delta M_{csf}}{M_0}$, Eq. 5.23 can be simplified.

$$\frac{\Delta S}{S_0} = \frac{U_{gm}\Delta M_{gm} + (U_{wm} + U_{csf})\Delta M_{wm,csf}}{M_0} = \frac{U_{gm}\Delta M_{gm} + (1 - U_{gm})\Delta M_{wm,csf}}{M_0} \quad (5.24)$$

Hence, the GM signal fraction is.

$$U_{gm} = \frac{\overbrace{\frac{\Delta S}{S_0}}^{\text{measured}}}{\underbrace{\frac{\Delta M_{gm}}{M_0}}_{\text{calculated}}} = \frac{\overbrace{\frac{\Delta M_{wm,csf}}{M_0}}^{\text{calculated}}}{\underbrace{\frac{\Delta M_{wm,csf}}{M_0}}_{\text{calculated}}} \quad (5.25)$$

The differences in z-magnetization are calculated based on literature values of WM/CSF T_1 and GM T_1 . The term $\frac{\Delta S}{S_0}$ denotes the relative signal change that is measured. U_{gm}

is the desired GM signal fraction that need to be determined in order to estimate the corresponding blood volume at rest CBV_{rest} .

One assumption in this scheme is that every voxel with grey matter contains either GM and WM or GM and CSF, but not all three compartments at once. In a voxel that contains both WM and CSF, the negative z-magnetization of CSF and the positive z-magnetization of WM might cancel each other out at the grey matter nulling point (TI_2). This could result in an overestimation of the grey matter fraction. Human cerebral cortex is 2 – 5mm thick [Kandel et al., 2000]. Therefore, at a voxel size of $1.5 \times 1.5 \times 1.5mm^3$ the assumption is valid for the vast majority of the voxels. The addition of a third image at TI_3 could account for this problem.

To determine the relative change in CBV, knowledge of the GM volume is not enough. The relative GM signal contribution at the blood nulling time $S(TI_{blood\ nulling})_{gm}$ must be considered. This can be extrapolated by means of the signal at the blood nulling point. Since this calculation consists only of relative signal changes, the GM signal contribution can be calculated without any knowledge of the flip angle. Only GM T_1 needs to be taken from the literature. Since, the sequence used is designed to measure M_0 in the first image, there is enough information to determine T_1^* for every voxel in addition to the GM-fraction. A T_1^* -map is depicted in Fig. 5.12 (b).

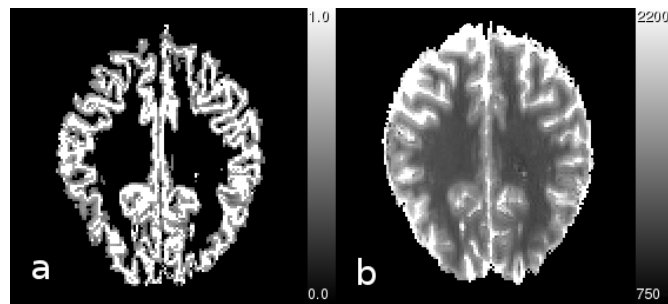


Figure 5.12: (a) Representative image of a mask of the relative GM signal contribution to the functional images at the blood nulling time. (b) Corresponding T_1^* is shown for the sake of comparison.

Experimental Acquisition

The two images to generate the GM mask were acquired with the acquisition parameters identical to the functional images, except for the inversion time TI . To decrease noise, 10 images for both TI were averaged. With the repetition time of $TR = 1.5s$, only 30s scan time is needed. Under some circumstances in pilot measurements, it turned out that the grey matter nulling point is not very stable. To ensure that the grey matter is completely nulled, three additional images were acquired close to the GM nulling point associated with additional scan time of 90s.

6 Sequence Development and Validation

In this chapter, all self developed sequence features are validated. Results from pilot measurements are evaluated and discussed.

6.1 Measurements and Discussion of the Dependencies of the tr-FOCI Adiabatic Inversion Pulse

In order to achieve a proper slab-selective inversion despite B_1 and SAR constraints, a tr-FOCI pulse was implemented. Its performance with respect to efficiency and spatial selectivity is evaluated theoretically and experimentally in detail.

6.1.1 Attributes of an Adiabatic Inversion Pulse

The inversion efficiency ξ is defined as the ratio of the accomplished change of the z-magnetization to the largest possible change of the z-magnetization. The inversion efficiency is $\xi = 100\%$ for full inversion. For fully relaxed magnetization the inversion efficiency is represented as $\xi = \frac{M_0 - M_z \text{ after inversion}}{2M_0}$, i.e. the inversion efficiency of a saturation pulse is $\xi = 50\%$. If the magnetization after the inversion pulse is $M_z \text{ after inversion} = -\chi M_z \text{ before inversion}$, then the inversion efficiency is shown as:

$$\xi = \frac{M_z \text{ before inversion} - M_z \text{ after inversion}}{2M_0} = \frac{1 - \chi}{2} \quad (6.1)$$

Aside from high inversion efficiency, high spatial selectivity is a desired attribute in inversion pulses. The spatial dependence of the inversion efficiency is called inversion profile. To be able to investigate the dependence of the inversion profile on the global pulse parameters, the parameters were kept variable. The variable parameters are discussed in the following sections. These parameters and their major influences on the inversion are:

- **Peak amplitude of the RF-pulse $B_{1 \text{ MAX}}$:** In order to fulfil the adiabatic condition (equation 2.21) $B_{1 \text{ MAX}}$ should be as big as possible. On the other hand, SAR is proportional to the square of the magnetic field. Hence, considering energy deposition $B_{1 \text{ MAX}}$ should be minimized.
- **Frequency sweep μ :** The frequency sweep relates directly to the slab thickness. The frequency sweep should be small in order to fulfil the adiabatic condition (equation 2.21). Apart from that, a larger frequency sweep is correlated with the sharpness of the inversion slab profile.
- **Slab-selective gradient G_s :** The slab-selective gradient determines the slab thickness ($\Delta x = \frac{\Delta\omega}{\gamma G}$).

- **Pulse duration T :** The pulse duration should be long, in order to fulfil the adiabatic condition (equation 2.21). Simultaneously, the pulse duration is proportional to SAR. Considerations of T_2 relaxation effects suggest that the pulse duration is also connected to the sharpness of the inversion profile.

In order to evaluate the dependencies of the adiabatic inversion pulse, the inversion profile was investigated as a function of these pulse variables. These validation measurements are realized using an oil phantom in order to minimize B_1 inhomogeneities. The relaxation times for this phantom are $T_1 \approx 932ms$ and $T_2 \approx 37ms$. More details of the experimental setup are described in section 7.1.

To validate the technical implementation of the pulse, the inversion profile was acquired with identical pulse parameters, as used in [Hurley et al., 2010]. The pulse duration is $5ms$. The inverted slab is $100mm$ thick.

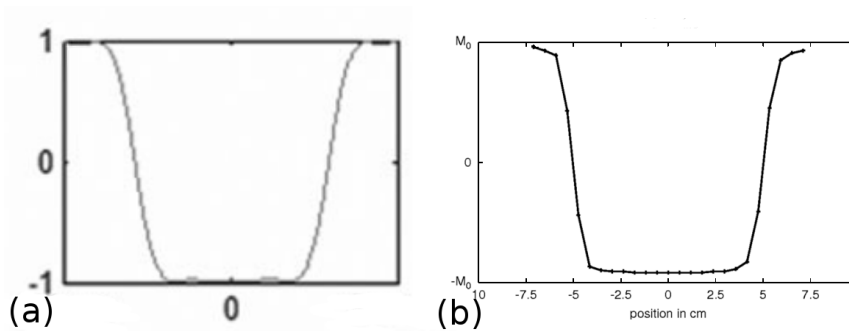


Figure 6.1: (a) depicts the slice profile of the tr-FOCI pulse with a duration of $5ms$ simulated by Hurley et al. The image is taken from [Hurley et al., 2010] page 56. The abscissa is the position along z-direction in a.u. The ordinate depicts the z-component of the magnetization after the inversion pulse in units of M_0 . (b) depicts the measured slice profile in oil of the implemented tr-FOCI pulse, with the same pulse parameters. The sharpness of the profiles in (a) and (b) is similar.

6.1.2 RF Pulse Magnitude B_1

Measurements and Discussion Figure 6.2 depicts the measured inversion profiles for several magnetic field strengths B_1 in oil. The sharpness of the slab profile is almost unaffected by B_1 . The inversion efficiency is highly dependent on B_1 , especially for small B_1 values.

The adiabaticity $\beta = \frac{|\gamma \vec{B}_{eff}|}{|\frac{d\psi}{dt}|}$ (see equation 2.22) is directly proportional to B_1 . Since the adiabatic condition (equation 2.21) is not fulfilled for very small B_1 values, this can explain the poor inversion efficiency at low B_1 magnetic fields. As long as the adiabatic condition is fulfilled, the inversion efficiency is independent of B_1 . The inversion efficiency is almost 95% for B_1 values above $7.8\mu T$ (30% of $25.91\mu T$). This is in accordance with

the literature, where a threshold of the adiabatic condition is simulated to be around $7\mu T$ for a tr-FOCI pulse [Hurley et al., 2010].

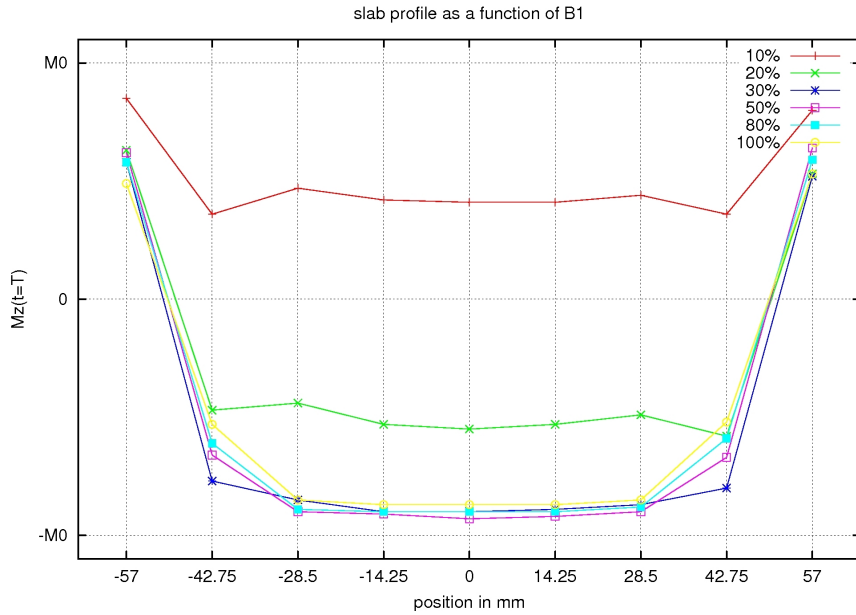


Figure 6.2: Slab profile of the tr-FOCI pulse as a function of the magnetic field strength B_1 in oil. It is apparent that the inversion efficiency reaches its maximal level for RF field strengths above $\approx 30\%$ of the reference value of $25.91\mu T$. The precise value of the reference amplitude was set arbitrarily.

6.1.3 Bandwidth μ

The slab profile was measured as a function of bandwidth $\Delta\omega = 2A_{max}\mu\beta$ (see equation 2.28). The reference bandwidth was set to $6.355kHz$. This bandwidth value was found to be optimal for a $5ms$ tr-FOCI pulse in [Hurley et al., 2010]. In order to keep the inversion slab thickness constant for different bandwidths, the gradient strength was adapted respectively.

In order to understand the dependence of the sharpness of the inversion slab on the bandwidth used, the behavior of spins at the margin of the slab is considered. Let's look at the reference frame of a set of spins that experience the same magnetic field (so-called isochromat) at the margin of the slab profile. For these isochromats in the transition zone, the inversion pulse doesn't begin with frequencies much above resonance, as the adiabatic principle would suggest. For these isochromats the effective magnetic field $B_{eff}(t=0)$ points at an angle $\psi \neq 0$ to the z direction at the beginning of the pulse (see Fig. 6.4(a)). The angle ψ between B_{eff} and the z -axis for a spin is given by equation 2.20 as $\psi(z) = \arctan\left[\frac{B_z - \frac{\omega}{\gamma}}{B_1}\right]$. This shows that $\psi \neq 0$ for frequencies not much above resonance. In this case, the cone of precession of the magnetization, which is getting

inverted in an adiabatic inversion pulse, has a big opening angle ψ .

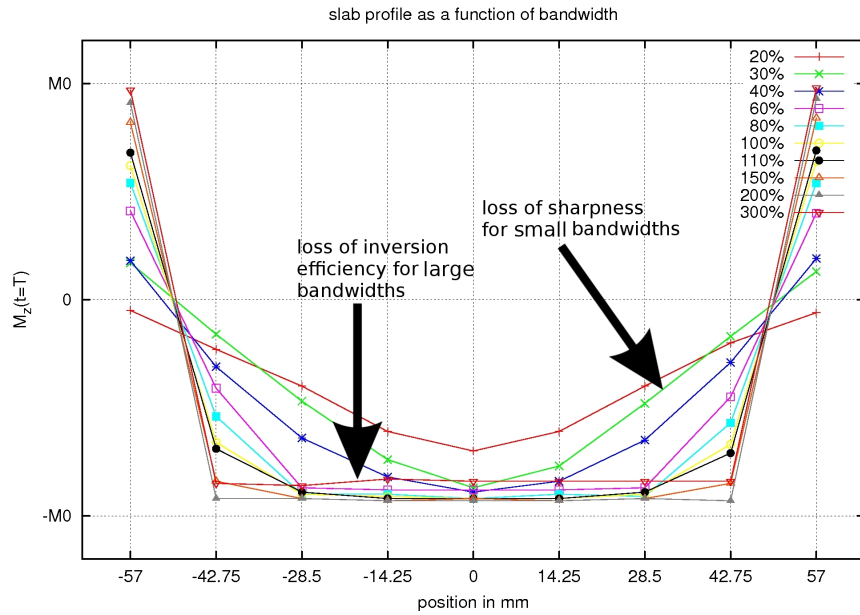


Figure 6.3: Slice profile of the tr-FOCI pulse in oil as a function of the pulse bandwidth μ . The numbers in the captions denote the percentage of the bandwidth. The reference bandwidth (100%) is 6.355kHz . One can see that the inversion profile becomes sharper for higher bandwidths. The inversion efficiency becomes lower for very big and very small bandwidths.

At the end of the inversion pulse the effective magnetic field $B_{eff}(t = T)$ points along the negative z-direction and the magnetization precesses around this field with a wide opening angle (see Fig. 6.4 (b)). Due to this wide opening angle, the z component of the magnetization is small at the end of the inversion. This yields an insufficient inversion. A similar situation holds for spins at the other margin of the inversion slab. In this case the effective magnetic field $B_{eff}(t = 0)$ is rather parallel to the z direction at the beginning of the pulse and the cone of precession has a narrow opening angle (see Fig. 6.4 (c)). However, at the end of the pulse the cone of precession is not fully inverted and still has a large component in the transverse plane (see Fig. 6.4 (d)).

These effects in the transition zone occur for a small range of frequencies $\Delta\omega_{on-res}$. For a given bandwidth the spatial area of spins, where this effect occurs, is given by the gradient strength applied during the pulse.

$$\Delta z_{on-res} = \frac{\gamma G}{\Delta\omega_{on-res}}. \quad (6.2)$$

For a higher frequency sweep, accompanied with a higher gradient, the spatial extent of the transition zone decreases, hence the slab profile becomes sharper. For very low fre-

quency sweeps - less than $1.9kHz$ (30% of reference frequency sweep) the spatial extent of the transition zone becomes as big as the slab thickness (see Fig. 6.3). This effect suggests using large frequency sweeps.

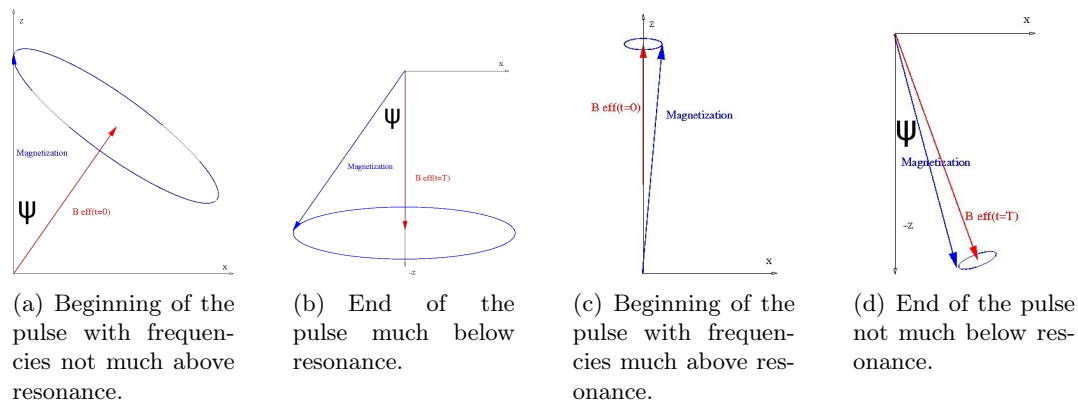


Figure 6.4: Incomplete inversion for spins at the margins of the slab profile, where the RF-frequency is not far off-resonance.

On the other hand, the adiabaticity β decreases with increasing frequency sweeps. According to Eq. 2.22 the adiabaticity is given by $\beta = \frac{|\gamma \vec{B}_{eff}|}{|\frac{d\psi}{dt}|}$. A high bandwidth is associated with a rapidly changing angle ψ and with a low adiabaticity β , respectively. This can explain why the measured inversion efficiency of the pulse decreases again for bandwidths above $12.7kHz$ (200% of reference bandwidth) in Fig. 6.3.

6.1.4 Duration T

The adiabaticity $\beta = \frac{|\gamma \vec{B}_{eff}|}{|\frac{d\psi}{dt}|}$ is directly proportional to the pulse duration T . Hence, in order to meet the adiabatic condition, the duration should exceed a certain threshold. In addition, the energy deposition (SAR) is proportional to the pulse duration T . This further suggests using short pulse durations.

Fig. 6.5 depicts the inversion profiles as a function of pulse duration. The decreasing inversion efficiency for long pulse duration can be explained with relaxation effects during long inversion pulses. These relaxation effects are discussed in section 6.1.5.

One can see in Fig. 6.5 that for short pulses the inversion profile becomes asymmetric. One possible explanation can be an asymmetric shape of the slab-selective gradient pulse. Eddy currents induced in the gradient coils can cause distortions in the gradient waveform. These eddy currents can be induced for many reasons; e.g., the magnet cryoshield [Siemens, 2010]. Technically, the scanner software compensates for these eddy currents by pre-distortion of the gradient waveform, but this compensation may not work properly for short timescales. The eddy current adjustment of the scanner used quantifies

the eddy current decay earliest $2ms$, after gradient switch-off. This suggests that eddy currents that are decayed after $\approx 2ms$ can not be compensated for.

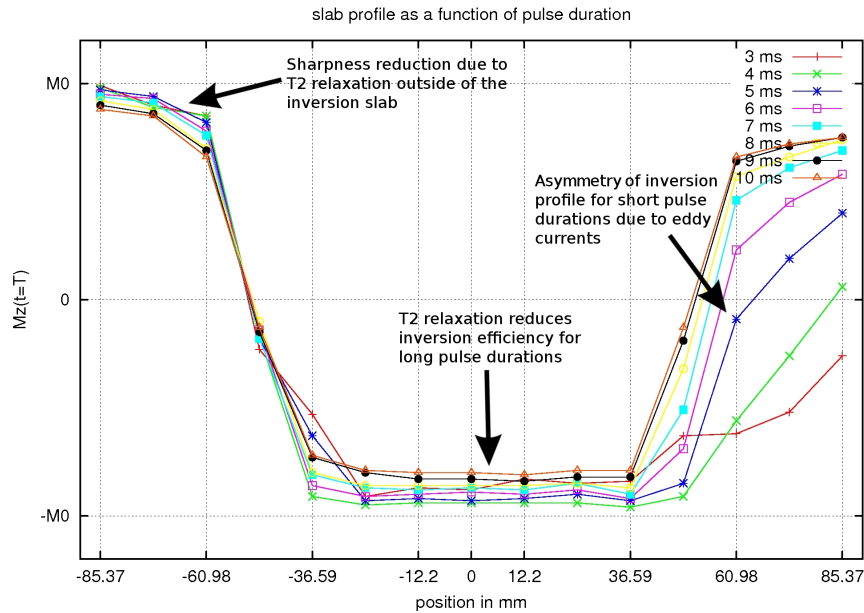


Figure 6.5: Measured slab profile of the tr-FOCI pulse as a function of the pulse duration T in oil. The numbers in the caption denote the pulse duration in ms. The measured inversion efficiency is low for very short durations ($3ms$). It is maximal for $4ms$ and it is decreasing again with longer pulse durations. The measured inversion profile becomes asymmetric for short pulse durations (right margin). The magnetization outside of the inversion slab decreases for very long pulse durations (left margin).

Considering this, pre-distortion can only compensate the effect of the eddy currents up to a certain time constant and the asymmetric slab profile could be explained by an asymmetric gradient waveform.

Figure 6.6 depicts the gradient waveform in the case that the eddy currents are not fully compensated for. The distorted gradient waveform was numerically created by means of the leaky integrator.

$$\frac{dG_{distort}(t)}{dt} = -\frac{1}{\tau} (G_{distort}(t) + G_{input}(t)) \quad (6.3)$$

$G_{distort}$ and G_{input} denote the distorted gradient waveform and the desired gradient waveform respectively. τ denotes the decay time and it is a measure for the distortion.

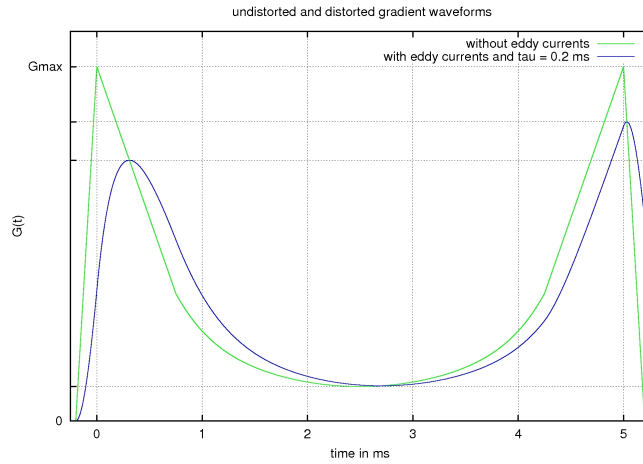


Figure 6.6: Simulated undistorted and distorted gradient waveform. In this generic example the eddy current decay time is $\tau = 0.2\text{ms}$. Real decay time may be even larger.

One can see in Fig. 6.6 that the distorted gradient wave form is asymmetric. The slab profile corresponding to this distorted gradient waveform has been simulated with a Bloch simulation program that is developed in [Helgstrand et al., 2000] and implemented in house by Markus Streicher. The simulated slab profiles are depicted in Fig. 6.7. The figure clearly shows the asymmetry of the distorted profile, similar to the measured profiles in Fig. 6.5.

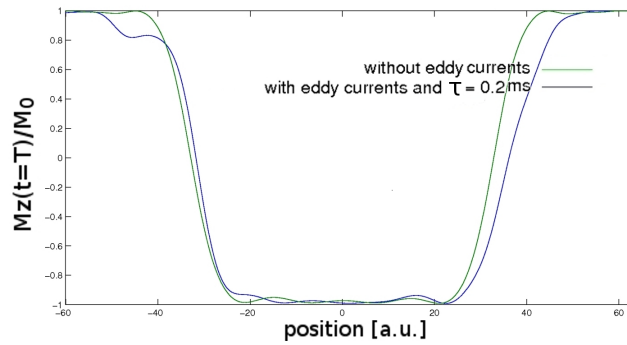


Figure 6.7: Simulated slab profiles corresponding to the undistorted and distorted gradient waveform in Fig. 6.6.

For a constant decay time τ , the distortions have a larger impact on the asymmetry of the profile for shorter pulse durations than for longer pulse durations. This could be a qualitative reason for the strong asymmetry for short pulse durations (see Fig. 6.5).

Sharpness

One can see in Fig. 6.5 that the magnetization outside of the inversion slab is reduced for longer pulse durations. This effect is particularly visible at the left margin. At the right margin this effect is masked by the aforementioned profile asymmetry. The reduced magnetization outside of the inversion slab for long pulse durations can be explained by T_2 -relaxation effects as follows. Let's consider the time-evolution of the magnetization of isochromats with a resonance frequency offset larger than the maximum frequency offset of the pulse at the beginning of the pulse. These isochromats experience an effective magnetic field B_{eff} along the z direction. During the pulse, the effective magnetic field B_{eff} tips into the transverse plane and it returns back to the z direction at the end of the pulse, with smaller magnitude.

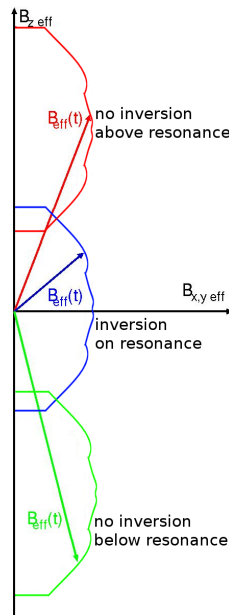


Figure 6.8: Trajectories of the effective magnetic field for three different isochromats in a sweep diagram [Conolly et al., 1989]. $B_{z,eff}$ is given as $B_{z,eff} = B_0 - \frac{\omega}{\gamma}$ and the B_{eff} component in the transverse plane is given as $B_{x,y,eff} = \sqrt{B_{x,eff}^2 + B_{y,eff}^2} = B_1$ in accordance to equation 2.9.

Figure 6.8 depicts the trajectories of the effective magnetic field B_{eff} in a so-called sweep diagram for three isochromats. Sweep diagrams were developed in 1989 by Conolly et al. [Conolly et al., 1989]. The trajectory of the magnetization of an isochromat far above resonance, outside the inversion slab (in red) is shown. The trajectory of the magnetization of an isochromat in the middle of the inversion slab (in blue) is shown, and one below resonance, outside of the inversion slab (in green) is shown respectively. If long pulse durations are used (above $7ms$ in Fig. 6.5), which are comparable to T_2 , the longitudinal magnetization outside the selected slab will be attenuated as a result

of its excursion into the transverse plane with deleterious effects on the slice profile [Norris, 2002]. It would not, however, be affected by the pulse without these relaxation effects.

6.1.5 T_2 -Relaxation During Inversion

During inversion, the effective magnetic field and the magnetization follow a trajectory in three dimensional space. Hence, the magnetization can relax both transversal and longitudinal direction during the inversion pulse. If magnetization relaxes during the pulse, the result is an incomplete inversion. These relaxation effects are considered below.

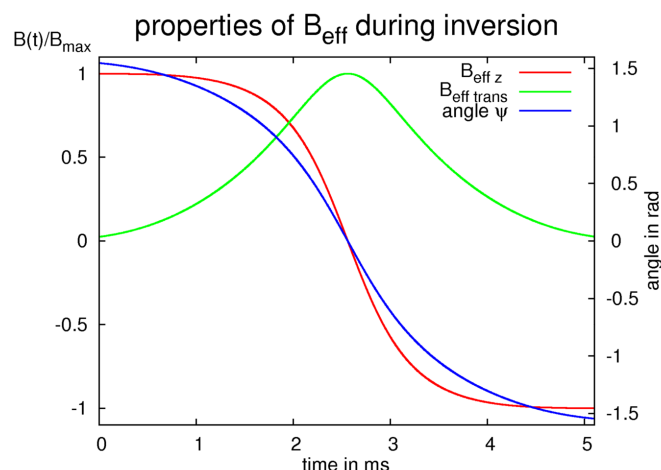


Figure 6.9: Longitudinal and transversal components of \vec{B}_{eff} during the tr-FOCI pulse. The angle between \vec{B}_{eff} and the transverse plane is termed ψ . The simulated pulse duration is $5ms$.

Fig. 6.9 depicts spatial properties of the effective magnetic field \vec{B}_{eff} during inversion. Unlike inversion efficiency, these properties highly depend on B_0 - and B_1 -inhomogeneities. The corresponding magnetization trajectory of this tr-FOCI pulse is depicted in Fig. 6.10. The relaxation constant during inversion consists of an interplay of longitudinal relaxation T_1 and transversal relaxation T_2 , dependent on the orientation of the magnetization. The precise relaxation dependencies of magnetization in \vec{B}_{eff} -direction (\vec{M}_ρ) are expressed in [Taheri and Sood, 2006] for a given orientation in adiabatic pulses:

$$\begin{aligned} \frac{dM_\rho}{dt} &= -\frac{1}{T_{1\rho}} (M_\rho - M_\rho(EQ, \psi)) \quad \text{with} \quad (6.4) \\ \frac{1}{T_{1\rho}(\psi)} &= \frac{1}{T_1} \left(\cos(\psi)^2 + \sin(\psi)^2 \frac{T_1}{T_2} \right) \\ M_\rho(EQ, \psi) &= \frac{M_0 \cos(\psi)}{\left(\frac{\cos(\psi)^2}{T_1} + \frac{\sin(\psi)^2}{T_2} \right) T_1} \end{aligned}$$

$M_\rho(EQ, \psi)$ is the equilibrium magnetization in \vec{B}_{eff} direction for a given orientation with angle ψ . The T_1 -dependence of the relaxation is nearly negligible for pulse durations below $\approx 30ms$.

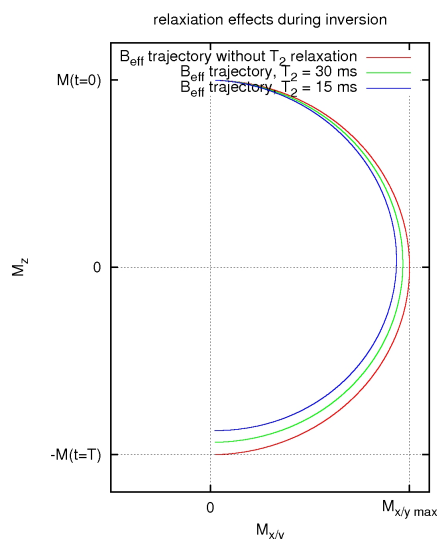


Figure 6.10: Trajectories of magnetization during inversion with and without relaxation. The simulated pulse duration is $5ms$. Assumption underlying the relaxation simulation is $T_1 \gg 5ms$.

The relaxation process during the inversion is determined numerically based on equations 6.4 by solving the differential equation 6.5.

$$M_\rho(t) = - [M_\rho(t - \Delta t) - M_\rho(EQ, \psi(t))] \frac{\Delta t}{T_{1\rho}(\psi(t))} + M_\rho(t - \Delta t) \quad (6.5)$$

Fig. 6.11 shows good compliance between simulated and measured inversion efficiency.

Measuring T_2 :

The dependence of inversion efficiency on the pulse duration due to T_2 -relaxation can be used to quantify T_2 . Recently, two methods were developed that create T_2 -weighted images based on relaxation during adiabatic pulses [Nezafat et al., 2009] [Wang et al., 2011b]. These methods use long BIR-4 pulses and measure the relaxation during the pulse. In this thesis an alternative method of measuring T_2 in a B_1 -independent way is developed. The tr-FOCI pulse is transformed to a spin-lock pulse. Spin-lock pulses allow magnetization to be kept in the transverse plane for certain amount of time by holding the amplitude constant while the frequency is on-resonant [Taheri and Sood, 2006]. This is achieved here by increasing the dwell time during which magnetization is on resonance.

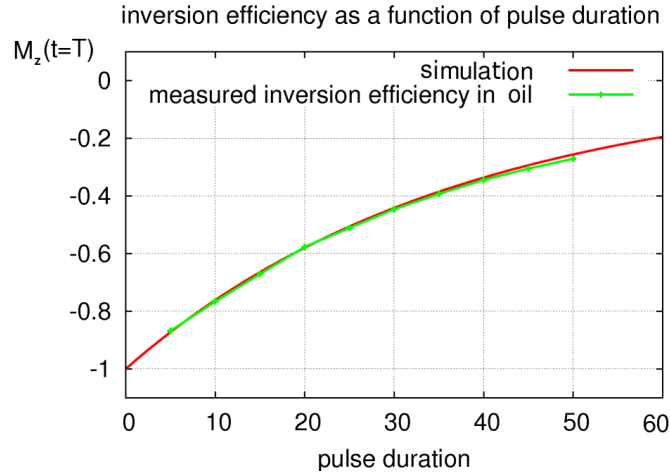


Figure 6.11: Measured and simulated inversion efficiency of an oil phantom with $T_1 = 935ms$ and $T_2 = 36.2ms$.

To minimize T_1 relaxation effects in the time between the adiabatic pulse and the image acquisition ($\approx 10ms$), the frequency modulation is adapted during the second half of the pulse. The frequency is inverted to achieve a magnetization flip back to the positive z-direction instead of an inversion. The adapted pulse amplitude and frequency is depicted in Fig. 6.12.

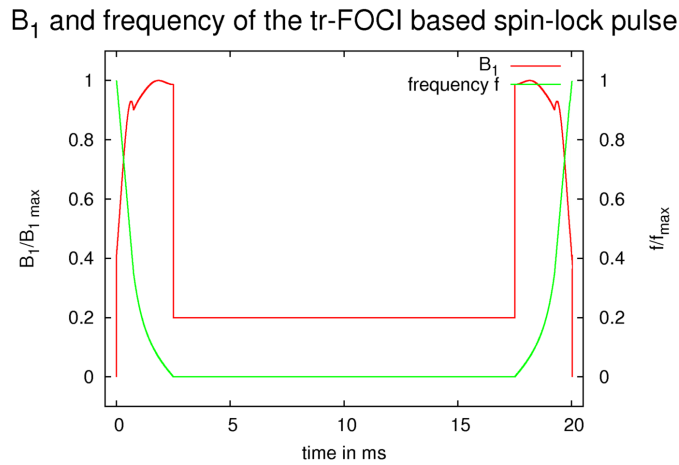


Figure 6.12: Pulse amplitude and frequency of the tr-FOCI based spin-lock pulse. Here the dwell time of the magnetization is $15ms$.

With this RF-Pulse, magnetization is taken from the positive z-direction with a pulse that starts with a frequency significant above resonance ($\approx 3.177kHz$). During the first

2.5ms, frequency is approaching the Larmor frequency and magnetization is tipped into the transverse plane. The magnetization remains there for the dwell time. During the dwell time, the orientation of the magnetization in the rotating frame of reference remains unchanged. Hence, the RF-amplitude B_1 can be reduced without loss in adiabaticity. B_0 -inhomogeneities can affect the Larmor frequency, which would lead to a dephasing of the magnetization during the dwell time. To avoid B_0 -sensitivities, the RF-amplitude is not reduced below a certain threshold. The remaining B_1 -field holds the magnetization in a narrow cone of precession. After the dwell time, the frequency increases again and tips the magnetization back to the positive z-direction.

T_2 can be calculated by comparing the signals of two images after two different dwell times D_1 and D_2 . One signal can be described as:

$$S(D_i) \propto C_a e^{-\frac{D_i}{T_{1\rho}}} C_b \quad (6.6)$$

C_a and C_b denote the relaxation during the first and the last 2.5ms, respectively. According to Eq. 6.4, $T_{1\rho} = T_2$ and the equation of motion is $\frac{dM_\rho}{dt} = -\frac{M_\rho}{T_{1\rho}}$ for the on-resonant case. With this and Eq. 6.6, T_2 is given as:

$$T_2 = \frac{\ln\left(\frac{S_1}{S_2}\right)}{D_2 - D_1} \quad (6.7)$$

This method is completely B_1 -independent above a certain threshold, for which the adiabatic condition is met. Due to the $\sin(\psi)^2$ and $\cos(\psi)^2$ terms in Eq. 6.4, the relaxation is only susceptible to B_0 -perturbations in second order.

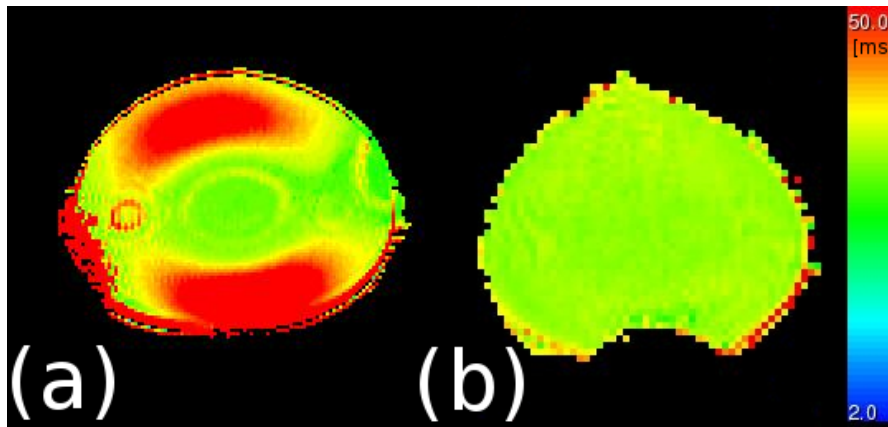


Figure 6.13: (a) T_2 -map generated with a multi spin echo sequence and a subsequent T_2 fit. (b) T_2 -map generated with two images using the described method (b). Figure (a) shows large T_2 -variations in the given range. Figure (b) on the other hand, does not show such large variations in T_2 , but typical EPI-distortions.

Fig. 6.14 depicts a T_2 map in human brain. It shows WM areas in which $T_2 \approx 48ms$.

Almost no GM with a larger T_2 is visible. Since CSF has $T_2 > 120ms$, even a small amount of CSF within the voxel contaminates the T_2 value of the whole voxel.

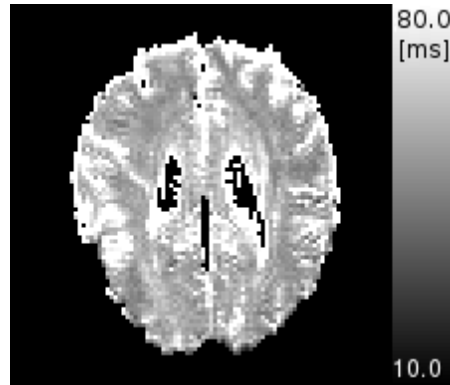


Figure 6.14: T_2 -map in human brain. Calculated from two images with dwell times of $D_1 = 0ms$ and $D_2 = 20ms$.

6.1.6 Position and Thickness of the Slab

According to the Larmor equation 2.7, the slab thickness is given by the bandwidth of the pulse and the gradient waveform.

$$\Delta\omega \underset{\text{Larmor Eq.}}{=} \gamma \frac{\Delta B}{\Delta z} \Delta z = \gamma G \Delta z \quad (6.8)$$

$\Delta\omega$ is given by the pulse parameter $A(0)$, μ , β (see equation 2.28 on page 23). To adjust the slab thickness according blood transit and arrival time in VASO, the gradient strength is adapted. Figure 6.15 illustrates the measured inversion profile for various slab thicknesses. The slab orientation is adjusted in the sample by means of a superposition of gradients in all three directions in space.

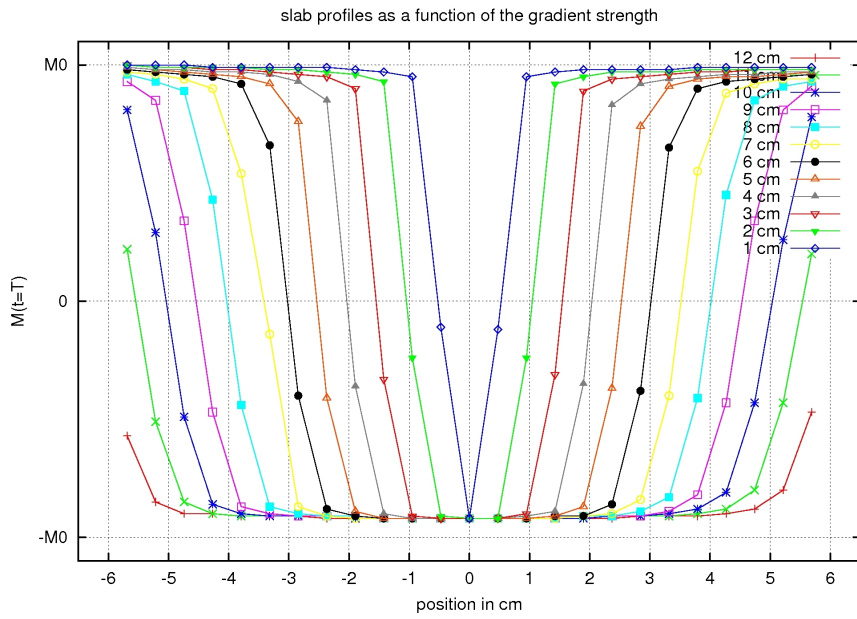


Figure 6.15: Measured slab thickness as a function of gradient strength in oil. One can see how the inversion slab thickness can be adjusted to a desired value without any artifact or the necessity of any kind of trade-off.

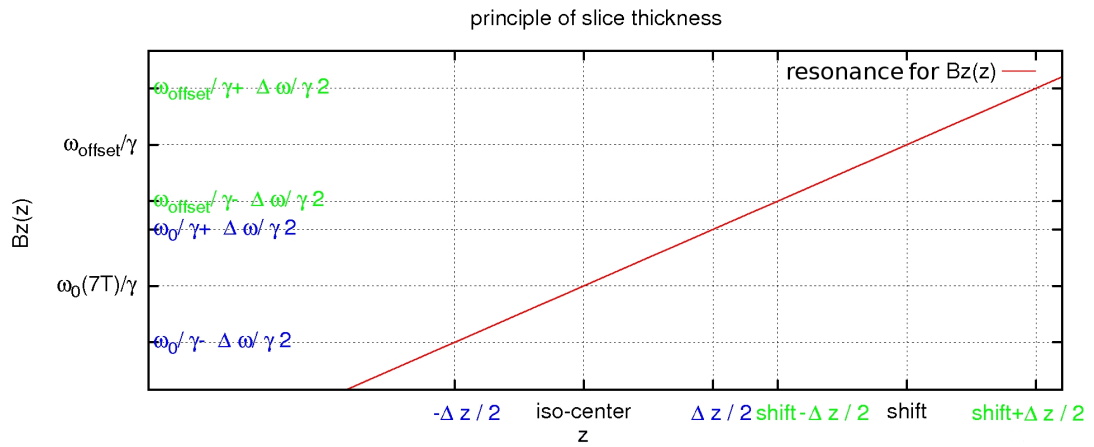


Figure 6.16: Slab position as a function of frequency offset. The ordinate represents the z-component of the magnetic field $B_z = B_0 + Gz$.

The position of the inversion slab along the gradient can be adapted by means of a frequency offset. Figure 6.16 depicts a slab being shifted by introducing a frequency offset, assuming that the gradient strength and the slab thickness remain unchanged.

According to the Larmor equation 2.7 the frequency offset is given by:

$$\omega_{offset} = \omega_0(7T) + \gamma G \cdot shift \quad (6.9)$$

Where $\omega_0(7T) = \gamma B_0$ is the Larmor frequency for the static magnetic field B_0 . For the tr-FOCI pulse, the situation is a little more complicated. Since the gradient strength changes during the pulse, the frequency offset ω_{offset} has to be adapted during the pulse as well. Figure 6.17 depicts how the frequency offset has to be changed in order to keep the slab position and slab thickness unchanged for different gradient strengths.

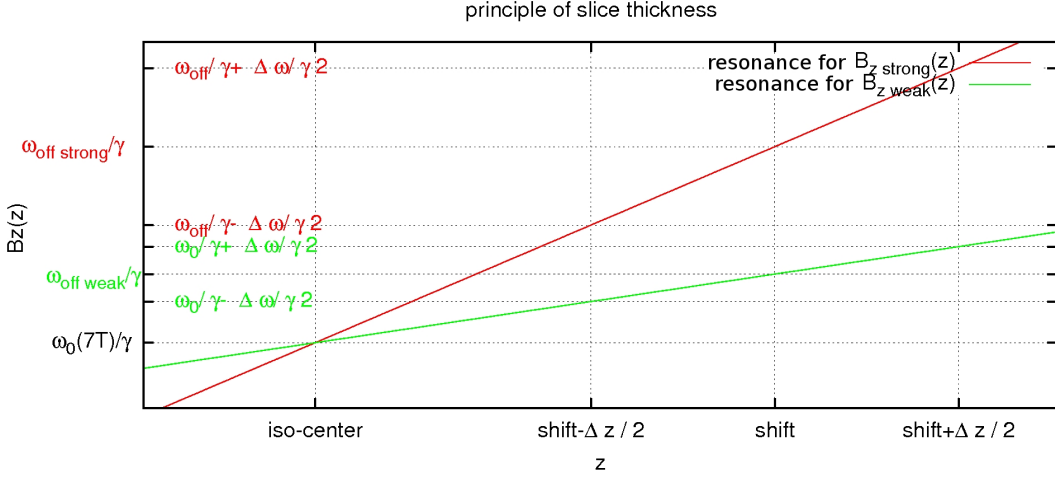


Figure 6.17: Frequency offset as a function of gradient strengths for a desired slab position. $B_z strong$ is defined as $B_z strong = B_0 + G_z strong \cdot z$ and $B_z weak$ is defined as $B_z weak = B_0 + G_z weak \cdot z$. One can see how the frequency offset has to be adjusted along the current gradient strength in order to maintain the same slab position throughout the inversion pulse.

For a slab that is not placed in the isocenter of the MR-scanner, the frequency modulation function $\Delta\omega(t)$ (see equation 2.27) becomes

$$\Delta\omega(t) = -A(t)\mu\beta\tanh(\beta T(t)) \longrightarrow \Delta\omega(t) = -A(t)\mu\beta\tanh(\beta T(t)) + \underbrace{\gamma A(t)G_s}_{G(t)} shift \quad . \quad (6.10)$$

Figure 6.18 illustrates the measured magnetization for several offsets.

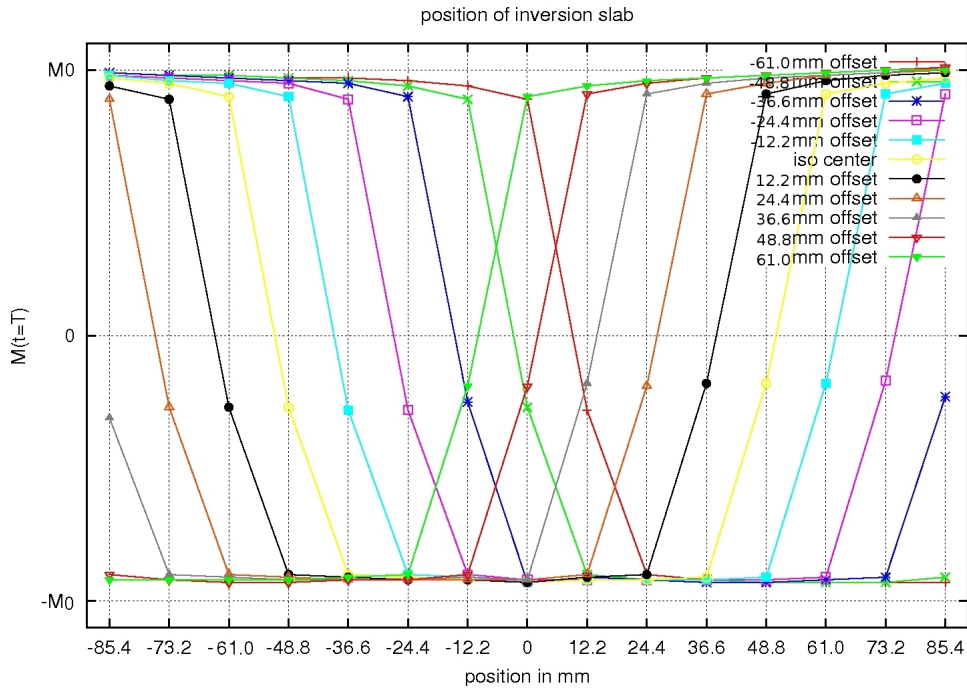


Figure 6.18: Slab position with equidistant offsets. One can see how robust the slab position can be adjusted, indicating that the dynamic frequency offset is implemented properly.

6.1.7 B_1 Measurements

In order to ensure that the RF-amplitude B_1 is strong enough to meet the adiabatic condition, it is essential to be able to measure B_1 . In this thesis a method called actual flip-angle imaging (AFI) [Yarnykh, 2007] is used to determine B_1 . It is a pulse sequence that consists of two identical RF pulses followed by two delays of different duration ($TR_1 < TR_2$) (see figure 6.19). After each pulse, a gradient-echo signal is acquired. It has been shown theoretically and experimentally that, if the delays TR_1 and TR_2 are sufficiently short, the AFI signal is T_1 -independent [Yarnykh, 2007].

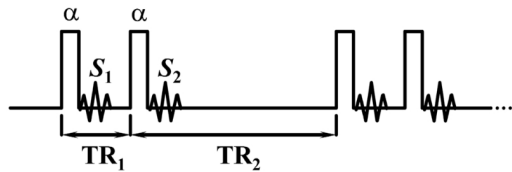


Figure 6.19: Timing diagram of the AFI-sequence. The figure is taken from [Yarnykh, 2007] page 193.

The unique feature of the AFI method is that it uses a pulsed steady-state signal acquisition. This overcomes the limitation of other methods to acquire B_1 that require long relaxation delays between sequence repetitions (e.g. double angle method [Insko and Bolinger, 1993]). An example of a B_1 map acquired with the AFI method is illustrated in figure 6.20.

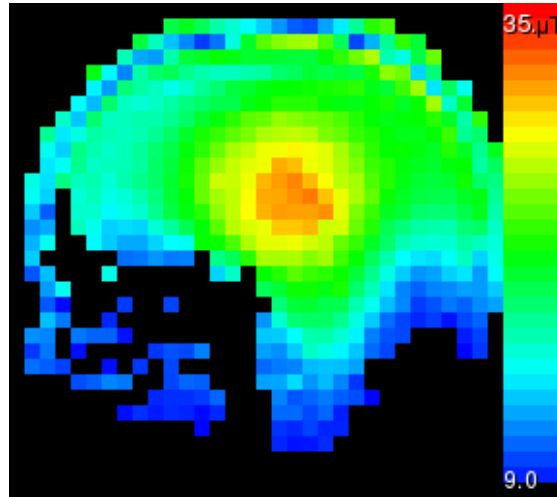


Figure 6.20: Representative B_1 map. The numbers in the caption denote the RF amplitude in μT for a desired magnitude of $25.91 \mu T$. According to pilot measurements (see section 6.1.2), the inversion pulse works properly for B_1 amplitudes above $\approx 8\mu T$. Hence, the magnetization in all colored voxels of this figure is expected to be fully inverted with the tr-FOCI pulse.

One can see that the RF amplitude can be quite small in some regions of the brain. The AFI sequence and the evaluation code were written inhouse by Markus Streicher.

6.1.8 B_1 Sensitivity in a Water Phantom

In order to determine the behavior of the tr-FOCI pulse used, experiments were done under huge B_1 variations. Inversion efficiency measurements were performed with a phantom of water (additives per 1000g H_2O are $1.24g NiSO_4 \times 6H_2O/2.62NaCl$ Siemens Healthcare Sector, Erlangen, Germany). For an accurate determination of the magnetization just after the inversion, an inversion recovery sequence was performed. The signal was acquired at several inversion times TI . The relaxation time T_1 and the inversion efficiency ξ was determined, by fitting the signal to a T_1 relaxation curve $M(TI) = M_0 - e^{-\frac{TI}{T_1}} (M_0 - M(t = T))$. Such a fitting curve is illustrated in Fig. 6.21.

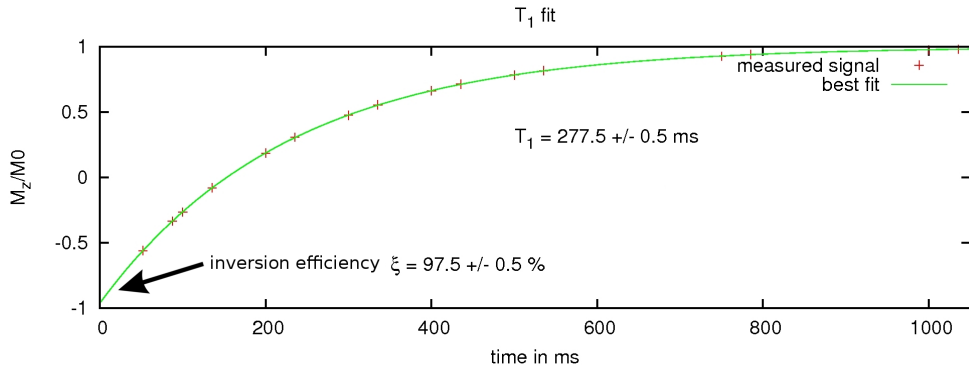


Figure 6.21: T_1 fit, necessary to determine the inversion efficiency. The irregular data sampling along time results from the fact that different slices are acquired interleaved.

Figure 6.22 depicts the slab profile of the water phantom. It can be seen that the inversion efficiency decreases for desired RF amplitudes below $\approx 15\mu T$ (yellow points in figure 6.22), even though the threshold is expected in the range of $\approx 8\mu T$. As it turns out, this is due to high B_1 inhomogeneities perpendicular to z -direction.

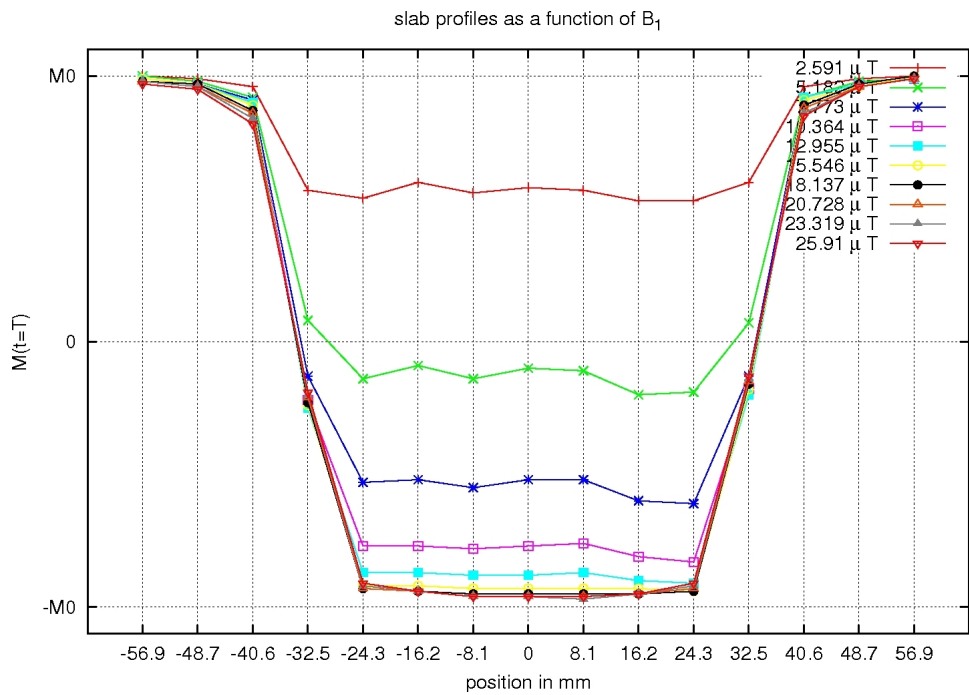
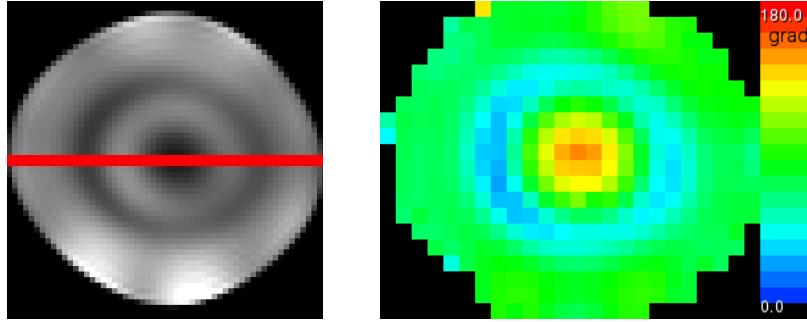


Figure 6.22: Slab profile as a function of RF magnitude B_1 used in a water phantom. The numbers in the caption denote the desired B_1 amplitude.

Figure 6.23 (a) depicts a grey-value EPI-picture with a desired excitation angle of 90° , as it is given in the operating software of the scanner. It shows an obscured ring and center. An AFI B_1 map of the same axial slice is depicted in Fig. 6.23 (b). This B_1 map suggests that the obscured ring is due to low B_1 amplitude in this region. The dark region in the center of the phantom on the other hand seems to be caused by excitation angles far beyond 90° . For flip angles above 90° , the transverse magnetization, which causes the induced MR-signal in the receive coil, decreases again.



(a) Grey-value image of the water phantom.

(b) B_1 map (AFI) of the same slice. The RF amplitude is denoted as flip angles in the caption. The voltage on the coil was adjusted to be 90° .

Figure 6.23: B_1 variations in a water phantom.

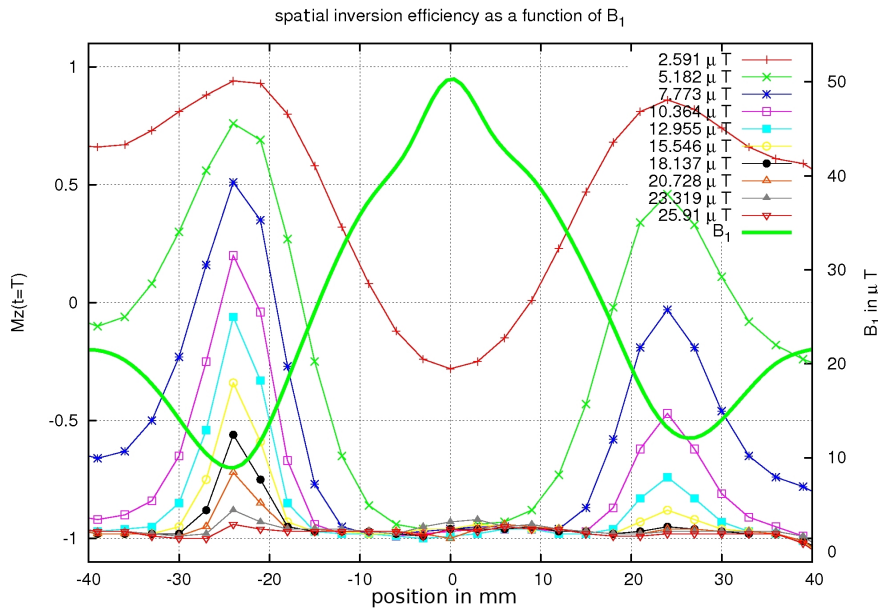


Figure 6.24: Inversion efficiency within one slice as a function of RF magnitude B_1 used.

The inversion efficiency along a transition line (indicated red in figure 6.23 (a)) is depicted in figure 6.24. This comparison can explain why the inversion efficiency decreases for desired amplitudes of $\approx 15\mu T$. Due to large B_1 inhomogeneities, the desired RF-amplitude has to be above $\approx 15\mu T$ to exceed the actual amplitude of $\approx 7\mu T$ at every location. The RF amplitude and the inversion efficiency are a bit lower in the anterior area of the phantom. This results from the fact that the phantom is not placed exactly in the center of the coil.

6.2 Inversion Efficiency and T_1 In Vivo

An inversion efficiency measurement was implemented, in order to confirm that the inversion efficiency is B_1 -independent in the human head. Therefore, the signal intensity was measured at two inversion times (TI_1 and TI_2) and without inversion.

The MR-signal of an inversion recovery sequence with $TR - TI \gg T_1$ is given by:

$$S(TI_{1,2}) \propto M(TI_{1,2}) = M_0 - e^{-\frac{TI_{1,2}}{T_1}} \left(M_0 - \underbrace{M(t=T)}_{-\chi M_0} \right) \quad (6.11)$$

Where $\chi = \frac{-M(t=T)}{M_0}$, according to equation 6.1. T denotes the pulse duration.

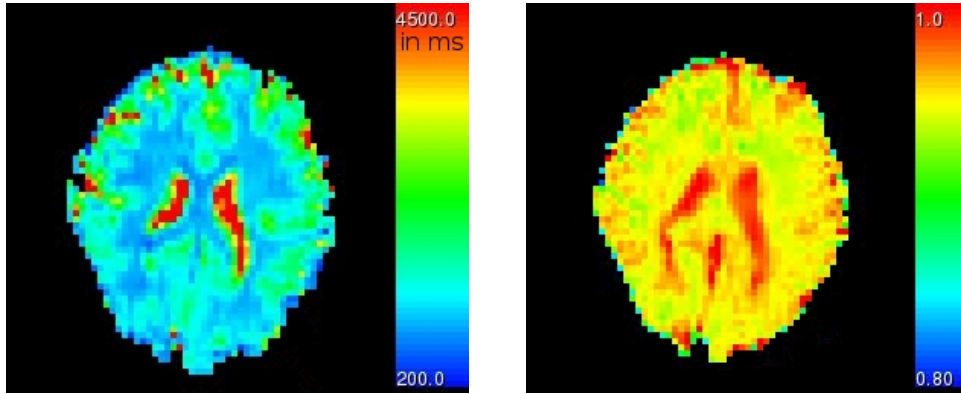
Knowing the signal without inversion, the longitudinal relaxation time T_1 and the inversion efficiency can be calculated. First of all, equation 6.11 for both inversion times are combined to isolate T_1 :

$$T_1 = \frac{TI_2 - TI_1}{\ln \left(\frac{M(TI_1) - M_0}{M(TI_2) - M_0} \right)} \quad (6.12)$$

Inserting this in equation 6.11 results in:

$$\xi \underbrace{=}_{\text{see Eq. 6.1}} \frac{M_0 - M_z \text{ after inversion}}{2M_0} \underbrace{=}_{\text{see Eq. 6.11}} e^{\frac{TI_{1,2}}{T_1}} \frac{(M(TI_{1,2}) - M_0)}{2M_0} \quad (6.13)$$

Figure 6.25 illustrates in vivo maps of T_1 and inversion efficiency ξ in slices that are oriented in a way so that they contain parts of the visual cortex.



(a) T_1 map. The caption denotes T_1 in ms . One can see that T_1_{CSF} is above $3500ms$, T_1_{GM} is in the range of $1900ms$ and T_1_{MW} is in the range of $1100ms$. This is in accordance with the literature (see table 6.1).

(b) Inversion efficiency map. As expected, CSF has larger inversion efficiencies due to the long T_2 values of this compartment (see section 6.1.4). The inversion efficiency is higher than $\approx 90\%$ in all compartments.

Figure 6.25: Results of T_1 and inversion efficiency measurements. Since the primary interest is the global inversion efficiency, rather than the spatial distribution, the images are acquired at low resolution and are slightly smoothed afterwards.

	cortical GM	WM	CSF	blood
[Rooney et al., 2007]	2132(± 103)	1220 (± 26)	4425(± 137)	2587(± 283)
[Wright et al., 2008]	1940(± 150)	1130(± 100)	-	-
[Dobre et al., 2006]	-	-	-	2212(± 53)
[Francis et al., 2008]	1600 (tissue)	1600 (tissue)	-	1950
[Abbas, 2010]	1900(± 150)	1075(± 50)	3700(± 150)	-

Table 6.1: Literature values of T_1 at 7 Tesla in ms .

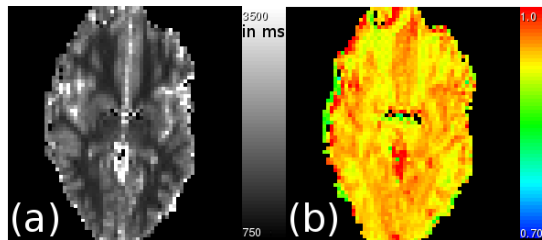


Figure 6.26: T_1 map and inversion efficiency map at the circle of Willis. Variations between 95% and 100% in inversion efficiency result from T_2^* relaxation effects, e.g. areas with high CSF content show high inversion efficiency.

Fig. 6.26 ensures that the RF amplitude is high enough down to the circle of Willis to achieve full magnetization inversion. This is of interest in the slab-selective VASO approach.

6.3 Arbitrary Inversion Efficiency

One problem in a blood nulling sequence can be that the inversion time (TI) is larger than the transit time of blood. RF head-coils only accomplish complete inversion in a confined region of the human head, i.e. blood in the neck of the subject is not fully inverted. If this blood arrives in the imaging slice during TI , not the full amount of blood in the imaging slice is nulled. This suggests the use of smaller inversion times TI . Blood-nulling time can be decreased by decreasing the inversion efficiency. Nonetheless, the inversion efficiency should remain B_1 -independent to counteract the large B_1 -inhomogeneities at high fields.

Here, the tr-FOCI pulse has been adapted in order to invert the magnetization with a predefined arbitrary inversion efficiency.

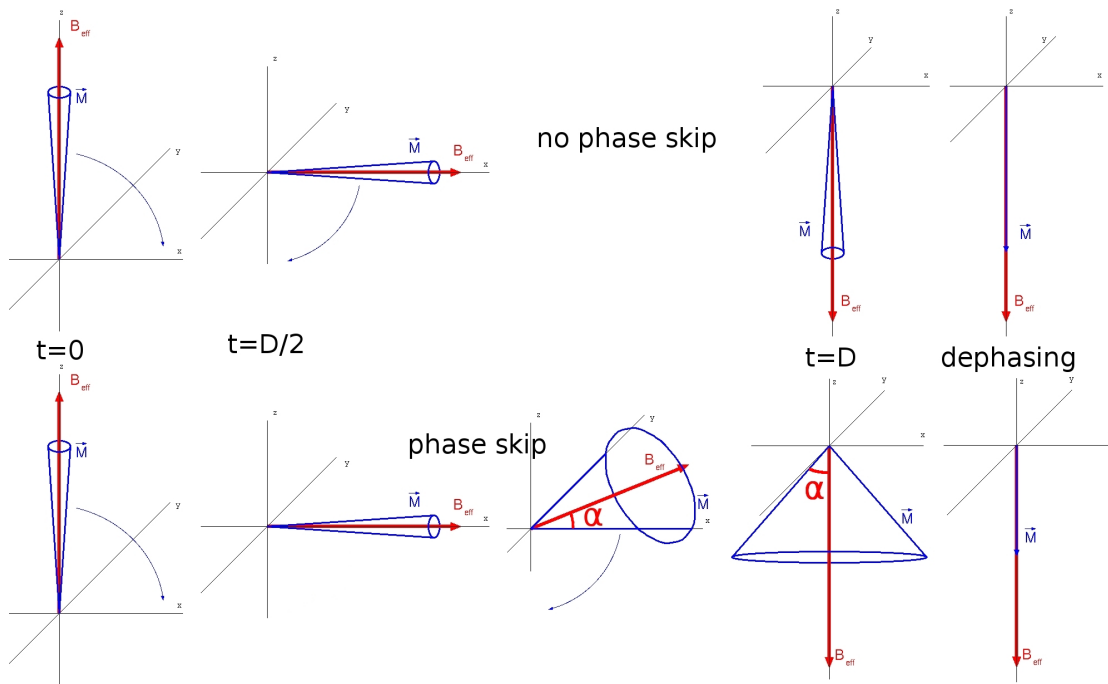


Figure 6.27: Effect of phase skip during inversion.

Figure 6.27 depicts the schematic operating principle of such an inversion pulse. The first row of Fig. 6.27 depicts the evolution of the magnetization during a conventional

adiabatic inversion. The magnetization follows the effective magnetic field \vec{B}_{eff} in a cone of precession with a small opening angle. The second row of Fig. 6.27 depicts the evolution of the magnetization during an adapted inversion. The first half of the pulse is played out in the conventional way. Halfway through the pulse, the RF-frequency is right on-resonance. Hence, the effective magnetic field \vec{B}_{eff} lies in the transverse plane. At this moment a phase skip is introduced. After the phase skip, the magnetization precesses in a cone with a wide opening angle α . During the second half of the pulse this cone of precession is rotated into negative z-direction in the conventional way. Afterwards a dephasing gradient disperses any magnetization not aligned to the z-axis. The magnitude of the inversion after this procedure is expected to be decreased by the factor $\xi = \cos(\alpha)$, where α is the angle of the phase skip. According to Eq. 6.1, the corresponding inversion efficiency is $\chi = \frac{1-\xi}{2}$. Due to the utilization of an adiabatic pulse, this reduction is expected to be independent of B_1 .

$\alpha \setminus B_1$	100%	90%	70%	50%	30%	average reduction ξ	$\cos(\alpha)$
0°	-0.87	-0.87	-0.88	-0.85	-0.90	-	1
60°	-0.43	-0.44	-0.43	-0.45	-0.44	0.50	0.5
90°	-0.01	-0.00	-0.03	-0.01	-0.02	-0.01	0

Table 6.2: Measured M_z/M_0 after inversion for different phase skips and B_1 amplitudes in oil. The standard deviation of all values listed is in the range of ± 0.01 .

Table 6.2 demonstrates that for a 60° -phase skip the longitudinal magnetization is reduced by a factor of 0.501 ± 0.01 . For a 90° -phase skip, the longitudinal magnetization is reduced to 0.01 ± 0.01 compared to conventional inversion. These numbers correspond with the expected values (last column in table 6.2) and there is no detectable B_1 dependence throughout the wide range of RF amplitudes used.

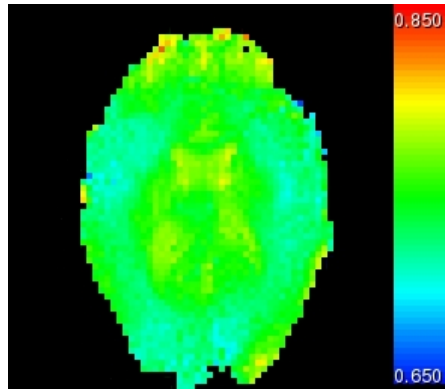


Figure 6.28: Partial inversion efficiency in vivo with a phase skip of 60° .

Figure 6.28 shows that the arbitrary inversion efficiency technique performs well in vivo. The expected reduction of the longitudinal magnetization for the 60° phase skip is $\xi = \cos(60^\circ) = 0.5$, which corresponds to an inversion efficiency of $\chi = 0.75$ (Eq. 6.1). The depicted inversion efficiency corresponds with the expected value. Due to T_2 -relaxation effects (see section 6.1.5) CSF has a slightly higher inversion efficiency than grey matter or white matter.

6.4 Magnetization Transfer

In certain heterogeneous biological environments two types of water molecules, free and bound, are found. Free water protons have a relatively long T_2 and their resonance frequencies lie narrowly around the normal proton resonance frequency of $\approx 297\text{MHz}$ (at 7 Tesla). Apart from that, bounded water molecules have a short T_2 , associated with a broad resonance frequency spectrum. Since the T_2 of bound water protons is approximately $10 - 100\mu\text{s}$, these protons normally do not contribute to MR-signal. The semi-solid component in biological tissue, such as cell membranes, proteins, and lipid bilayers comprises such bound protons [Mehta et al., 1996] [Hua et al., 2009].

However, the free water and macromolecular H_1 populations interact magnetically and undergo a cross-relaxation process consisting of magnetization exchange. This process, called magnetization transfer (MT), can have a detectable effect on MR-signal [Mehta et al., 1996].

6.4.1 MT-VASO

How can blood be distinguished from tissue in MRI? So far two properties of blood are described to get a CBV-contrast in VASO. (a) Blood has a different T_1 from tissue and (b) blood moves into the tissue, while tissue is spatially fixed. An additional feature can be taken into account. Blood has fewer macromolecules compared to tissue and is therefore less sensitive to MT-effects. MT-effects can be used to increase the CBV-contrast of the VASO-Signal [Hua et al., 2009].

The basic idea in MT-VASO is that a far off-resonant RF pulse saturates the z-magnetization of water protons in macromolecules. Since free water has a sharp resonance spectrum, these free water protons remain unaffected from a largely off-resonant RF pulse. Via MT effects, the saturation of the macromolecules in the tissue is transferred to free water in the tissue. In an inversion recovery sequence, this causes a faster recovery of tissue magnetization, when an off-resonant pulse (MT-pulse) is played out right after the inversion [Hua et al., 2009].

The basic assumption in MT-VASO method is that blood inversion time is not affected by the MT-pulse. This assumption has been validated for moderate RF power irradiation ($\approx 2 - 4\mu\text{T}$) and a frequency offset larger than 20ppm in humans [Hua et al., 2009].

However, an additional RF-pulse in the sequence is associated with additional energy deposition in the body (SAR).

If the inversion time TI is only a little bit smaller than the repetition time TR , the

negative z-magnetization after inversion is relatively small. Hence, in this case the MT-induced partial saturation of tissue has only a small effect on the tissue signal. For every set of sequence parameters, a different tradeoff between SAR constraints and maximum signal must be found.

6.4.2 MT-Experiment

In order to investigate the signal increase in MT-VASO, an MT-pulse was implemented for pilot measurements. This off-resonant MT-pulse is used with a corresponding $B_1 \approx 3\mu T$ and a frequency offset of $30ppm$ in accord with [Hua et al., 2011a]. The MT-pulse duration is $90ms$ and it is played out just after the inversion. A slab-selective VASO sequence with $TR = 3s$ and a corresponding blood nulling time of $TI = 1325ms$ is used.

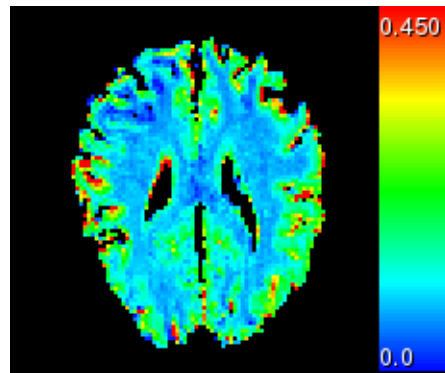


Figure 6.29: The depicted MT-contrast shows the relative signal increase caused by the MT-pulse.

Figure 6.29 depicts the MT-contrast, defined as $\frac{MT\ picture - traditional\ picture}{traditional\ picture}$. Despite the fact that MT effects are stronger in WM than in GM [Mehta et al., 1996], Fig. 6.29 shows a stronger signal increase in GM. This is because z-magnetization of grey matter is comparatively small at the blood nulling time of $TI \approx 1.3s$. Hence, the relative signal increase is larger (see Fig. 6.30). With the sequence parameters used, a grey matter signal increase of $\approx 20\%$ is detected. Despite the GM signal increase, the MT-pulse is not advantageous in this study. The additional energy deposition must be compensated by longer repetition times, associated with a lower temporal resolution. Since one of the aims of this study is investigation of the temporal evolution of CBV, the MT-pulse is not used here.

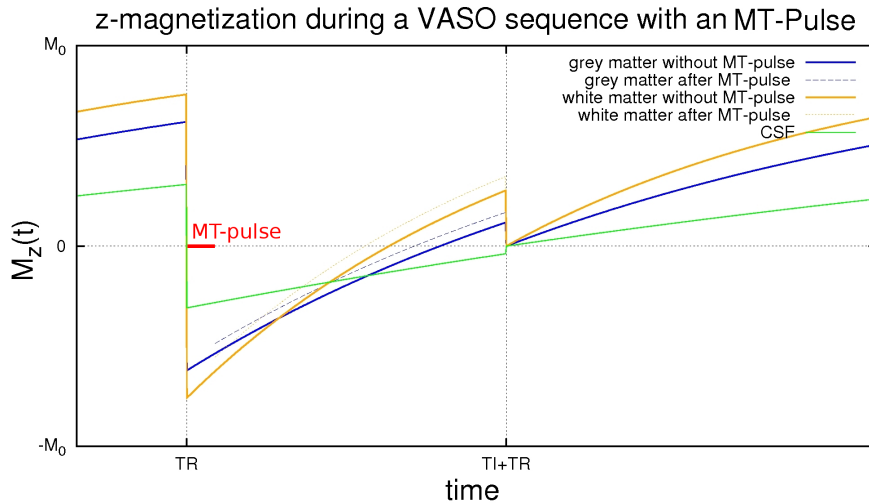


Figure 6.30: Expected steady-state z-magnetization of different compartments during MT-VASO. CSF is expected to be only slightly influenced by the MT-Pulse. White matter is expected to be more affected by the MT-Pulse compared to grey matter. Nevertheless, the relative GM signal increase is higher than the WM signal increase at the inversion times used.

6.5 Experimental Validation of BOLD-Corrected VASO Calculation

During mild hyperoxia, the vasculature and CBV respectively are expected to remain approximately unchanged [Bulte et al., 2007]. On the other hand, the increased O_2 partial pressure during hyperoxia is expected to increase the BOLD signal significantly [Bulte et al., 2007]. In this context, hyperoxia can be used to validate the aforementioned BOLD-correction scheme. Under the assumption that CBV remains unchanged during hyperoxia, the BOLD-corrected VASO signal should not change during hyperoxia, despite the signal change due to the BOLD response. A decrease in BOLD-corrected VASO signal during hyperoxia would imply that the negative MRI-signal response of the BOLD-corrected VASO during activation arises from BOLD over-compensations, rather than from CBV increase. Hyperoxia-induced changes in the partial pressure of CO_2 can reduce CBV (see section 3.3) [Chiarelli et al., 2007]. Hence, for an accurate discussion of the CBV response, the partial pressure of CO_2 has to be measured during hyperoxia as well [Chiarelli et al., 2007] [Mark et al., 2011].

6.5.1 Hyperoxia-Experiment

The BOLD response and the BOLD-corrected VASO-response were measured in one subject, during mild hyperoxia. During the first 2 minutes of the 10 minute experiment the normoxia baseline was measured. After these 2 minutes the subject began breathing

an air mixture containing 50% O_2 for 5 minutes. In the last three minutes, the subject was breathing room air again. The experiment is designed to measure normoxia at the beginning and the end of the experiment, to assess possible signal drifts caused by scanner instabilities. During the whole experiment, the end-tidal partial pressure of O_2 and CO_2 were recorded with a BIOPAC MP150 unit (BIOPAC Systems Inc, Goleta CA, USA) using a pulse oximeter and sampling line connected to the mouthpiece. The experimental setup was arranged inhouse by Dimo Ivanov [Ivanov et al., 2011].

The partial pressure of O_2 at normal pressure ($\approx 760mmHg$) is the product of the pressure with the volume fraction of O_2 ($volume\ fraction\ of\ O_2 \times 760mmHg = partial\ pressure\ of\ O_2$). During hyperoxia the fractional concentration of O_2 increases from ≈ 0.21 (room air O_2 concentration) up to a volume fraction of ≈ 0.5 . This leads to a partial pressure increase from $\approx 160mmHg$ to $\approx 380mmHg$.

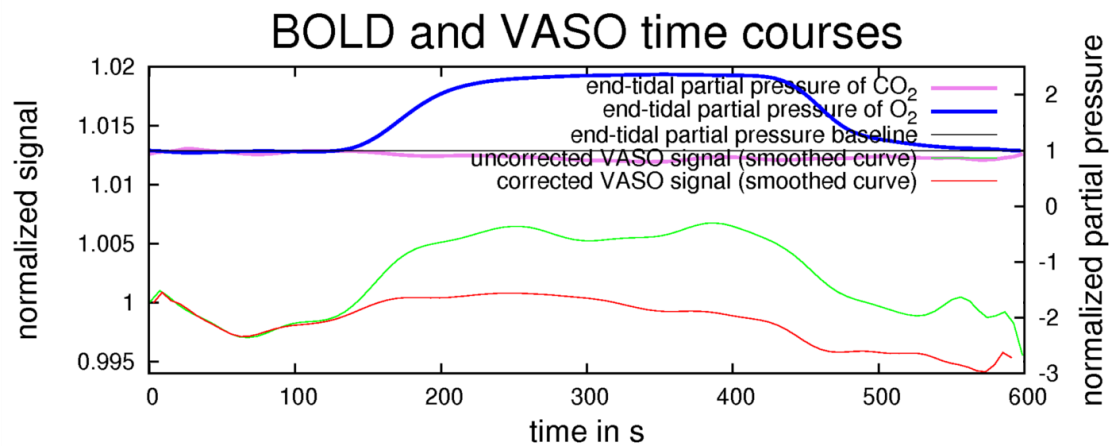


Figure 6.31: Time courses of uncorrected and BOLD-corrected VASO signal and the corresponding time courses of the partial pressures of O_2 and CO_2 . The end-tidal partial pressure baseline of O_2 and CO_2 was set to $154mmHg$ and $40mmHg$ respectively. During the measurement the end-tidal partial pressure of O_2 increased to $\approx 368mmHg$ and the end-tidal partial pressure of CO_2 decreased to a minimum of $\approx 35mmHg$. Due to the transition time, O_2 needs to get from the lungs to the brain tissue and sampling delay from the mouth to the BIOPAC unit, a time delay between the measured partial pressure curves and the MR-signals of $15s$ was introduced. The sequence parameters were $TR/TI/TE = 1.5s/1.3s/10ms$. The signal intensity refers to the mean signal of five slices at a resolution of $3mm$ isotropic. Signal intensity is normalized to the signal intensity at baseline.

Figure 6.31 depicts the time courses of the uncorrected and corrected VASO signal (in green and red) averaged over all voxels and the corresponding partial pressure curves of

O_2 and CO_2 (in purple and blue). It can be seen that the two signals are close together at the first 2 minutes of the experiment. At the start of hyperoxia the uncorrected signal increases simultaneously (considering the time delay of 15s) with the increase in partial pressure of O_2 due to the BOLD effect. This increase in BOLD signal is expected due to the decrease in deoxyhemoglobin during hyperoxia. No significant decrease in the BOLD-corrected VASO signal (red) can be seen. On the contrary, a tendency of an increase in BOLD-corrected VASO signal can be observed. Does this mean that the proposed BOLD-correction of VASO (see section 5.3) is insufficient and the corrected VASO signal is still BOLD contaminated?

6.5.2 Interpretation of an Increase in BOLD-Corrected VASO during Hyperoxia

It has been shown that O_2 is the major contributor to T_1 changes in water induced by paramagnetic molecular oxygen [Zaharchuk et al., 2005]. A CSF- T_1 decrease of $\approx 4\%$ has been suggested while breathing 50% O_2 compared to room air [Zaharchuk et al., 2005]. In the proposed VASO-sequence, this would lead to an increase of steady-state z-magnetization of CSF by $\approx 3.7\%$. Hence, the CSF-fraction in a voxel would increase the signal in the proposed VASO-sequence. This can lead to a small signal increase during hyperoxia despite accurate BOLD-correction.

Even a small decrease of the partial pressure in CO_2 can reduce CBV. Figure 6.31 depicts that the partial pressure of CO_2 decreases slightly during hyperoxia. The accompanying decrease in CBV leads to an increase in VASO signal. No significant dependence of blood T_1 on oxygenation has been observed [Dobre et al., 2006] [Brooks and Chiro, 1987] [Lu et al., 2003].

This argument suggests that the mild increase in BOLD-corrected VASO signal is not caused by an inaccurate BOLD-correction, but by the mild physiological response to hyperoxia. At the time when the partial pressure in CO_2 returns back to baseline, the two signals in Fig. 6.31 converge again.

7 Materials and Methods

7.1 Experimental Setup

All measurements were performed on a 7-T whole-body MR scanner (MAGNETOM 7T, Siemens Healthcare Sector, Erlangen, Germany). A 24-element phased-array head coil (Nova Medical, Wilmington, MA) and a 8-element phased array head coil (Rapid Biomedical, Rimpfing, Germany) respectively were used for signal transmission and reception. Results of pilot measurements suggest that the Nova coil produces better results in this study.

To measure dependencies and limitations of the developed RF-Pulse and the slab-selective, BOLD-corrected VASO-sequence, a repertoire of Phantoms was used:

- Oil phantom provided by Siemens (Siemens Healthcare Sector, Erlangen, Germany). Additives are dimethylpolysiloxan-oil with 1g tris and 0.2g fat color per kg.
- Agar phantom made inhouse by Bibek Dhital. Additives are $dH_2O + 0.7\%NaCl + 1.5\%Agar$.
- Water phantom provided by Siemens; Additives per 1000g H_2O are 1.24g $NiSO_4 \times 6H_2O/2.62NaCl$ (Siemens Healthcare Sector, Erlangen, Germany).

The slab-selective, BOLD-corrected VASO sequence, as well as all other self-developed sequences were implemented by means of the sequence development environment IDEA (Integrated Development Environment for (MR) Applications) from Siemens [Siemens, 2010]. The visual stimulus was diverted from a projector into the bore of the MR scanner by means of a mirror system. The stimulus covered horizontally $\approx 27^\circ$ and $\approx 21^\circ$ vertically of the visual field.

7.2 Parameters of the Slab-Selective BOLD-Corrected VASO Sequence

7.2.1 Parameters of the Inversion Pulse

The inversion was realized with a pulse based on the tr-FOCI pulse [Hurley et al., 2010]. The pulse duration was 5.12ms, the frequency sweep during the pulse was 6.355kHz and the voltage at the RF-coil was adjusted to induce a mean B_1 -amplitude of $\approx 25.1\mu T$. Despite inter-subject B_1 variations, the transmit voltage of the RF-coil remained constant in all subjects, due to SAR limitations.

In preliminary measurements, these parameters were found to be optimal for this study, i.e. to maintain a complete selective inversion despite B_1 -inhomogeneity and SAR constraints. The thickness and position of the inversion slab was set to invert the local magnetization down to the circle of Willis (Fig. 7.1). The slab-selective gradient strength was adjusted to get an inversion slab thickness of 14.28cm . A gradient in z -direction dephases possible residual transverse magnetization after the inversion pulse.

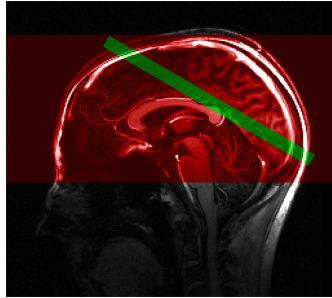


Figure 7.1: Positioning of inversion slab (red) and imaging slices (green).

7.2.2 Parameters of the Sequence

The inversion time TI in the developed sequence was set to the time, where the blood z -magnetization is nulled ($\vec{M}_z^{blood} = 0$). TI can be calculated with Eq. 6.11 to $TI = T_{1\ blood} * \ln(1 + \chi_{blood})$. Anticipating a $T_{1\ blood} \approx 2100\text{ms}$ (see Tab. 5.1) and a blood inversion efficiency of $\approx 94.12\%$, TI is given as $TI = 1328\text{ms}$. The inversion efficiency of $\approx 94.12\%$ was calculated based on the relaxation effects discussed in section (6.1.5). The repetition time in the standard fMRI acquisition was $TR = 1.5\text{s}$. An inversion pulse was played out every 3s (see Fig. 7.2). After the excitation with a desired flip angle of $\approx 90^\circ$, an unaccelerated 2D multi-slice single-shot EPI acquisition without slice gaps was performed. In all VASO acquisitions a field of view of $192 \times 192\text{mm}^2$ and an imaging matrix of 128×128 was used, with 1.5m slice thickness, resulting in $1.5 \times 1.5 \times 1.5\text{mm}^3$ resolution. Five slices were acquired, but only three slices were taken for the functional evaluation. The bandwidth in read direction and in phase direction was $1628\text{Hz}/Px$ and $11.93\text{Hz}/Px$, respectively. The echo time was $TE = 19\text{ms}$, using a partial Fourier factor of $5/8$ to minimize T_2^* -relaxation-effects and image distortions. For fat suppression, an off-resonant (3.5ppm frequency offset) saturation pulse was played out before excitation.

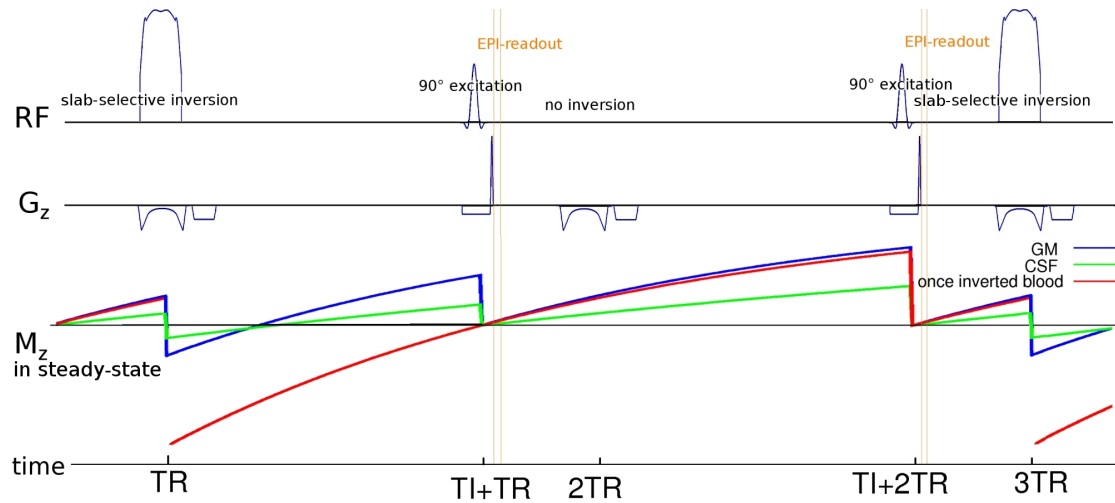


Figure 7.2: Schematic sequence diagram of the slab-selective, BOLD-corrected VASO sequence.

7.3 Session Protocol

- The scan protocol started with an anatomical localizer, followed by shim adjustments. The shim adjustment was used to compensate B_0 -inhomogeneities caused by the susceptibility of the body. The shim parameters remained the same throughout the whole scan session.
- To find the stimulated visual areas within the occipital lobe, a short ($4min$) online BOLD localizer was used.
- The slab-selective, BOLD-corrected VASO measurements lasted $6min$ and was accompanied by visual stimulation. A moving star field paradigm (block design: $30s$ rest vs. $30s$ stimulation) with radially moving stars was used to induce neural activation in the visual cortex. The presentation paradigm of the visual stimulus was based on [Huk et al., 2002].
- Subsequently, a series of measurements was acquired to create a GM-mask and a $T1^*$ -Map (according to section 5.5). The sequence parameters were identical to those used in the BOLD-corrected VASO sequence with a change is the inversion time TI . Eight measurements with durations of $30s$ were taken. The inversion times were $TI = 42ms, 200ms, 350ms, 550ms, 620ms, 690ms, 750ms$ and $1000ms$.
- In all scanning sessions, a whole brain B_1 -Map was acquired with a resolution of $3 \times 3 \times 3mm^3$. The B_1 -map was acquired with an AFI-sequence [Yarnykh, 2007] (see section 6.1.7) implemented inhouse by Markus Streicher. The B_1 -Maps were acquired to ensure whether the blood flowing into the imaging slice within TI is

fully inverted. Therefore the RF amplitude has to be larger than $7\mu T$ down to the circle of Willis. This acquisition took 3:18min.

- An anatomical scan of the same region as the functional slices was acquired with a standard MP RAGE Sequence (data not shown in this thesis). This measurement lasted 2:17min. This measurement was taken to be able to compare possible spatial abnormalities in the functional measurements with anatomical structures.
- The residual time was used differently for different subjects. In all sessions the BOLD-corrected VASO sequence was repeated with small adaptations. In seven subjects the VASO-sequence was repeated with a different stimulation paradigm. To investigate the behavior of CBV after stimulation, the resting period was increased from 30s to 60s in four subjects, so the total measurement is increased from 6min to 9min. With two subjects the stimulation duration is increased from 30s to 60s additionally, so the total measurement was increased from 9min to 12min. To investigate the blood transit time dependencies, the repetition time (TR) was increased to $TR = 2s$, $2.5s$ and $3s$ in two subjects. To investigate the spatial difference of VASO and BOLD, the functional measurements were repeated with a $1 \times 1 \times 1mm^3$ -resolution in two subjects. To achieve this resolution the slice thickness was reduced to $1mm$, the imaging matrix was enlarged to 192×192 and the echo time was increased to $TE = 33ms$. Due to the longer acquisition time per slice of $131.19ms$, the number of slices was reduced to three. The decision in which protocol was applied to each subject was made randomly.

No subject was in the scanner room longer than 90min. All in-vivo studies were carried out with ethics approval from the local university.

7.3.1 Additional Subjects

In addition to the ten subjects, who were scanned with the aforementioned session protocol, four additional subjects were scanned with similar session protocols, to investigate more dependencies of the slab-selective, BOLD-corrected VASO sequence.

- Two of the additional subjects were scanned to look at the blood flow dependence of the slab-selective, BOLD-corrected VASO sequence. In these experiments, all scan parameters remained constant, except for the gradient strength during the inversion. The central plane of the volume of the inversion slab was set to be identical as the middle imaging slice. The gradient was adapted so that the inversion slab thickness was $7cm$, $10cm$, $14cm$, $20cm$ and $\approx 30cm$. This means that blood outside of the inversion slab must overcome $4.5cm$, $5cm$, $7cm$, $10cm$ and $\approx 15cm$ to enter the imaging slice.
- Two of the additional subjects were scanned with a repetition time where both CSF magnetization and blood magnetization was nulled (see 5.4.4). Therefore two measurements of both subjects were taken. The repetition times were $TR = 1.5s$ and $TR = 3.5s$, respectively. All residual scan parameters (e.g. TE, bandwidth,

resolution, TI, position and inversion) remained unchanged. The stimulation and resting periods were increased from 30s to 42s, so both measurements contain an odd number of images for each period. This is helpful for the BOLD-correction scheme.

7.4 Processing of the Functional Data

- **Initial Processing:** The raw data from the scanner were converted into NIfTI (Neuroimaging Informatics Technology Initiative)-files by an inhouse written conversion software from Enrico Reimer. All data were corrected for motion with the evaluation software SPM8 [Penny et al., 2007]. The single images with foregone inversion (blood nulled) and the images without foregone inversion (blood not nulled) were corrected separately because of their differing contrast.
- **T_1^* -Map and Determination of the Spatial Distribution of the three Compartments WM, GM and CSF:** The images that had been acquired with the series of different TI were used to generate WM-, GM- and CSF-masks as well as a T_1^* -Map. The T_1^* -Map was derived with a C++ based evaluation software using a single exponential least squares fit. For matrix inversion in the fitting algorithm, GSL-libraries [Gough, 2009] were used. To include NIfTI-files in the C++ program, ODIN-libraries [Jochimsen and v. Mengershausen, 2004] were used. A representative distribution of T_1^* is depicted in Fig. 7.3.

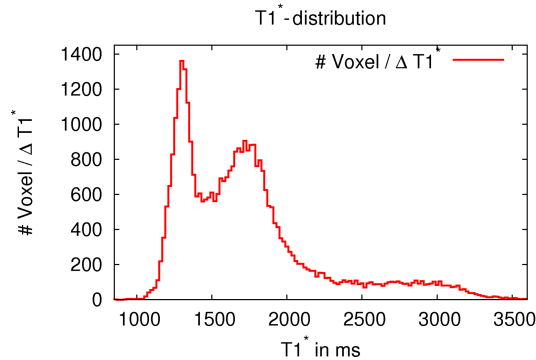


Figure 7.3: Representative distribution of T_1^* of the first subject. It can be seen how WM-voxels (left peak) can be distinguished from GM (right peak) at the used resolution ($1.5 \times 1.5 \times 1.5 mm^3$). It is apparent that there are only very few voxels that contain all three compartments (GM, WM and CSF).

The peaks and the minimum between the peaks of the T_1^* -distribution was derived for each subject individually.

The GM-mask is derived as described in section 5.5.3. A WM-probability mask was derived by including all voxels within the WM-peak (left peak in Fig. 7.3). The

WM-fraction of voxels in the transition zone between WM and GM was derived with a Fermi distribution function $f(T_1^*) = \frac{1}{\exp\left(\frac{2(T_1^* - min)}{GM_{Peak} - WM_{Peak}}\right) + 1}$. The WM-masks were not used in this thesis. A CSF-Mask was created by calculating the fraction of each voxel that is not completely filled with GM and has a T_1^* higher than the GM-peak (right peak in Fig. 7.3). The CSF-fraction was determined as the volume fraction within the voxel that is not filled with GM. A representative T_1^* -map and all masks of the first subject are shown in Fig 7.4

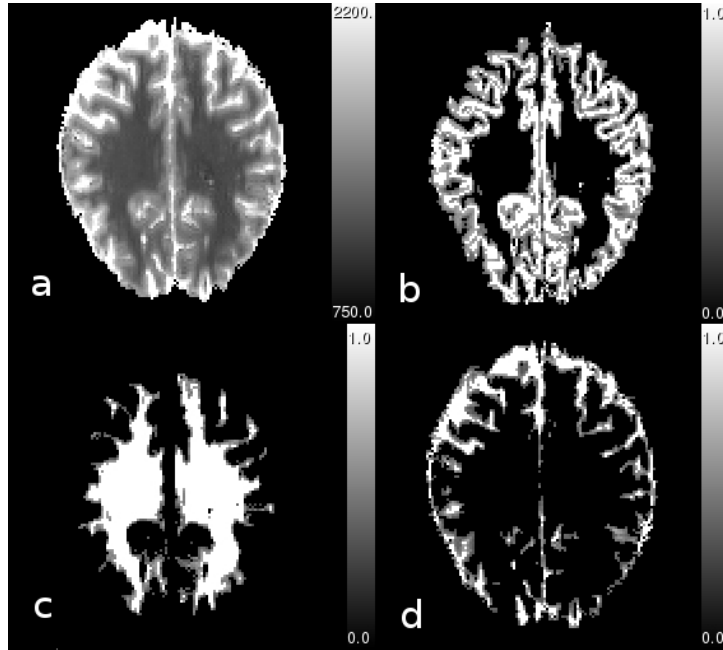


Figure 7.4: Representative T_1^* -map (a) with corresponding GM-mask (b) WM-mask (c) and CSF-mask of the first subject.

- **BOLD-Correction:** The images were combined to correct for the BOLD effect, according to the algorithm described in section 5.3. In order to avoid a time shift of the resulting VASO and BOLD time series, the VASO images (with foregone inversion) were corrected by means of both the previous and the following BOLD images. The surrounding images were used to interpolate the BOLD signal linearly to the time of VASO image acquisition. This evaluation step produced a time series of BOLD-corrected VASO contrast, as well a BOLD contrast for the same measurement with a temporal resolution of $2TR = 3s$.

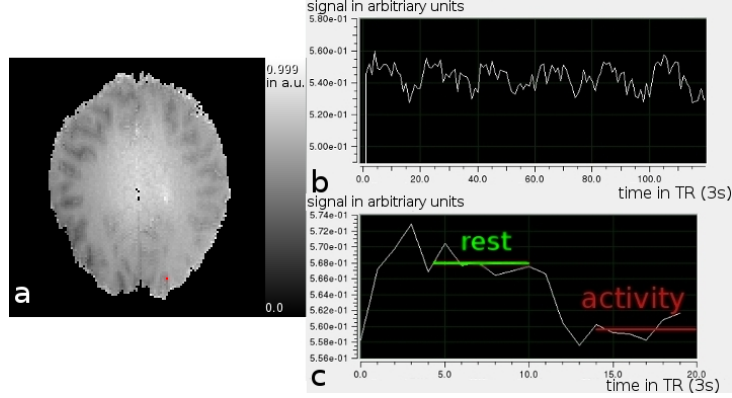


Figure 7.5: (a) Representative BOLD-corrected VASO image of the first subject with corresponding temporal evolution of the signal in (b) and the time course averaged over all stimulation periods in (c), and of a voxel that shows strong CBV-changes.

The evaluation software was written in C++. A representative BOLD-corrected VASO image is presented in Fig. 7.5 with the time course of a voxel that shows strong CBV-changes.

- **Correction for Signal Drifts:** A linear signal drift was calculated by determining the mean signal during the first and the last resting periods of the measurement. The implemented signal drift correction minimized the difference of the signal during the first and the last resting periods for every voxel individually. The signal drift correction was implemented as a small C++ software.
- **Generation of $\frac{\Delta CBV}{CBV_{rest}}$ -Maps:** The temporal signal evolution of every voxel was averaged over all six stimulation periods. Fig. 7.5 (c) depicts such an averaged time course for one voxel. The relative signal change was calculated as the difference of the mean signal during stimulation (red line in Fig. 7.5) with the mean signal during rest (green line in Fig. 7.5). The first 12s of every period were ignored to account for the delayed vascular response to neural activity. The relative change in CBV was determined for every voxel by means of the GM-signal fraction (see section 5.5), CBV_{rest} (see section 5.2.5) and the signal change with formula 7.1.

$$\frac{\Delta CBV}{CBV_{rest}} = \frac{S_{rest} - S_{act}}{S_{rest}} \frac{1}{CBV_{rest}} \frac{1}{GM_{fraction}} \quad (7.1)$$

A $\frac{\Delta CBV}{CBV_{rest}}$ -map was filled with these values. CBV volume fraction in GM at rest was assumed to be $CBV_{rest} = 5.5\%$ (see Tab. 5.2 on page 42). To obtain an activation map, a $\frac{\Delta CBV}{CBV_{rest}}$ -threshold of 5% was introduced. A representative $\frac{\Delta CBV}{CBV_{rest}}$ -activation map of the first subject is depicted in Fig. 7.6 (a). In general, many false positive voxels can be seen outside the grey matter of the occipital lobe. Due to the large

amount of voxels (≈ 50.000) it is not surprising that some voxels show signal increase induced by noise and no change in CBV. These false positive voxels can be filtered out by introducing a cluster threshold. The cluster threshold and the corresponding false positive voxels were determined by means of statistical activation maps described in the following paragraph. The selection of the threshold value is discussed in section 8.12.1. A representative $\frac{\Delta CBV}{CBV_{rest}}$ -activation map of the first subject with the cluster threshold is depicted in Fig. 7.6 (b).

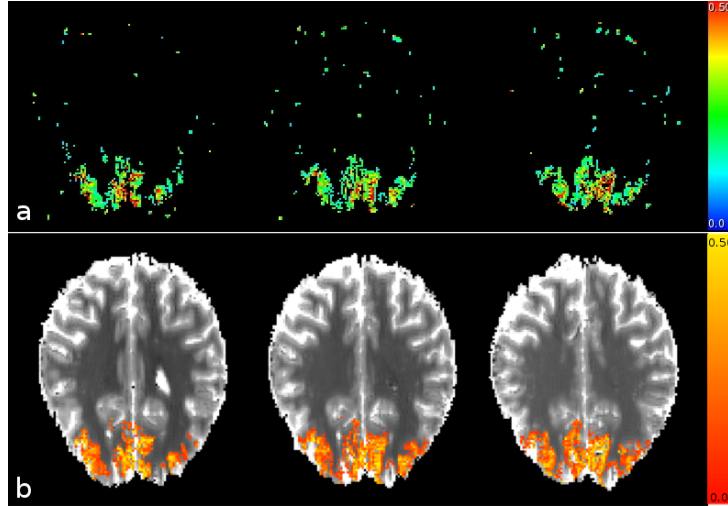


Figure 7.6: (a) Representative $\frac{\Delta CBV}{CBV_{rest}}$ -activation map and (b) the same data using a cluster threshold, superimposed on the T_1^* -map of the first subject.

- Statistical Analysis:** Three Statistical activation maps were created for all subjects. z-score maps were calculated using the software Feat (Version 5.98) [Worsley, 2001]. A high-pass filter cutoff of 100s was used to account for residual signal drifts of higher non-linear order. Activation was defined as a cluster of voxels having z-values above 2.3 (single voxel) and a combined significance level of $p < 0.05$ (cluster, multiple comparison corrected). In statistical hypothesis testing, a z-value indicates how many standard deviations an observation is above or below the mean of a Gaussian probability distribution function. It can be converted into the p-value, which denotes the probability to obtain the observed data assuming the null hypothesis is true. Cluster thresholding is often done in functional fMRI to handle the multiple comparison problem. The three generated activation maps were: (a) an activation map of the VASO data with a spatial smoothing with a smoothing constant of $0.5mm$ (FWHM), (b) an activation map of the VASO data without smoothing and (c) an activation map of the BOLD data without smoothing. The smoothed VASO activation map was used for exclusion of false positive voxel clusters. The unsmoothed VASO and BOLD activation maps were used for comparison of spatial differences of VASO and BOLD. It must be pointed out that the statistical analysis is only done to restrict the region of interest and to exclude false-positive voxels.

The z-values within the activation maps are ignored and only relative signal changes are considered. Because of the $\frac{\Delta CBV}{CBV_{rest}}$ -threshold of 5%, the CBV activation maps are usually considerably smaller than the statistical activation maps derived after smoothing.

- **Application of the Generated Data:** Mean time courses of all significant BOLD and VASO voxels, as well as the corresponding signal changes were calculated for the aforementioned masks.

After processing of the functional data, every voxel was provided with the set of the following parameters:

- VASO signal change
- $\frac{\Delta CBV}{CBV_{rest}}$
- VASO z-value after spatial smoothing with FWHM of $0.5mm$
- VASO z-value without spatial smoothing
- VASO signal evolution and corresponding standard deviation regarding signal variations between the six stimulation periods
- BOLD signal change
- BOLD z-value without spatial smoothing
- BOLD signal evolution and corresponding standard deviation regarding signal variations between the six stimulation periods
- GM signal content
- CSF volume content

8 Results and Discussion

8.1 Relative Change in CBV

As mentioned in section 7.4, $\frac{\Delta CBV}{CBV_{rest}}$ activation maps were created for all ten subjects. The area of activation is fairly restricted to GM of the visual cortex (see Fig. 8.1).

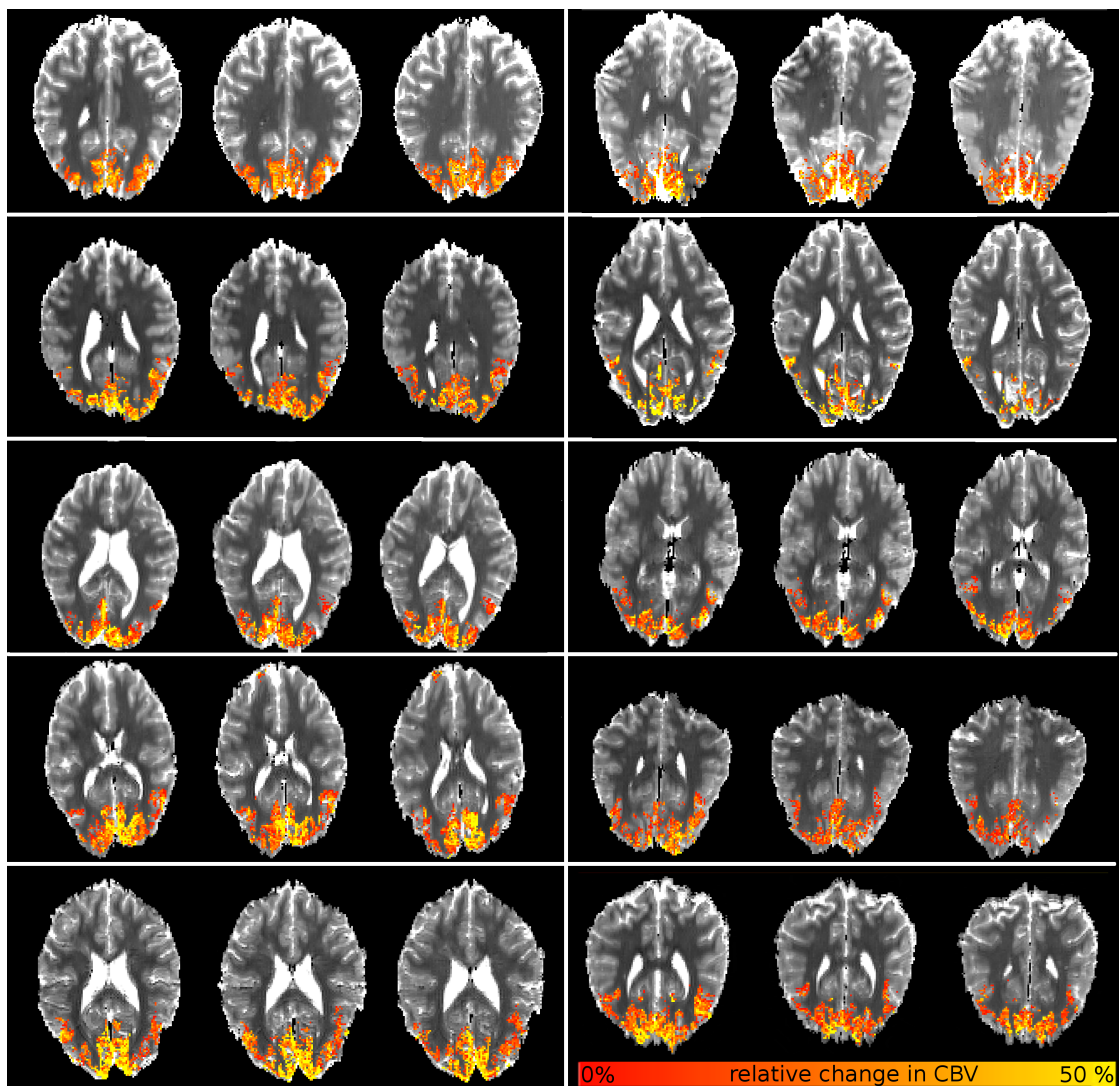


Figure 8.1: CBV $\frac{\Delta CBV}{CBV_{rest}}$ activation maps of all ten subjects.

In some subjects, the acquired slices contain the visual area V5. V5 is a region of extrastriate visual cortex that is thought to play a major role in the perception of motion. Due to the small volume coverage of only three slices with a thickness of 1.5mm , V5 is not covered by the field of view in all subjects. The number of active voxels varies strongly between the subjects (see Fig. 8.1 and Tab. 8.1). Nevertheless, the relative signal change is quite stable. The average change in CBV was calculated to be $\frac{\Delta\text{CBV}}{\text{CBV}_{rest}} = 28.2\% \pm 4.5\%$. Underlying assumptions in this calculation are that (a) there is no change in the volume fraction of CSF between activation and baseline, (b) the entire blood in the microvessels is nulled and (c) CBV volume fraction in GM at rest is $\text{CBV}_{rest} = 5.5\%$ (compare with Tab. 5.2). The individual results of all subject are summarized in Tab. 8.1.

	Subject	Date	Sex	$\frac{\Delta\text{CBV}}{\text{CBV}_{rest}}$	Voxel Number	GM-fraction
1	KMKT	06/08/11	m	30.58%	2518	60.82%
2	HKDT	06/23/11	m	27.90%	1425	60.88%
3	HSJT	06/28/11	w	28.49%	2811	61.11%
4	BAKT	06/29/11	m	20.81%	1760	51.14%
5	GF1T	06/29/11	m	23.59%	1776	64.31%
6	JA3T	06/30/11	m	33.26%	2082	56.66%
7	SJ6T	07/08/11	w	31.73%	2862	54.51%
8	HJ7T	07/11/11	w	22.82%	2273	65.37%
9	BE4T	07/15/11	w	33.86%	3001	55.19%
10	WCAT	07/26/11	w	29.24%	2700	48.95%
all	Average		5/5	28.23%	2320.8	57.89%
all	STD¹			4.49%	542.79	5.49%
women	Average			29.23%	2729.4	57.03%
women	STD			3.72%	247.86	5.68%
men	Average			27.23%	1912.2	58.76%
men	STD			4.53%	367.4	4.52%

Table 8.1: Table of results containing ten subjects with identical scan protocol. The relative change in CBV refers to all voxels that show a relative CBV change over 5% and that are within the statistical activation map, which is derived after a spatial smoothing of $\text{FWHM} = 0.5\text{mm}$. The voxel number refers to the volume of activation. The GM-fraction in the last column refers to the averaged GM content of all active voxels.

The mean GM content in all significant voxels is $\approx 58\%$, which is a surprisingly low number. It must be stressed that the excluded voxel clusters are determined not to be significant after spatial smoothing. The number of average GM content of all significant

¹standard deviation

voxels without smoothing increases to $\approx 65\%$ (see Tab. 8.2).

8.2 Connection of Signal Change in VASO and in BOLD to GM and CSF Content

Subject	Number of Voxels	VASO z-val	BOLD z-val	VASO \wedge BOLD	GM in VASO	GM in BOLD	VASO \wedge CSF	BOLD \wedge CSF
KMKT	451	2.3	6.61	59.42%	66.24%	68.91%	24.39%	24.83%
HKDT	269	2.3	4.73	46.09%	60.36%	51.17%	50.55%	46.46%
HSJT	505	2.3	5.45	63.56%	68.79%	66.70%	36.33%	38.01%
BAKT	395	2.3	4.24	56.45%	53.50%	58.32%	8.86%	20.25%
GF1T	135	2.3	4.50	46.66%	73.30%	74.14%	17.77%	29.62%
JA3T	480	2.3	5.03	71.04%	62.32%	62.59%	38.33%	43.95%
SJ6T	615	2.3	5.13	66.50%	61.40%	62.57%	20.16%	27.31%
HJ7T	341	2.3	7.57	40.01%	72.38%	74.69%	24.92%	39.00%
BE4T	799	2.3	5.39	72.84%	60.17%	60.31%	20.05%	22.15%
WCAT	475	2.3	7.35	58.10%	58.40%	65.41%	21.68%	27.78%
Average	467.73	2.3	5.59	58.92%	64.90%	65.55%	26.56%	31.94%
STD	187.06		1.11	10.83%	7.24%	7.67%	12.08%	8.91%

Table 8.2: Table of results containing ten subjects with identical scan protocol. The numbers refer to active voxels in the single slice that is acquired exactly when blood is expected to be nulled. Here, activation in the VASO data is determined without foregone smoothing. Activation of the BOLD-induced signal change is determined in the same manner as the VASO activation, except that the z-value threshold of the BOLD data is increased until the activation volume is the same in both the VASO and the BOLD data. Hence, the number of voxels in the second column refers to the volume of activation in both VASO and BOLD activation. Columns 3 and 4 contain the corresponding z-thresholds. Columns 5-9 contain the relative intersection between the activation volume and/or the different compartments. A voxel is determined as a CSF-voxel, if the CSF volume fraction is larger than 10%.

Results in Tab. 8.2 show that the volume of activity (number of significant voxels) in VASO and in BOLD intersects only up to $\approx 60\%$. The data show the trend that voxels with strong BOLD response overlay more often ($\approx 20\%$) with CSF than VASO voxels (not significant with $p = 0.128$). The mean grey matter content of the significant voxels is the same in VASO and BOLD, namely $\approx 65\%$.

8.3 Time Courses of VASO and BOLD Signal

The averaged signal evolution of all significant voxels from all subjects is calculated.

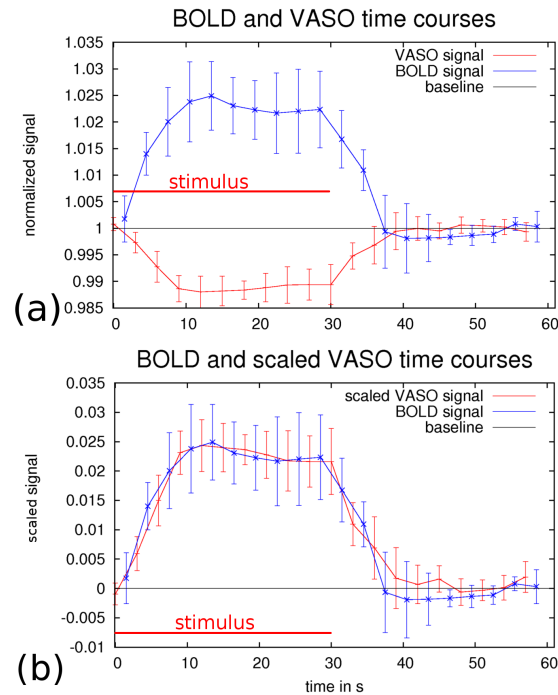


Figure 8.2: BOLD and VASO time courses of all active voxels within the statistical map that is derived after a smoothing of $0.5mm$ (a). The signal intensity is normalized to the signal intensity at rest, i.e. signal is given in units of baseline signal. In (b) the VASO signal time course is scaled (with a negative scale factor) for the sake of comparison. The subjects are exposed to the stimulus during seconds 0 to 30. Error bars refer to the standard deviation between the subjects.

The time courses in Fig. 8.2 show that VASO-induced signal change rises in the same time scale as the BOLD signal. The recurrence to baseline of the VASO signal after the 30s stimulus is in the same range as the BOLD signal. The relatively fast return to baseline of the VASO signal after the stimulus cessation is contrary to the results of [Mandeville et al., 1999] [Herman et al., 2009] but in agreement with [Dechent et al., 2010]. The time evolution after stimulus cessation is discussed in detail in section 8.7.

The error bars in Fig. 8.2 refer to the inter-subject standard deviation. Fig. 8.2 shows that the inter-subject standard deviation of the VASO time course is significantly smaller than the inter-subject standard deviation of the BOLD signal. This is consistent with similar measurements in the literature. Investigating the reproducibility of functional activation measured with BOLD and ASL (CBF) Tjandra et al. [Tjandra et al., 2005]

found that CBF has a significantly lower inter-subject variation than BOLD. Leontiev et al. could not confirm these results [Leontiev and Buxton, 2007], probably due to tSNR limitations in ASL. However, Fig. 8.2 suggests that VASO has better inter-subject reproducibility than BOLD. This could be a consequence of multiple physiological factors (e.g. CBF, CBV, CMRO₂) contributing to BOLD changes, including biological causes such as hormonal changes, arterial concentration of CO₂ and hematocrit. The reduced variability of the BOLD-corrected VASO is very likely also due to inherent division of VASO images with BOLD images during the BOLD-correction evaluation scheme. In other words, small signal drifts due to scanner instability result in an unstable baseline in BOLD, while these instabilities are canceled out in VASO. The VASO and BOLD time courses in Fig. 8.2 are much smoother than the error bars suggest. In other words, if one looks at the surrounding signal values, there is no extraordinary data point in the entire set of signals throughout the time course. This suggests that the standard deviation is dominated by the variation of hemodynamic response of the individual subjects rather than by low tSNR of the acquired data. The variation in hemodynamic response might be due to differences in attention or differences in physiologic (hematocrit variations, T_1 variations) or pharmacologic (e.g. coffee) states.

8.4 BOLD Correction

The BOLD contamination in VASO images is corrected by means of the previous and following BOLD images. In other words, the BOLD signal at the time of VASO image acquisition is assessed by taking the average of the BOLD signal taken 1.5s earlier and the BOLD signal taken 1.5s later. This approach is only valid if the hemodynamic response function doesn't change much during this time period. The error in BOLD correction scheme during fast BOLD signal change is discussed.

Fig. 8.3 depicts the expected hemodynamic response function and the corresponding error in BOLD-corrected VASO images. Fig. 8.3 shows that the error in BOLD correction scheme is negligible in steady-state activation or steady-state rest. When the BOLD hemodynamic response function is concave upwards, VASO signal is underestimated and vice versa. This suggests that the speed of recurrence to baseline in the VASO time courses (Fig. 8.2) might be even faster. It further suggests, that calculation of $\frac{\Delta CBV}{CBV_{rest}}$ is unaffected by the error in BOLD correction scheme, as this calculation is based on the signal change between steady-state rest and steady-state activation (see section 7.4).

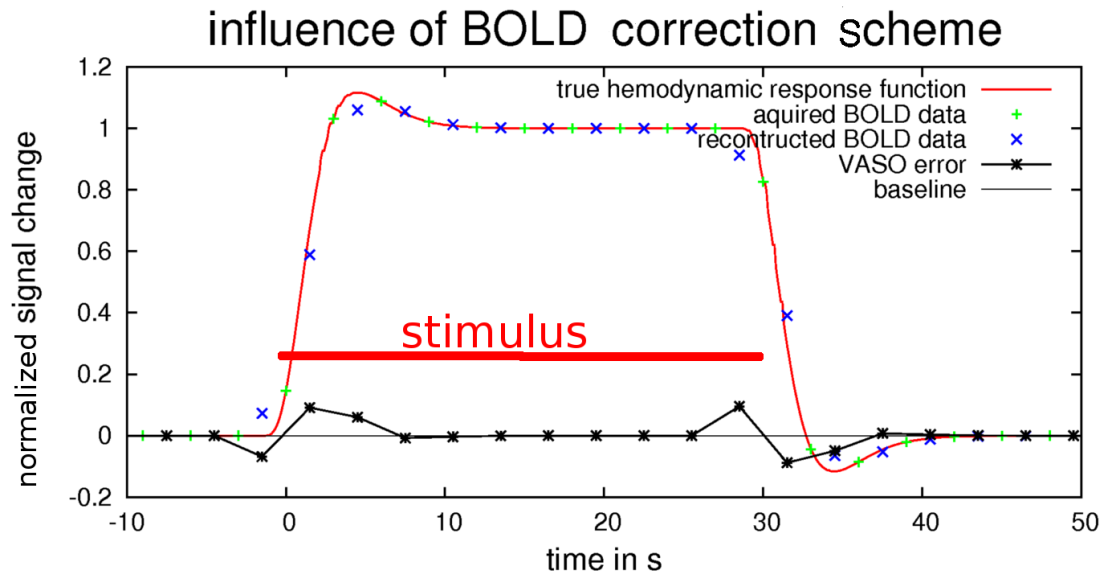


Figure 8.3: Error in BOLD correction scheme due to temporal shift between BOLD and VASO. A double Gamma function is used as hemodynamic response function to include the BOLD post stimulus undershoot. The sampling rate is set to 1.5s like the TR used in this study. The ordinate depicts the signal change normalized to one.

8.5 TR-Dependencies

If the blood remains within a slice longer than $TR = 1.5s$ with thickness of $1.5mm$, not all blood would be nulled. Particularly, the venous blood could have been inverted twice. In this case, the time courses shown in Fig. 8.2 may only represent arterial and capillary blood. These compartments are believed to have different hemodynamic evolution than the venous compartment [Hillman et al., 2007]. Due to substantial CBF increase during neural activity, the not-nulled blood within the venous vessels would be less during activity than during rest. This would lead to an overestimation of $\frac{\Delta CBV}{CBV_{rest}}$. To investigate this issue, the time course of VASO signal is considered during a series of different repetition times of $TR = 1.5s$, $TR = 2s$, $TR = 2.5s$ and $TR = 3s$ in two subjects. The time courses refer to the same set of voxels (region of interest) for all four measurements.

Fig. 8.4 shows no significant variation of the signal change for different repetition times. Neither a dependency in the amount of the relative signal change, nor a structural difference in the shape of the time courses can be seen. This data suggest that total venous blood within the imaging slice is nulled for the scan parameters used in this study.

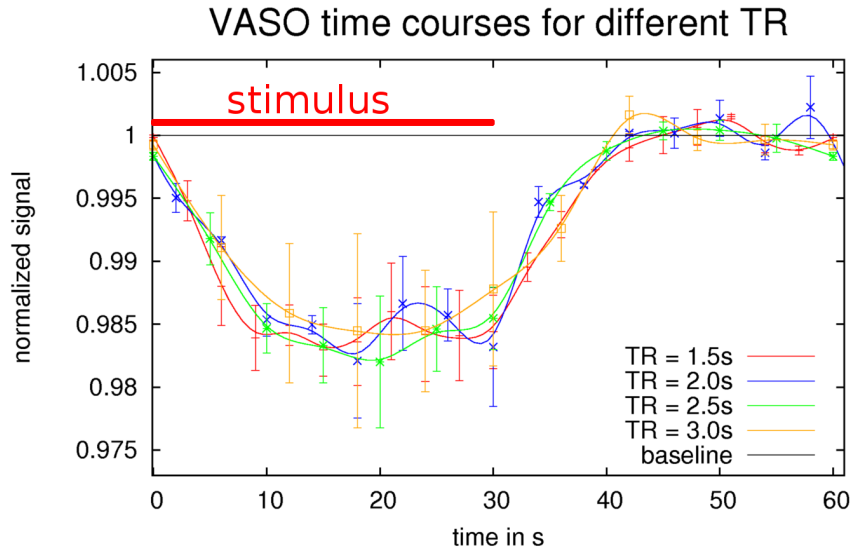


Figure 8.4: VASO time courses of different repetition times of $TR = 1.5s$, $TR = 2s$, $TR = 2.5s$ and $TR = 3s$. Two subjects were measured. The depicted signal time course is the mean of the two subjects. Error bars refer to the standard deviation of the two subjects. The signal is normalized to the signal intensity at rest.

8.6 Influence of Slab Thickness

The basic assumption in slab-selective VASO is that all blood in the microvessels of the imaging slice has been inverted once and only once. For VASO at 7 T the blood nulling time TI is quite large due to large blood T_1 . Hence, there is the possibility that fresh (not-inverted) blood enters the small vessels within that time. Due to CBF increase during activation, more fresh blood would enter the vessels and cause a signal increase during activation. This is essentially the mechanism used in ASL. This CBF-induced signal increase counteracts the VASO signal and results in an underestimation of $\frac{\Delta CBV}{CBV_{rest}}$. To evaluate whether all blood in the microvessels of the imaging slice is nulled, the VASO signal change is considered for five different inversion slab thicknesses. It is expected that for very thin inversion slab thicknesses the VASO signal change is reduced due to the mentioned ASL contamination. However, above a certain inversion slab thickness all blood in the imaging slab should be nulled, associated with no further change in VASO signal. Fig. 8.5 depicts the VASO signal changes of two subjects for five different inversion slab thicknesses. The chronological order of the five scans is set arbitrary to minimize signal changing effects caused by decreasing attention of the subject during the session. Data in Fig. 8.5 suggest that all blood in the microvessels of the imaging slice is nulled for inversion slab thickness above $7cm$. This is just the inversion slab thickness used in this study.

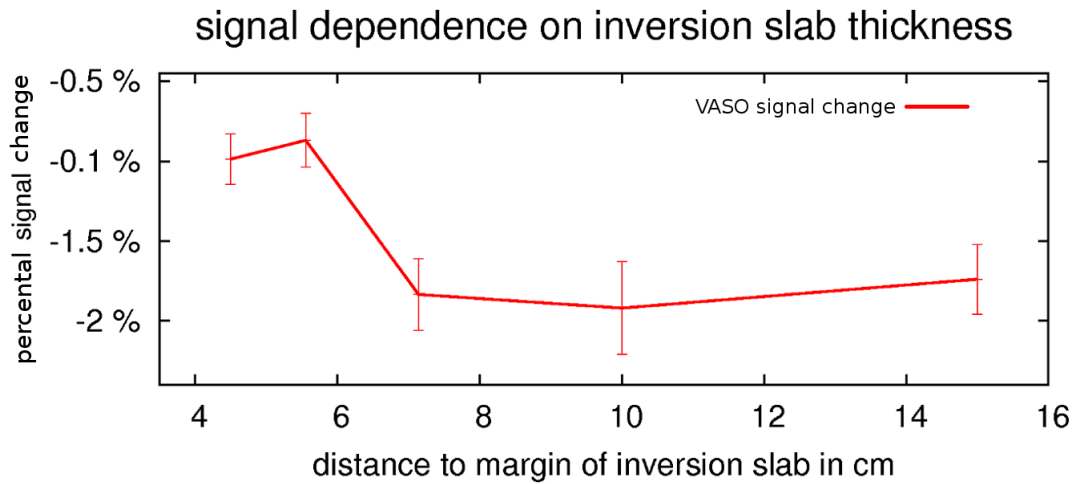


Figure 8.5: Dependence of VASO signal change on inversion slab thickness.

It is important to note that these considerations hold only for functional mapping of $\frac{\Delta CBV}{CBV_{rest}}$ in the occipital lobe. For example, in the motor cortex, the arterial arrival times are in the order of $\approx 500ms$ smaller. There, a thicker inversion slab would have to be used. This data show a clear significant overshoot in the VASO signal (red line in Fig. 8.6). This would imply a post stimulus undershoot in CBV.

8.7 Post Stimulus Undershoot

To investigate the behavior of the vasculature after activity, the resting period was increased to 60s in four subjects.

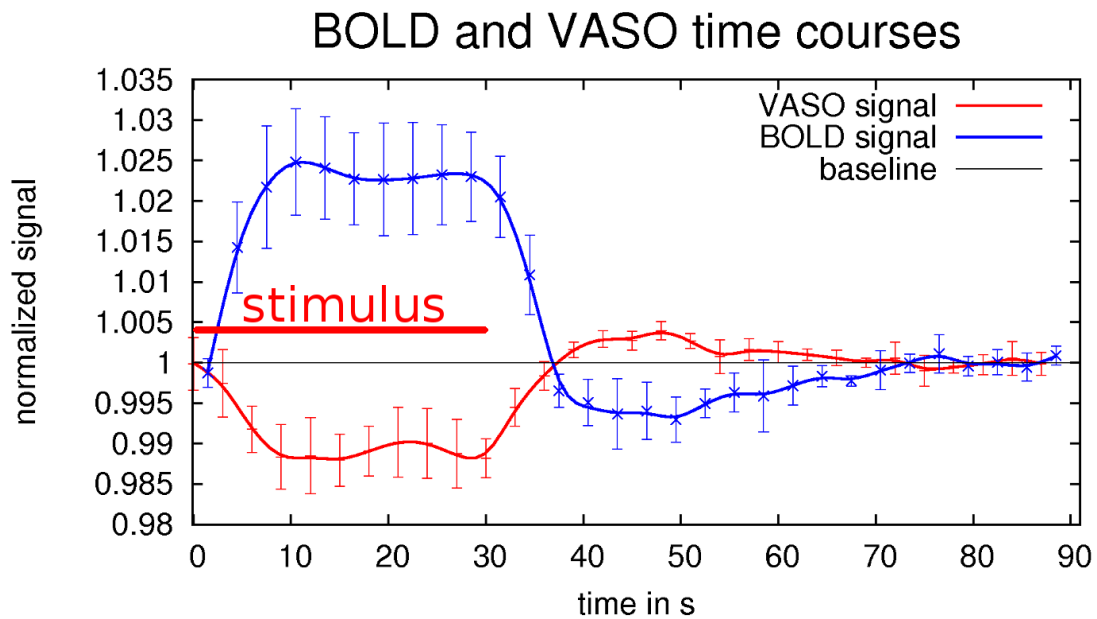


Figure 8.6: BOLD and VASO signal time courses with a stimulation task that contains 30s stimulation periods and 60s resting periods. The time courses depict the average of four subjects. Error bars refer to the standard deviation between the subjects. The signal is normalized to the signal intensity at rest.

There is a controversial debate about the behavior of CBV after stimulus cessation in the literature. Significant post stimulus undershoots in CBV are reported in several publications, while other studies show a prolonged elevated CBV after stimulation.

The following studies report CBV undershoots after stimulation:

- [Donahue et al., 2009a]: Donahue et al. report of a small but significant post stimulus undershoot in CBV using a VASO-FLAIR sequence and a visual stimulation of 30s.
- [Kim and Kim, 2010]: Kim and Kim report of a significant post stimulus undershoot in total CBV using a stimulus (visual) length of 40s. They measure total CBV in anesthetized cats with MION contrast agent. They report an even larger post stimulus undershoot in the arterial compartment of CBV.
- [Poser and Norris, 2007]: VASO HASTE data of Norris and Poser show a significant post stimulus undershoot in visual cortex after a stimulus of 21s.
- [Hillman et al., 2007]: Hillman et al. report a post stimulus undershoot in volume of total arterial hemoglobin in rats after a visual stimulus of 4s using two-photon microscopy.
- [Hua et al., 2011a]: Data from Hua et al. acquired with MT-VASO at 7T show a moderate post stimulus undershoot in CBV.

- [Wu et al., 2007]: Wu et al. report of a significant post stimulus undershoot in CBV using a VASO variant and a stimulus (visual) length of 24s.

The following studies show a prolonged elevated CBV after stimulation:

- [Herman et al., 2009]. Herman et al. show a prolonged elevated CBV after electrical stimulation of 30s in anesthetized rats using laser-Doppler flowmetry.
- [Mandeville et al., 1999]. Mandeville et al. show a prolonged CBV after electrical stimulation of rat forepaw of 120s using contrast agent MRI.

Venous CBV is believed to show a delayed recurrence to baseline throughout the literature [Chen and Pike, 2010a] [Buxton, 2010] [Kim and Kim, 2010] [Mandeville et al., 1999]. It must be pointed out that the results in this study are not at variance with Mandeville’s established Windkessel model [Mandeville et al., 1999] or Buxton’s Balloon model [Buxton et al., 1998]. These models explain the post stimulus undershoot of BOLD with a prolonged elevated volume of deoxygenated blood after the stimulus. As VASO measures the total CBV change and BOLD depends only on the venous (deoxygenated) CBV, the results of this study do not contradict with the Balloon or Windkessel model. I hypothesize a substantial post stimulus undershoot in arteriolar CBV, a mild undershoot in total CBV and a prolonged elevated venous CBV.

Because the post stimulus undershoot in CBV is by no means well established, it is discussed in detail below. Errors in the signal time course of the slab-selective VASO sequence can have by the following possible sources:

- **Time Blood Spends within the Imaging Slice:** The slab-selective VASO sequence can be biased to arteriolar CBV changes if the repetition time TR is shorter than the dwell time blood spends in the imaging slice (see section 8.5). As the VASO signal change does not vary for different TR, this explanation for the post stimulus in CBV can be excluded.
- **Bias Caused by BOLD Correction Scheme:** The evaluation software of the BOLD correction scheme can only account for the total BOLD effect as long as the second time derivative of the BOLD time course is very small (see section 8.4). After cessation of the stimulus, BOLD time course is concave upwards, which corresponds to a CBV underestimation. Hence, BOLD correction scheme can not explain the post stimulus undershoot of CBV, but rather suggests that the undershoot might even be slightly larger.
- **Dependence on Stimulus Duration:** For short stimulus durations, the CBV of the venous compartment shows almost no change at all [Hillman et al., 2007] [Lee et al., 2001] [Kim and Kim, 2010]. Only for stimulation periods longer than 30s – 40s, a stronger change in venous CBV can be seen. Hence, the omission of the venous CBV change (with slower behavior) after a short stimulus could explain the post stimulus in the data. Since the undershoot persists for longer stimulus durations (see section 8.8), this effect can not entirely explain the post stimulus undershoot in CBV either.

- **ASL-Contamination:** The slab-selective VASO approach assumes that no fresh (not-inverted) blood enters the small vessels within the inversion time. If not-inverted blood enters the small vessels of the imaging slice, the blood in the arteries would be not nulled. Due to the substantial increase in arterial CBF during activation, the amount of inflowing fresh blood in the microvasculature would increase during activation. Based on steady-state considerations, a similar ASL contamination of VASO was first investigated in [Donahue et al., 2006] and further discussed in [Donahue et al., 2009b]. Due to this effect, the signal of the slab-selective VASO would increase during activation, which causes an additional underestimation of arterial CBV. In this case, an undershoot in CBF would counteract the VASO signal overshoot. This suggests that the mentioned ASL contamination can not explain the measured VASO signal overshoot. Furthermore, the results in section 8.6 show that the ASL contamination can be neglected with the used inversion slab thickness.
- **Water Exchange in Capillaries:** Due to relatively long inversion times used, water exchange between intravascular space and tissue can result in incomplete blood nulling in the venous compartment. The residual venous blood contribution could introduce a mild CBF weighting associated with a post stimulus overshoot in VASO signal. The effect of CBF due to blood-brain barrier permeability on VASO is discussed in more detail in section 8.16.

8.8 Stimulus Length

To investigate whether the VASO overshoot is caused only by omission of slowly changing venous CBV with short stimulus durations, the stimulus duration was increased to 60 s in two subjects. Fig. 8.7 compares VASO time courses for the stimulus paradigm 1 of 30s activity and 90s rest with the paradigm 2 of 60s activity and 60s rest. The post stimulus overshoot of VASO is clearly apparent with both stimulus durations. The overshoot tends to be a little smaller in paradigm 2 than in paradigm 1 (not significant). However, the overshoot seems to be almost as big as the original signal decrease during stimulus. This is in contrast to the time courses in Fig. 8.6. It must be pointed out that here one stimulus-rest period lasts two minutes, which is already in the time scale of signal drifts due to scanner instabilities. This results show that the post stimulus overshoot in VASO can not be explained by the omission of the venous CBV change after a short stimulus.

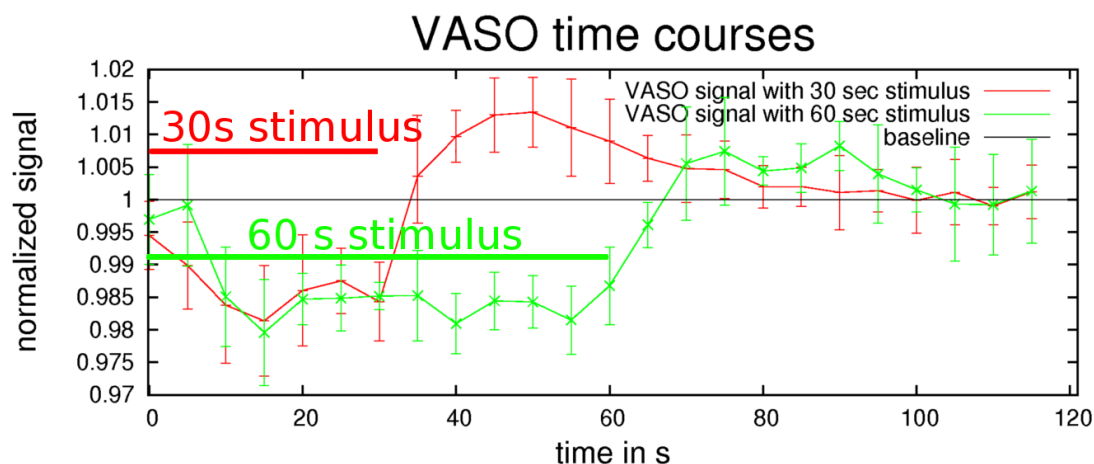


Figure 8.7: VASO signal time courses with stimulation paradigm 1 that consists of 30s stimulation and 90s rest, and VASO signal time courses with stimulation paradigm 2 that contains 60s stimulation and 60s rest. The depicted time courses are the average of two subjects. Error bars refer to the standard deviation between the two subjects. The signal is normalized to the signal intensity at rest. The baseline is set to the signal intensity at the end of the resting period.

8.9 Spatial Specificity of BOLD and VASO

For the sake of accurate comparison of the spatial differences between VASO and BOLD, the time courses of active voxels without smoothing are considered. The following considerations refer only to the middle slice where blood is believed to be completely nulled. In this slice the signal change is directly proportional to ΔCBV . Fig. 8.8 (a) depicts the signal time course of these voxels. Fig. 8.8 (b) depicts the signal time course of a subset of these voxels that are filled with at least 10% of CSF volume and more than 5% GM volume. The voxels that contain more than 10% CSF are believed to represent the surface of the cortex and more likely contain GE BOLD-sensitive draining veins. A comparison of Fig. 8.8 (b) with Fig. 8.2 (a) clearly shows that the signal change of all active voxels without foregone smoothing is larger. This is not surprising, since the voxels with small signal change also have a lower significance z-values.

The voxels that contain more than 10% of CSF volume shows a significant ($p = 0.026$) increase in BOLD signal change from $\approx 4.6\%$ to $\approx 5.4\%$ (Fig. 8.8 (b)). This corresponds to a relative increase of $\approx 18\%$. In VASO, a significant ($p = 0.0018$) decrease of the signal change from $\approx 2.1\%$ to $\approx 1.4\%$ can be seen. That corresponds to a relative decrease of $\approx 30\%$. The temporal evolution of the time course (e.g. recurrence to baseline) seems to remain the same.

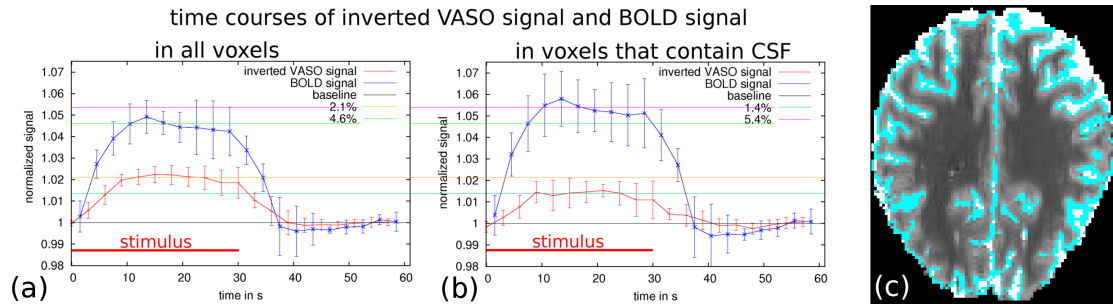


Figure 8.8: BOLD and VASO time courses of all significant voxels within the statistical map derived without smoothing are depicted in (a). Time courses of the subset of voxels that contain $> 10\%$ CSF volume fraction and $> 5\%$ GM volume fraction are depicted in (b). The time courses contain data of all ten subjects. The error bars refer to the standard deviation between the subjects. The signal is normalized to the signal intensity at rest. The surface voxels in the transition region between GM a CSF are depicted for the first subject in (c).

This signal difference suggests that CBV change occurs in the deeper layers of the cortex. This is in agreement with [Kim and Kim, 2010], where Kim and Kim show that in V1 of cats the highest change in CBV is located in layer IV. Weber et al. [Weber et al., 2008] report that this is also the layer with the highest CBV fraction at rest (in macaques). In contrast to VASO, the BOLD signal change is largest in the upper layers of the cortex. This is in agreement with results from depth-dependent BOLD measurements in humans V1 [Koopmans et al., 2010]. It is believed to be caused by BOLD-sensitive pial veins on the cortical surface [Turner, 2002].

8.10 CSF

In the slab-selective VASO approach CSF z-magnetization within the imaging slice is in steady-state, while blood in the imaging slice has been inverted only once. This circumstance can be utilized to null both blood and CSF (see section 5.4.4). Fig. 8.9 shows that there is no significant difference in BOLD for different TR. There is a minor difference expected between intravascular and extravascular signal. This contrast difference is highly suppressed at high fields, as there is almost no contribution of intravascular BOLD effect in GE images due to short T_2^* of venous blood [Kim and Bandettini, 2010]. Fig. 8.9 shows a difference in VASO signal time course for nulled and not-nulled CSF. For the CSF-nulled approach, the VASO signal change is significantly ($p = 0.0094$) larger.

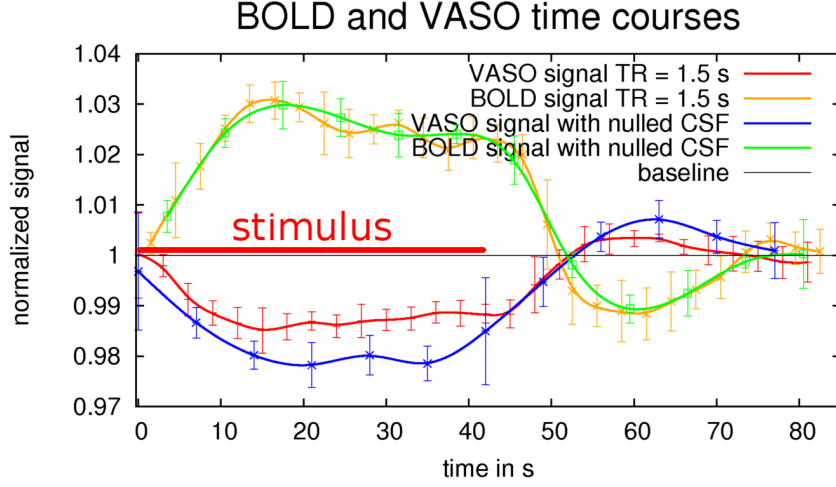


Figure 8.9: BOLD and VASO time courses with not-nulled CSF ($TR = 1.5s$) and nulled CSF ($TR = 3.5s$). The experiment is done with two subjects. Signal time courses refer to mean of the two subjects. The error bars refer to the standard deviation between the subjects. The signal is normalized to the signal intensity at rest.

To discuss this difference, the origin of signal change is considered. The relative signal change can be modeled with Eq. 8.1 for the case of CSF not-nulled and it can be modeled with Eq. 8.2 for nulled CSF.

$$\frac{\Delta S}{S_{rest}} = \frac{S_{GM}\Delta V_{GM} + S_{CSF}\Delta V_{CSF}}{S_{GM} + S_{CSF}} \quad \text{for not-nulled CSF} \quad (8.1)$$

$$\frac{\Delta S}{S_{rest}} = \frac{S_{GM}\Delta V_{GM}}{S_{GM}} \quad \text{for nulled CSF} \quad (8.2)$$

Here S_{GM} and S_{CSF} denote the relative signal per unit volume of GM and CSF. This value is dependent on z-magnetization, the proton density, T_2^* and relative volume in a voxel of the corresponding compartment. V_{CSF} and V_{GM} denote the activation-induced volume change in CSF and GM. If we assume that $\frac{\Delta CBV}{CBV_{rest}}$ is compensated more with change in GM volume than change in CSF Volume, VASO signal change is expected to be larger in the CSF nulled approach.

$$\frac{\overbrace{S_{GM}\Delta V_{GM} + S_{CSF}\Delta V_{CSF}}^{\text{Eq. 8.1}}}{S_{GM} + S_{CSF}} < \frac{\overbrace{S_{GM}\Delta V_{GM}}^{\text{Eq. 8.2}}}{S_{GM}} \quad \text{for } \Delta V_{GM} > \Delta V_{CSF} \Leftrightarrow \quad (8.3)$$

$$\frac{S_{GM} + S_{CSF}}{S_{GM} + S_{CSF}} \frac{\Delta V_{CSF}}{\Delta V_{GM}} < 1 \quad \text{for } \frac{\Delta V_{CSF}}{\Delta V_{GM}} < 1$$

These considerations explain that the VASO signal change is larger for nulled CSF than for not-nulled CSF.

In conclusion, the data suggest that not all CBV change is compensated by GM, but also by CSF to some extent. This is in agreement with previous VASO studies of Scouten and Constable [Scouten and Constable, 2008]. In this study the dynamic CSF behavior is assessed by comparing a VASO experiment with nulled blood and an experiment with nulled CSF. They show that changes in CSF fraction with activation can have a significant impact on conventional blood-nulled VASO signal. In [Donahue et al., 2006] Donahue et al. estimate the CSF partial volume at rest with a double inversion (VASO-FLAIR) and they find an upper bound of CSF volume change of $\approx 10\%$. Piechnik et al. found functional change in CSF volume using measurement of water T_2 relaxation of $5\% - 6\%$ with visual stimulation [Piechnik et al., 2009]. However, it is not clear where the CSF volume goes, since the cranium is regarded to be a closed container (see more in section 5.4.4).

8.11 Signal Change Distribution

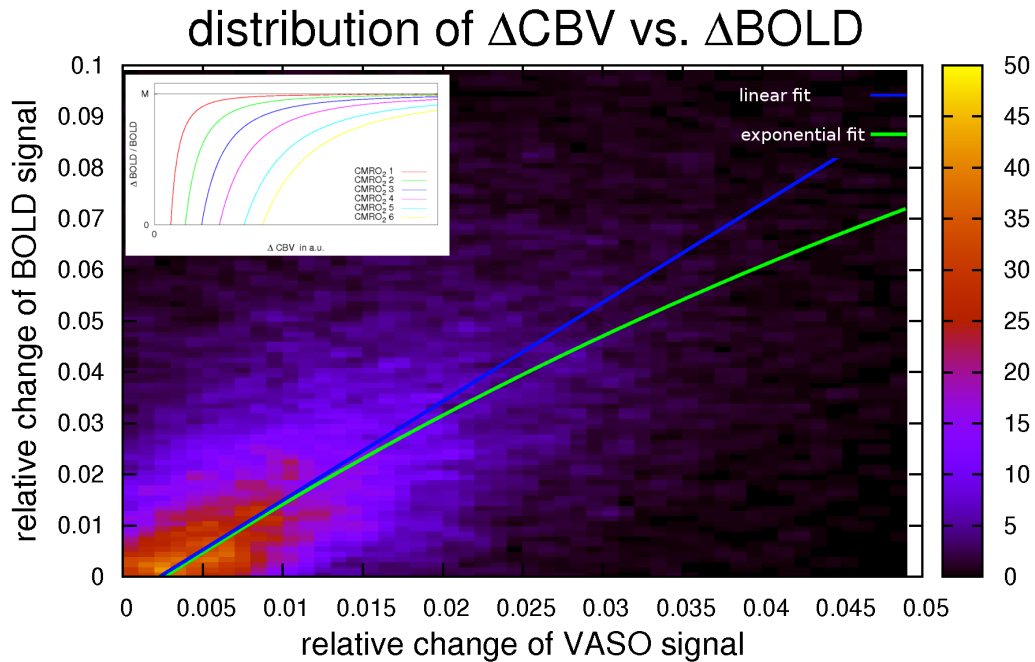


Figure 8.10: Distribution of VASO and BOLD signal changes and their correlation. The theoretical relationship of $\Delta BOLD$ to ΔCBV according to the deoxyhemoglobin dilution model [Hoge et al., 1999] is displayed for different values of $CMRO_2$. The histogram contains all significant voxels determined without smoothing and within the middle slice. The signal changes are displayed in units of the signal intensity at rest.

The wide scattering of signal changes in Fig. 8.10 show a relatively low correlation between BOLD and VASO signal change. The relation between BOLD and VASO signal change seems to be slightly non-linear. Furthermore, the distribution seems to be biased to large signal changes in VASO (see transition through abscissa in Fig. 8.10). These features are discussed in the following.

BOLD contrast $\frac{\Delta BOLD}{BOLD}$ depends on the interplay of CBF, CBV and CMRO₂. The connection can be described with the deoxyhemoglobin dilution model [Hoge et al., 1999]:

$$\frac{\Delta BOLD}{BOLD} = M \left[1 - \left(\frac{CMRO_2}{CMRO_{2\ rest}} \right)^\beta \left(\frac{CBV}{CBV_{rest}} \right) \left(\frac{CBF_{rest}}{CBF} \right)^\beta \right] \quad (8.4)$$

Here, M is a calibration factor that may be dependent between subjects and brain areas. It represents the maximum BOLD signal change that can be attained by achieving a theoretical 100% oxygen saturation in the venous vessels. β describes the oxygenation and field strength dependence of the BOLD effect. The last term in Eq. 8.4 can be expressed as a function of CBV according to the Grubb relation $\frac{CBV}{CBV_{rest}} = \left(\frac{CBF_{rest}}{CBF} \right)^\alpha$ (see equation 3.5).

$$\frac{\Delta BOLD}{BOLD} = M \left[1 - \left(\frac{CMRO_2}{CMRO_{2\ rest}} \right)^\beta \left(\frac{CBV}{CBV_{rest}} \right)^{1-\frac{\beta}{\alpha}} \right] \quad (8.5)$$

This curve is depicted for different values of CMRO₂ in the upper left section in Fig. 8.10. The measured relation between BOLD and VASO is still in the linear range with the stimulus used. A larger and nonlinear BOLD and CBV change is expected for flickering checkerboard stimulation or hypercapnia-induced change in BOLD and CBV.

The large scattering of VASO and BOLD signal can be caused by factors other than noise. (a) The M -value varies immensely between subjects, which is directly reflected in the slope of the curve in Fig. 8.10. (b) Since the resolution used has the same scale as cortical thickness, the different compartments of the deoxyhemoglobin dilution model are not necessarily in the same voxel. For example, the draining veins at the cortical surface are believed to show large BOLD effect but almost no change in CBV. This could result a loose connection between VASO and BOLD.

The individual signal distribution of BOLD and VASO is considered in the following.

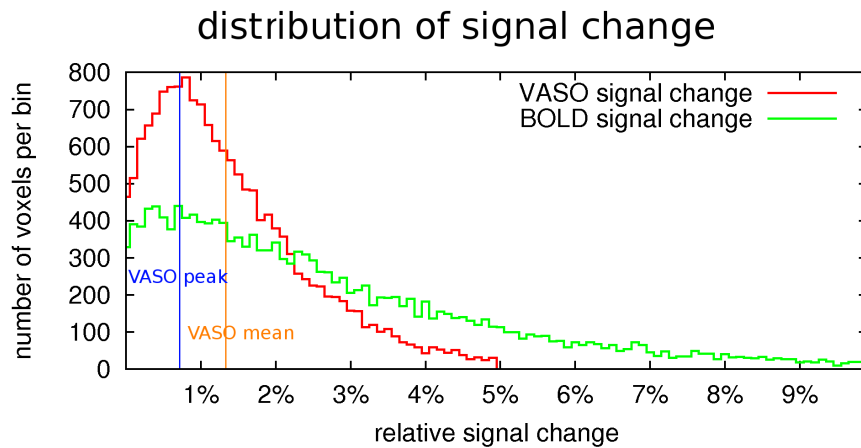


Figure 8.11: Distribution of VASO and BOLD signal changes. A cutoff value is used in VASO to exclude voxels with Signal changes that are much more than the expected values. Therefore no VASO signal change is depicted above 5%. For a voxel of pure GM this would correspond to a relative change in CBV of $\approx 91\%$.

Fig. 8.11 shows that there is a distinct peak in the VASO signal change distribution. In the BOLD signal change distribution, the peak is not so clear. This is also reflected in the fact that the distribution in Fig. 8.10 does not cross the origin, but crosses the abscissa at a positive value of VASO signal change.

There are two possible explanations for this:

- In voxels that have only small BOLD response, the vasculature increases its volume at least to a minimum value. In other words, there is almost no BOLD response despite increase in neural activity if the CBF increase is compensated by $CMRO_2$ increase. This can be illustrated by a curve in the deoxyhemoglobin dilution model with a high value of $CMRO_2$. CBV on the other hand is independent of $CMRO_2$ response.
- Because of the different spatial specificity of BOLD and VASO, there are some significant BOLD voxels in areas that show lower noise level. Hence, it is more likely for BOLD to have high z-values in voxels that show only small signal changes. Fig. 8.12 shows an example with some significant BOLD clusters within the WM where actually no strong activation is expected. In WM the noise level is lower than in GM [Bodurka et al., 2007]. Therefore, these voxels get relatively high z-values despite their small signal change.

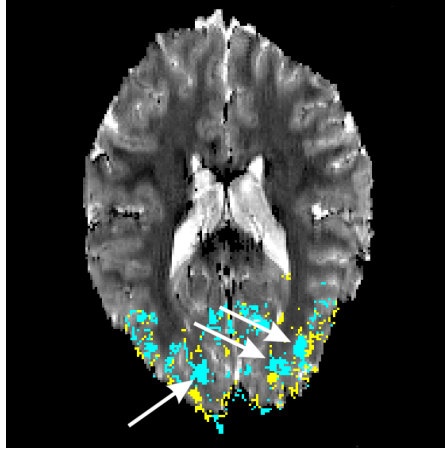


Figure 8.12: Spatial difference of VASO and BOLD. To generate this image, the z-value of BOLD is scaled up so that BOLD and VASO have the same number of significant voxels. All voxels that show significant z-values in VASO but no significant z-value in BOLD are colored in yellow. All voxels that show significant z-values in BOLD but no significant z-value in VASO are colored in turquoise. The arrows emphasize BOLD clusters in WM, where even a small signal change could lead to high z-values due to the low noise level. A reasonable hypothesis could be that despite the large z-threshold in BOLD, there are some false positive clusters.

8.12 Noise-Induced Bias in $\frac{\Delta CBV}{CBV_{rest}}$ Determination

Voxels that show only small stimulus-induced VASO signal change may have only small z-values in the statistical activation maps, and may not exceed the z-value threshold. Hence, they may not contribute to the calculation of the mean $\frac{\Delta CBV}{CBV_{rest}}$. Voxels that show high stimulus-induced signal change are less likely to be excluded from the activation maps. This disparity could lead to an overestimation of $\frac{\Delta CBV}{CBV_{rest}}$. To investigate whether all voxels that contain stimulus-induced signal change are included in the activity map, the distribution of the signal change is considered. Fig. 8.13 depicts the spectra of the signal change during a visual stimulation task and the background noise-induced signal distribution. As expected, more voxels show a positive signal change during a visual task. The difference of the two signal distribution functions in Fig. 8.13 is expected to contain only the distribution of the stimulus-induced signal change. The mean of this distribution $\frac{\int_0^\infty x f(x) dx}{\int_0^\infty f(x) dx}$ provides the mean value of $\frac{\Delta CBV}{CBV_{rest}}$ independent of the statistical activation maps. However, the spatial information for the voxels is lost. Fig. 8.14 compares the aforementioned distribution of signal change with the signal change of all significant voxels within the activation maps.

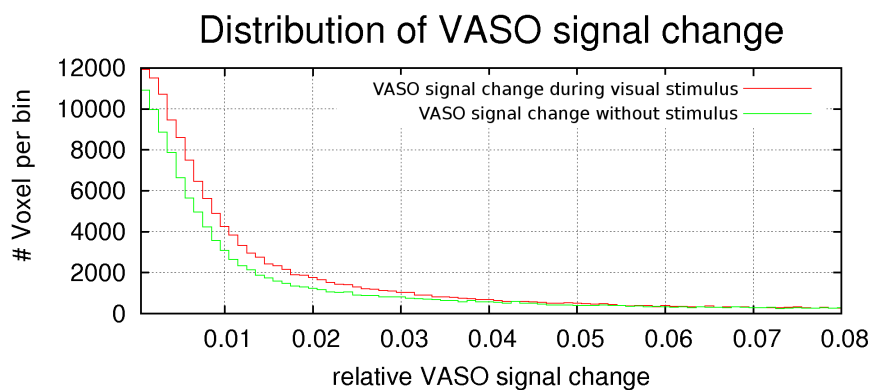


Figure 8.13: Distribution of the signal change with and without visual stimulation. The data of all ten subjects are included in the spectra.

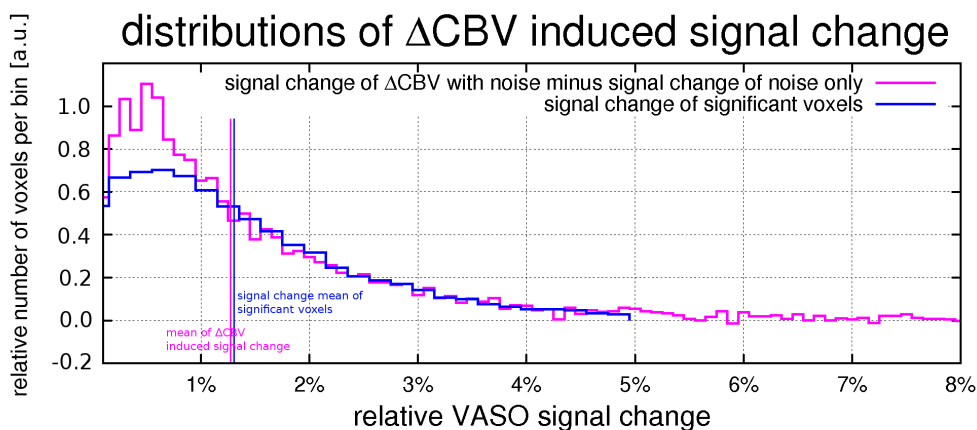


Figure 8.14: Distribution of stimulus-induced VASO signal change and distribution of signal change of significant voxels. The mean of stimulus-induced signal change is

$$\frac{\int_0^{\infty} x f(x) dx}{\int_0^{\infty} f(x) dx} = 0.012711$$

$$\text{and the mean of the signal distribution of all significant voxels is } \frac{\int_0^{\infty} x f(x) dx}{\int_0^{\infty} f(x) dx} = 0.01304.$$

Fig. 8.14 shows that the activation maps underestimate the number of significant voxels at signal changes below 1%. This leads to a small overestimation of $\frac{\Delta CBV}{CBV_{rest}}$ in the range of $\approx 2.59\%$. Hence the relative change in CBV is not $28.23\% \pm 4.49\%$ but rather $27.49\% \pm 4.55\%$.

8.12.1 Cluster Threshold

Activation is defined as a cluster of voxels having z-values above 2.3 and a combined significance of $p < 0.05$. This is done to avoid false positive voxels caused by the multiple comparison problem in noisy data. This threshold is varied in pilot scans to exclude all significant clusters beyond the occipital lobe. In nine of ten subjects the clusters in the occipital lobe contain much more than 100 voxels and voxels beyond the occipital lobe contain less than 40 voxels. In subject SJ6T only (fourth in the first column in Fig. 8.1), there is a significant cluster in the frontal lobe with 137 voxels. This might be due to distortion of occipital grey matter that could result in folding over the field of view. In conclusion, the area of activation is determined with a cluster threshold, but the results are highly independent of the threshold values within a wide range.

8.13 GM-Content

To convert signal changes into relative changes in CBV, the grey matter signal fraction of the voxel is needed. The GM signal fraction is determined according to the technique described in section 5.5. The relative change in CBV is calculated with equation 7.1 $\frac{\Delta CBV}{CBV_{rest}} = \frac{S_{rest} - S_{act}}{S_{rest}} \frac{1}{CBV_{rest}} \frac{1}{GM_{fraction}}$. As shown in Fig. 8.15, the error in the calculation of $\frac{\Delta CBV}{CBV_{rest}}$ from $\frac{\Delta S}{S_{rest}}$ is highly dependent on the error in GM signal contribution of a voxel. For example if a voxel with a true GM signal contribution of 40% is underestimated by only 10%, then the calculated percent CBV change from VASO experiment would be overestimated by almost 20%. However, it is clear that any systematic error in the calculation of GM signal contribution will have a significant impact on the calculation of $\frac{\Delta CBV}{CBV_{rest}}$.

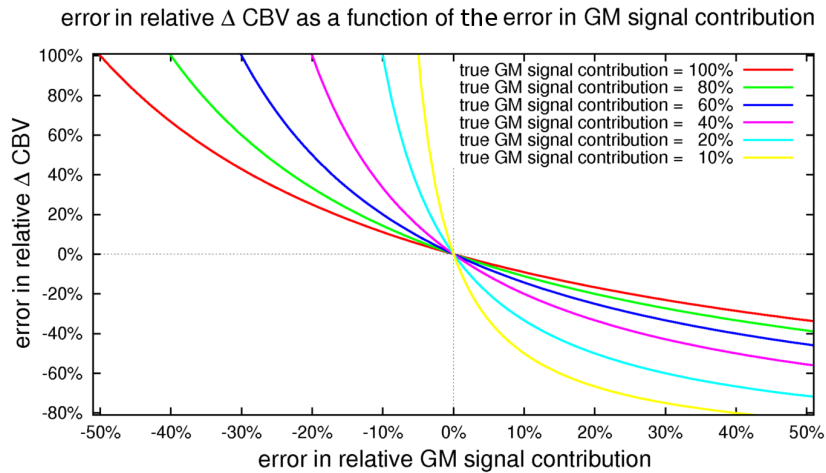


Figure 8.15: The error in $\frac{\Delta CBV}{CBV_{rest}}$ as a function of the error GM signal contribution is depicted for five values of true GM signal contributions.

To minimize the error in GM fraction determination, special attention is focused on its generation. Even though two images at different TI are enough to generate a GM mask according to the algorithm described in 5.5, images at eight different TI were acquired to minimize noise by fitting. For every TI , 10 identical images are acquired and averaged for further noise reduction. The generated GM masks are validated for every individual subject by comparison with the high resolution anatomical image acquired. Furthermore, the error in GM fraction is assumed to be unbiased. This means that even if GM might be overestimated in some voxels, this can be compensated for with voxels that show an underestimation in GM fraction. This suggests that the average in relative change in CBV is only slightly dependent on the error in GM fraction, as long as the error is within the linear range in Fig. 8.15.

8.14 Gender Dependencies

There is no significant gender dependence of blood volume change $\frac{\Delta CBV}{CBV_{rest}}$. The average change in CBV in women is $29.2 \pm 3.7\%$ and in men it is $27.2 \pm 4.5\%$ (see table 8.1 at page 98). There is, however, a significant difference in the activated volume. Women show a volume of activity of $9.210 \pm 0.837 cm^3$, while men show a significant lower ($z = 4.129$, $p < 0.0001$) volume of activity of $6.483 \pm 1.238 cm^3$. Prudent and detailed literature about dimorphism in human visual cortex is scarce. A selection of reported dimorphisms is discussed below.

- Men have larger brain volumes than women. Larger brain volumes in men can hamper the shim adjustment. An insufficient shim could lead to an SNR decrease in some areas, which reduces the z-value of activity. For low z-values the potential for false negative voxel increases, which could lead to a smaller volume of activation in men. This contradicts the fact, that the average of $\frac{\Delta CBV}{CBV_{rest}}$ is not smaller in women than in men. Furthermore, section 8.12 suggests that there are only very few false negative voxels.
- The normal hematocrit level is higher in men than in women [Billett, 1990], which results in a slightly higher blood T_1 in women. This results in a slightly more negative blood z-magnetization in women. A smaller blood z-magnetization leads to a larger VASO signal change. This could be the reason for the small gender difference in $\frac{\Delta CBV}{CBV_{rest}}$, but does not explain the difference in the activated volume.
- MacIntosh et al. [MacIntosh et al., 2010] found a significantly lower arterial arrival times in females compared to males throughout the cortex, probably due to the smaller brain volume. This could affect the contamination due to fresh (not-inverted) blood in the small vessels of the imaging slice (see 8.6). Fresh blood in the small vessels of the imaging slice could cause an underestimation in $\frac{\Delta CBV}{CBV_{rest}}$ and an ASL contamination in the data. This dimorphism also does not explain the difference in volume of activation.

- Results in [Amunts et al., 2007] show significant dimorphism in cytoarchitecture of the human visual cortex. It is suggested that different neural strategies in visual information processing are used in males and females, which correspond with anatomical differences. This could explain the difference in the activated volume of data in this study to some extent.

8.15 T_1 Dependency on Blood Nulling Time

The blood nulling time TI is chosen based on literature values of blood T_1 from Tab. 5.1. The value used in this thesis is $T_1 = 2100ms$, but the true value might differ in a range of $\approx 100ms$. The effect of the associated remaining blood signal on the determined blood volume change is estimated.

Eq. 5.2 suggests that during $100ms$ blood z-magnetization relaxes up to $\frac{M_z(TI)}{M_0 z} = 2.5\%$ of its maximal magnetization. Referring to Eq. 5.3 the VASO signal change can be estimated with Eq. 8.6.

$$\frac{\Delta VASO}{VASO_{rest}} = \frac{[(1-CBV_{rest})M_{z gm}(TI)+CBV_{rest}M_{z b}(TI)]-[(1-CBV_{act})M_{z gm}(TI)+CBV_{act}M_{z b}(TI)]}{(1-CBV_{rest})M_{z gm}(TI)+CBV_{rest}M_{z b}(TI)} \quad (8.6)$$

Assuming a CBV change of $\approx 28\%$ and $CBV_{rest} = 5.5\%$ (Tab. 5.2) the error of $\frac{\Delta CBV}{CBV_{rest}}$ in the sequece used is $\approx 5.2\%$. This value refers to the blood volume change and not the total blood volume. The error that refers to the total blood volume is $5.2\% * 0.28 = 1.45\%$. This means that the value of $\frac{\Delta CBV}{CBV_{rest}}$ should be written as $\frac{\Delta CBV}{CBV_{rest}} = 28.32\% \pm 4.49\%$ (inter-subject standard deviation) $\pm 1.45\%$ (due to incomplete blood nulling) .

8.16 Water Exchange Between Tissue and Blood During TI

Due to the long blood T_1 at high fields and due to the specific non-steady-state properties of blood in the slab-selective VASO approach, this study uses longer inversion times than any other published VASO variant. Therefore the influence of the long TI must be discussed. In specific, the water exchange and the corresponding magnetization exchange between intravascular and extravascular space must be considered. Blood magnetization that perfuses into the extravascular space relaxes there with tissue T_1 instead of blood T_1 . At the blood nulling point, that magnetization would not be nulled. Up to linear order, this effect is compensated with tissue magnetization that perfuses into the vessels and relaxes there with blood T_1 . Recently, Wu et al. simulated this effect in a two compartment model as a function of physiological parameters and field strength [Wu et al., 2010]. They found a blood contribution in the order of $\approx 2\%$ at 7T, which is negligible regarding the uncertainties in blood T_1 and inter-subject stability. On the other hand, this blood signal contribution is most likely very different in arterioles, capillaries and venules. The total blood volume change might be quite independent of capillary permeability. Nonetheless, different blood compartments might be weighted differently. This could result in a time course that overestimates the arterial compartment of CBV.

9 Conclusion

VASO gives an fMRI contrast that is built on the precise performance of the inversion pulse. To make sure that blood is nulled properly, the dependencies of the implemented inversion pulse is investigated and understood in detail. It has been shown that slab-selective, BOLD-corrected VASO can give stable results of functional changes in CBV at a resolution of 1.5mm isotropic at 7T. This is possible due to the high signal increase in the slab-selective approach up to the factor of 10. It was shown that the entire visual cortex, visible in the acquired volume, has significant increase in CBV and not only peak voxels with very high signal changes. VASO gives reliable and consistent average CBV changes of $28.2\% \pm 4.5\%$. The interleaved acquisition of VASO and BOLD enables direct spatio-temporal comparison between the two contrasts. This comparison of the acquired data suggests that the surface veins contribute to BOLD signal change, but not to VASO signal change. Furthermore, the recurrence to baseline of total CBV after cessation of the stimulus is in same time scale as in BOLD. Partial volume effects of functional change of CSF can be eliminated with the developed method by nulling both steady-state CSF and flowing blood. By doing so, it has been confirmed that functional changes in CSF volume can contribute to the traditional VASO signal change. Furthermore, it was shown that slab-selective, BOLD-corrected VASO measures changes in CBV without any confounds from CBF and oxygenation in the occipital lobe. This is only true for repetition times above $\approx 1.5\text{s}$ and inversion slab thicknesses that invert blood down to $\approx 4.5\text{cm}$ below the imaging slice.

Further improvements can be done with respect to the sampled volume. With the developed VASO variant, a precise measurement of CBV is only possible for one slice. Published techniques that increase the coverage to the entire brain can be adopted [Scouten and Constable, 2007] [Hua et al., 2011a] [Poser, 2009] [Ciris et al., 2011]. The resolution can be improved with faster acquisition techniques, such as parallel acquisition or zoomed methods that enable smaller fields of view. For precise understanding concerning different CBF contamination in arteries, capillaries and venules, the role of the capillary permeability has to be further investigated.

The combined sampling of BOLD and CBV might be useful in studies where changes in BOLD signal are not directly dependent on neural activity alone, but on the particular interplay of CBF, CBV and CMRO_2 , e.g. in studies concerning BOLD signal differences dependent on gender, age, pathology or pharmacology.

The developed VASO variant can be useful to investigate the functional hemodynamics in volunteers with unprecedented resolution and without the use of an exogenous contrast agents.

Bibliography

- [Abbas, 2010] Abbas, Z. (2010). Mr-parameter mapping of human brain at 7 tesla. Master’s thesis, Department of Physics and Earth Sciences of the Leipzig University and Max Planck Institute for Human Cognitive and Brain Sciences.
- [Abraham, 1961] Abraham, A. (1961). *The principles of nuclear magnetism*. Oxford: Clarendon Press.
- [Amunts et al., 2007] Amunts, K., Armstrong, E., Malikovic, A., Homke, L., Mohlberg, H., Schleicher, A., and Zilles, K. (2007). Gender-specific left-right asymmetries in human visual cortex. *The Journal of Neuroscience, February*, 7:1356–1364.
- [Anderson et al., 2006] Anderson, J., Shafi, N. I., and Brayan, R. M. (2006). Endothelial influence on cerebrovascular tone. *Journal of Applied Physiology*, 100:318–327.
- [Belliveau et al., 1991] Belliveau, J. W., Kennedy, D. N., McKinstry, R. C., Buchbinder, B. R., Weisskoff, R. M., Cohen, M. S., Vevea, J. M., Brady, T. J., and Rosen, B. R. (1991). Functional mapping of the human visual cortex by magnetic resonance imaging. *Science*, 254:716–719.
- [Bernstein et al., 2004] Bernstein, M. A., King, K. F., and Zhou, X. J. (2004). *Handbook of MRI Pulse Sequences*. Elsevier Academic Press.
- [Billett, 1990] Billett, H. H. (1990). *Clinical Methods: The History, Physical, and Laboratory Examinations. 3rd edition*. Butterworth Publishers.
- [Bodurka et al., 2007] Bodurka, J., Ye, F., Petridou, N., Murphy, K., and Bandettini, P. A. (2007). Mapping the mri voxel volume in which thermal noise matches physiological noise - implications for fmri. *NeuroImage*, 34:542–549.
- [Brooks and Chiro, 1987] Brooks, R. A. and Chiro, G. D. (1987). Magnetic resonance imaging of stationary blood: a review. *Medical Physics*, 14:903–913.
- [Bulte et al., 2007] Bulte, D. P., Chiarelli, P. A., Wise, R., and Jezzard, P. (2007). Measurement of cerebral blood volume in humans using hyperoxic mri contrast. *Journal of Magnetic Resonance Imaging*, 26:894–899.
- [Buxton, 2009] Buxton, R. B. (2009). *Introduction to Functional Magnetic Resonance Imaging*. Cambridge University Press, 2 edition.
- [Buxton, 2010] Buxton, R. B. (2010). Interpreting oxygenation-based neuroimaging signals: the importance and the challenge of understanding brain oxygen metabolism. *Frontiers in Neuroenergetics*, 2:8.

- [Buxton et al., 1998] Buxton, R. B., Wong, E. C., and Frank, L. R. (1998). Dynamics of blood flow and oxygenation changes during brain activation: the balloon model. *Magnetic Resonance in Medicine*, 39:855–864.
- [Chen and Pike, 2009] Chen, J. J. and Pike, G. B. (2009). Origins of the bold post-stimulus undershoot. *Neuroimage*, 46:559–568.
- [Chen and Pike, 2010a] Chen, J. J. and Pike, G. B. (2010a). Global cerebral oxidative metabolism during hypercapnia and hypocapnia in humans: implications for bold fmri. *Journal of Magnetic Resonance Imaging*, 30:1094–1099.
- [Chen and Pike, 2010b] Chen, J. J. and Pike, G. B. (2010b). Mri measurement of the bold-specific flow–volume relationship during hypercapnia and hypocapnia in humans. *Neuroimage*, 53:383–391.
- [Chen et al., 2011] Chen, Y., Wang, D. J., and Detre, J. A. (2011). Comparison of arterial transit times estimated using arterial spin labeling. *Magnetic Resonance Materials in Physics Biology and Medicine.*, 24.
- [Chiarelli et al., 2007] Chiarelli, P. A., Bulte, D. P., Wise, R., Gallichan, D., and Jezard, P. (2007). A calibration method for quantitative bold fmri based on hyperoxia. *NeuroImage*, 37:808–820.
- [Ciris et al., 2011] Ciris, P. A., Qiu, M., and Constable, R. T. (2011). Non-invasive quantification of absolute cerebral blood volume. In *Proceedings of the International Society of Magnetic Resonance in Medicine*.
- [Cohalan, 2009] Cohalan, C. (2009). Cerebral blood volume changes during human neural activation: A comparative study of vaso and verve. Master’s thesis, McGill University, Montreal.
- [Conolly et al., 1991] Conolly, S., Glover, G. H., Nishimura, D., and Macovski, A. (1991). A reduced power selective adiabatic spin-echo pulse sequence. *Magnetic Resonance in Medicine*, 18:28–38.
- [Conolly et al., 1988] Conolly, S., Nishimura, D., and Glover, G. H. (1988). Variable-rate selective excitation. *Magnetic Resonance in Medicine*, 78:440–458.
- [Conolly et al., 1989] Conolly, S., Nishimura, D., and Macovski, A. (1989). Sweep diagram analysis of selective adiabatic pulses. *Journal of Magnetic Resonance*, 83:549–564.
- [Czosnyka et al., 2004] Czosnyka, M., Czosnyka, Z., and an dJ. C. Pickard, S. M. (2004). Cerebrospinal fluid dynamics. *Physiological Measurement*, 25:R51–R76.
- [Dechent et al., 2010] Dechent, P., Schütze, G., Helms, G., Merboldt, K. D., and Frahm, J. (2010). Basal cerebral blood volume during the poststimulation undershoot in bold mri of the human brain. *Journal of Cerebral Blood Flow and Metabolism*, 31:82–89.

- [Detre et al., 1992] Detre, J. A., Leigh, J. S., and Williams, D. S. (1992). Perfusion imaging. *Magnetic Resonance in Medicine*, 23:37–45.
- [Dobre et al., 2006] Dobre, M. C., Uğurbil, K., and Marjanska, M. (2006). Determination of longitudinal relaxation time (t1) at high magnetic field strengths. *Magnetic Resonance Imaging*, 25:733–735.
- [Donahue et al., 2009a] Donahue, M. J., Blicher, J. U., Ostergaard, L., Feinberg, D. A., MacIntosh, B. J., Miller, K. L., Günther, M., and Jezzard, P. (2009a). Cerebral blood flow, blood volume, and oxygen metabolism dynamics in human visual and motor cortex as measured by whole-brain multi-modal magnetic resonance imaging. *Journal of Cerebral Blood Flow and Metabolism*, 29:1856–1866.
- [Donahue et al., 2009b] Donahue, M. J., Hua, J., Pekar, J. J., and van Zijl, P. C. M. (2009b). Effect of inflow of fresh blood on vascular-space-occupancy (vaso) contrast. *Magnetic Resonance in Medicine*, 61:473–480.
- [Donahue et al., 2006] Donahue, M. J., Lu, H., Jones, C. K., Edden, R. A. E., Pekar, J. J., and van Zijl, P. C. M. (2006). Theoretical and experimental investigation of vaso contrast mechanism. *Magnetic Resonance in Medicine*, 56:1261–1273.
- [Donahue et al., 2010] Donahue, M. J., Sideso, E., MacIntosh, B. J., Kennedy, J., Handa, A., and Jezzard, P. (2010). Absolute arterial cerebral blood volume quantification using inflow vascular-space-occupancy with dynamic subtraction magnetic resonance imaging. *Journal of Cerebral Blood Flow and Metabolism*, 30:1329–1342.
- [Duelli and Kuschinsky, 1993] Duelli, R. and Kuschinsky, W. (1993). Changes in brain capillary diameter during hypocapnia and hypercapnia. *Journal of Cerebral Blood Flow and Metabolism*, 12:125–128.
- [Edelstein et al., 1986] Edelstein, W. A., Glover, G. H., Hardy, C. J., and Redington, R. W. (1986). The intrinsic signal-to-noise ratio in nmr imaging. *Magnetic Resonance in Medicine*, 3:604–618.
- [Engvall et al., 2008] Engvall, C., Ryding, E., Wirestam, R., Holtas, S., Ljunggren, K., Ohlsson, T., and Reinstrup, P. (2008). Human cerebral blood volume (cbv) measured by dynamic susceptibility contrast mri and 99mtc-rbc spect. *Journal of Neurosurgical Anesthesiology*, 1:41–44.
- [Figueiredo et al., 2005] Figueiredo, P. M., Clare, S., and Jezzard, P. (2005). Quantitative perfusion measurements using pulsed arterial spin labeling: effects of large region-of-interest analysis. *Journal of Magnetic Resonance Imaging*, 21:676–682.
- [Fox, 1986] Fox, P. T. (1986). Focal physiological uncoupling of cerebral blood flow and oxidative metabolism during somatosensory stimulation in human subjects. *Proc Natl Acad Sci USA*, 83:1140–1144.

- [Francis et al., 2008] Francis, S. T., Bowtell, R. W., and Gowland, P. A. (2008). Modeling and optimization of look-locker spin labeling for measuring perfusion and transit time changes in activation studies taking into account arterial blood volume. *Magnetic Resonance Imaging*, 59:316–325.
- [Frank et al., 1994] Frank, J., Massay, V., Duyn, J., Soberin, G., Barrios, F., Zigun, J., Sexton, R., Kwok, P., Woo, J., and Moonen, C. (1994). Measurement of relative cerebral blood volume changes with visual stimulation by double dose gadopentate dimeglumine enhanced dynamic magnetic resonance imaging. *Investigative Radiology*, 29:157–160.
- [Giovacchini et al., 2002] Giovacchini, G., Chang, M. C., Channing, M. A., Toczek, M., Mason, A., Bokde, A. L., Connolly, C., Vuong, B. K., Ma, Y., Der, M. G., Doudet, D. J., Herscovitch, P., Eckelman, W. C., Rapoport, S. I., and RE, R. E. C. (2002). Brain incorporation of ¹¹c-arachidonic acid in young healthy humans measured with positron emission tomography. *Journal of Cerebral Blood Flow and Metabolism*, 22:1453–1462.
- [Gordon et al., 2011] Gordon, G. R., Howarth, C., and MacVicar, B. A. (2011). Bidirectional control of arteriole diameter by astrocytes. *Experimental Physiology*, 98:393 – 399.
- [Gough, 2009] Gough, B., editor (2009). *GNU Scientific Library Reference Manual*. Network Theory Ltd.
- [Grubb et al., 1974] Grubb, R. L., Raichle, M. E., Eichling, J. O., and Ter-Pogossian, M. M. (1974). The effect of changes in paco₂ cerebral blood volume, blood flow, and vascular mean transit time. *Journal of the American Heart Association*, 5:630–639.
- [Gu et al., 2006] Gu, H., Lu, H., Ye, F. Q., Stein, E. A., and Yang, Y. (2006). Noninvasive quantification of cerebral blood volume in humans during functional activation. *Neuroimage*, 30:377–387.
- [Hall et al., 2011] Hall, E. L., Gowland, P. A., and Francis, S. T. (2011). Look-locker 3d-epi asl at 7t. In *Proceedings of the International Society of Magnetic Resonance in Medicine*.
- [Harrison et al., 2002] Harrison, R. V., Harrel, N., Panesar, J., and Mount, R. J. (2002). Blood capillary distribution correlates with hemodynamic-based functional imaging in cerebral cortex. *Cerebral Cortex*, 12:225–233.
- [Helgstrand et al., 2000] Helgstrand, M., Härd, T., and Allard, P. (2000). Simulations of nmr pulse sequences during equilibrium and non-equilibrium chemical exchange. *Journal of Biomolecular NMR*, 18:49–63.
- [Herman et al., 2009] Herman, P., Sanganahalli, B. G., and Hyder, F. (2009). Multi-modal measurements of blood plasma and red blood cell volumes during functional brain activation. *Journal of Cerebral Blood Flow and Metabolism*, 29:19–24.

- [Hillman et al., 2007] Hillman, E. M. C., Devor, A., Bouchard, M. B., Dunn, A. K., Krauss, G. W., Skoch, J., Bacsikai, B. J., Dale, A. M., and Boas, D. A. (2007). Depth-resolved optical imaging and microscopy of vascular compartment dynamics during somatosensory stimulation. *NeuroImage*, 35:89–104.
- [Hoge et al., 1999] Hoge, R. D., Atkinson, J., Gill, B., Crelier, G. R., Marrett, S., and Pike, G. B. (1999). Investigation of bold signal dependence on cerebral blood flow and oxygen consumption: The deoxyhemoglobin dilution model. *Magnetic Resonance in Medicine*, 42:849–863.
- [Hua et al., 2009] Hua, J., Donahue, M. J., Zhao, J. M., Grgac, K., Huang, A. J., Zhou, X. J., and van Zijl, P. C. M. (2009). Magnetization transfer enhanced vascular-space-occupancy (mt-vaso) functional mri. *Magnetic Resonance in Medicine*, 61:944–951.
- [Hua et al., 2011a] Hua, J., Jones, C. K., and van Zijl, P. C. M. (2011a). Vascular-space-occupancy (vaso) mri in human brain at 7t. In *Proceedings of the International Society of Magnetic Resonance in Medicine*.
- [Hua et al., 2011b] Hua, J., Qin, Q., Donahue, M. J., Zhou, J., Pekar, J. J., and van Zijl, P. C. M. (2011b). Inflow-based vascular-space-occupancy (ivaso) mri. *Magnetic Resonance in Medicine*, 66:40–56.
- [Hua et al., 2011c] Hua, J., Qin, Q., Pekar, J. J., and van Zijl, P. C. M. (2011c). Measurement of absolute arterial cerebral blood volume in human brain without using a contrast agent. *Nuclear Magnetic Resonance in Biomedicine*.
- [Huk et al., 2002] Huk, A. C., Dougherty, R. F., and Heeger, D. J. (2002). Retinotopy and functional subdivision of human areas mt and mst. *Journal of Neuroscience*, 22:7195–7205.
- [Hurley et al., 2010] Hurley, A. C., Al-Radaideh, A., Bai, L., Aickelin, U., Coxon, R., Glover, P., and Gowland, P. A. (2010). Tailored rf pulse for magnetization inversion at ultrahigh field. *Magnetic Resonance in Medicine*, 63:51–58.
- [Insko and Bolinger, 1993] Insko, E. and Bolinger, L. (1993). Mapping of the radiofrequency field. *Magnetic Resonance in Medicine*, 103:82–85.
- [Ito et al., 2004] Ito, H., Kanno, I., Kato, C., Sasaki, T., Ishii, K., Ouchi, Y., Iida, A., Okazawa, H., Hayashida, K., Tsuyuguchi, N., Ishii, K., Kuwabara, Y., and Senda, M. (2004). Database of normal human cerebral blood flow, cerebral blood volume, cerebral oxygen extraction fraction and cerebral metabolic rate of oxygen measured by positron emission tomography with 15o-labelled carbon dioxide or water, carbon monoxide and oxygen: a multicentre study in japan. *European Journal of Nuclear Medicine and Molecular Imaging*, 31:635–643.
- [Ito et al., 2001] Ito, H., Takahashi, K., Hatazawa, J., Kim, S.-G., and Kanno, I. (2001). Changes in human regional cerebral blood flow and cerebral blood volume during

- visual stimulation measured by positron emission tomography. *Journal of Cerebral Blood Flow and Metabolism*, 21:608–612.
- [Ivanov et al., 2011] Ivanov, D., Lohmann, G., Kabisch, S., Henseler, I., Schloegl, H., Heinke, W., Hutton, C., , and Turner, R. (2011). Breathing gas calibration for mr cmro2 measurments: comparative effects on functional brain networks. In *Proceedings of the Inernational Society of Magnetic Resonance in Medicine*.
- [Ivanov et al., 1981] Ivanov, K. P., Kalinina, M. K., and Levkovich, Y. I. (1981). Blood flow velocity in capillaries of brain and muscles and its physiological significance. *Microvascular Research*, 22:143–155.
- [Jin and Kim, 2008] Jin, T. and Kim, S.-G. (2008). Improved cortical-layer specificity of vascular space occupancy fmri with slab inversion relative to spin-echo bold at 9.4 t. *Neuroimage*, 40:59–67.
- [Jochimsen and v. Mengershausen, 2004] Jochimsen, T. H. and v. Mengershausen, M. (2004). Odin-object-oriented development interface for nmr. *Journal of Magnetic Resonance*, 170:67–78.
- [Kandel et al., 2000] Kandel, E., Schwartz, J., and Jessell, T. (2000). *Principles of Neural Science*. McGraw-Hill.
- [Kelly, 1824] Kelly, G. (1824). Appearances observed in the dissection of two individuals; death from cold and congestion of the brain. *Trans Med Chir Sci Edinb*, 1:84–169.
- [Kennerley et al., 2010] Kennerley, A. J., J. E. Mayhew, P. R., and Berwick, J. (2010). Vascular origins of bold and cbv fmri signals: Statistical mapping and histological sections compared. *The Open Neuroimaging Journal*, 4:1–8.
- [Kim and Bandettini, 2010] Kim, S. G. and Bandettini, P. A. (2010). *BOLD fMRI: A Guide to Functional Imaging for Neuroscientists.*, chapter Chapter 1. Principles of Functional MRI. S. H. Faro and F. B. Mohamed.
- [Kim and Kim, 2010] Kim, T. and Kim, S. G. (2010). Temporal dynamics and spatial specificity of arterial and venous blood volume changes during visual stimulation: implication for bold quantification. *Journal of Cerebral Blood Flow and Metabolism*, 12:1211–1222.
- [Koopmans et al., 2010] Koopmans, P. J., Barth, M., and Norris, D. G. (2010). Layer-specific bold activation in human v1. *Human Brain Mapping*, 31:1297–1304.
- [Krieger, 2010] Krieger, S. (2010). Cerebral blood volume weighted fmri: A physiological and hemodynamical analysis. Master’s thesis, Department of Physics and Earth Sciences of the Leipzig University.
- [Kuschinsky, 1996] Kuschinsky, W. (1996). Capillary perfusion in the brain. *Brain Research*, 432:R42–R46.

- [Kuschinsky, 2000] Kuschinsky, W. (2000). *Regulation of Cerebral Blood Flow*. In: *Functional MRI*, pages 15–24. C. T. W. Moonen and P. A. Bandettini.
- [Lee et al., 2001] Lee, S. P., Duong, T. Q., Yang, G., Iadecola, C., and Kim, S. G. (2001). Relative changes of cerebral arterial and venous blood volumes during increased cerebral blood flow: implications for bold fmri. *Magnetic Resonance in Medicine*, 45:791–800.
- [Leontiev and Buxton, 2007] Leontiev, O. and Buxton, R. B. (2007). Reproducibility of bold, perfusion, and cmro2 measurements with calibrated-bold fmri. *NeuroImage*, 35:175–184.
- [Lin et al., 2011] Lin, A.-L., Lu, H., Fox, P. T., and Duong, T. Q. (2011). Cbv measurements-gd dtpa vs. vaso- and their relationship with cbf in activated human cortex. In *Proceedings of the International Society of Magnetic Resonance in Medicine*.
- [Lu, 2008] Lu, H. (2008). Magnetization ‘reset’ for non-steady-state blood spins in vascular-space-occupancy (vaso) fmri. In *Proceedings of the International Society of Magnetic Resonance in Medicine*.
- [Lu et al., 2004] Lu, H., Clingman, C., Golay, X., and van Zijl, P. C. M. (2004). Determination of longitudinal relaxation time t1 of blood at 3.0 tesla. *Magnetic Resonance in Medicine*, 52:679–628.
- [Lu et al., 2003] Lu, H., Golay, X., Pekar, J. J., and van Zijl, P. C. M. (2003). Functional magnetic resonance imaging based on changes in vascular space occupancy. *Magnetic Resonance in Medicine*, 50:263–274.
- [Lu et al., 2005] Lu, H., Law, M., Johnson, G., Ge, Y., and van Zijl, P. C. M. (2005). Novel approach to the measurement of absolute cerebral blood volume using vascular-space-occupancy magnetic resonance imaging. *Magnetic Resonance in Medicine*, 54:1403–1411.
- [Lu and van Zijl, 2005] Lu, H. and van Zijl, P. C. M. (2005). Experimental measurement of extravascular parenchymal bold effect and tissue oxygen extraction fraction using multi-echo vaso fmri at 1.5 and 3.0 t. *Magnetic Resonance in Medicine*, 53:808–816.
- [MacIntosh et al., 2010] MacIntosh, B., Filippini, N., Chappell, M. A., Woolrich, M. W., Mackay, C. E., and Jezzard, P. (2010). Assessment of arterial arrival times derived from multiple inversion time pulsed arterial spin labeling mri. *Magnetic Resonance in Medicine*, 63:641–647.
- [Mandeville et al., 1999] Mandeville, J. B., Marota, J. J., Ayata, C., Zaharchuk, G., Moskowitz, M. A., Rosen, B. R., and Weisskoff, R. M. (1999). Evidence of a cerebrovascular postarteriole windkessel with delayed compliance. *Journal of Cerebral Blood Flow and Metabolism*, 19:679–689.

- [Mandeville et al., 1998] Mandeville, J. B., Marota, J. J., Kosofsky, B. E., Keltner, J. R., Weissleder, R., Rosen, B. R., and Weisskoff, R. M. (1998). Dynamic functional imaging of relative cerebral blood volume during rat forepaw stimulation. *Magnetic Resonance in Medicine*, 39:615–624.
- [Mansfield, 1977] Mansfield, P. (1977). Multi-planar image formation using nmr spin echoes. *Journal of Physics*, 10.
- [Mark et al., 2011] Mark, C. I., Fisher, J. A., and Pike, G. B. (2011). Improved fmri calibration: Precisely controlled hyperoxic versus hypercapnic stimuli. *NeuroImage*, 54:1102–1111.
- [Mehta et al., 1996] Mehta, R. C., Pike, G. B., and Enzmann, D. R. (1996). Magnetization transfer magnetic resonance imaging: A clinical review. *Topics in Magnetic Resonance Imaging*, 8:214–230.
- [Mildner et al., 2010] Mildner, T., Hetzer, S., Driesel, W., Müller, K., and Möller, H. E. (2010). Flow-weighted arterial transit time mapping of the human brain. In *Proceedings of the International Society of Magnetic Resonance in Medicine*.
- [Murphy et al., 2007] Murphy, K., Bodurka, J., and Bandettini, P. A. (2007). How long to scan? the relationship between fmri temporal signal to noise ratio and necessary scan duration. *Neuroimage*, 34:565–574.
- [Nezafat et al., 2009] Nezafat, R., Ouwerkerk, R., Derbyshire, A. J., Stuber, M., and McVeigh, E. R. (2009). Spectrally selective b1-insensitive t2 magnetization preparation sequence. *Magnetic Resonance in Medicine*, 61:1326–1335.
- [Norris, 2002] Norris, D. G. (2002). Adiabatic radiofrequency pulse forms in biomedical nuclear magnetic resonance. *Concepts in Magnetic Resonance*, 14:89–101.
- [Ogawa et al., 1990] Ogawa, S., Lee, T. M., and Nayak, A. S. (1990). Oxygenation-sensitive contrast in magnetic resonance image of rodent brain at high magnetic fields. *Magnetic Resonance in Medicine*, 14:68–78.
- [Ordidge et al., 1996] Ordidge, R. J., Wylenzinska, M. W., Hugg, J. W., Butterworth, E., and Franconi, F. (1996). Frequency offset corrected inversion (foci) pulses for use in localized spectroscopy. *Magnetic Resonance in Medicine*, 36:562–566.
- [Pawlik et al., 1981] Pawlik, G., Rackl, A., and Bing, R. J. (1981). Quantitative capillary topography and blood flow in the cerebral cortex of cats: An in vivo microscopic study. *Brain Research*, 208:35–58.
- [Pears et al., 2003] Pears, J., Francis, S. T., Butterworth, S., Bowtell, R. W., and Gowland, P. A. (2003). Investigating the bold effect during infusion of gd dtpa using rapid t2 imaging. *Magnetic Resonance in Medicine*, 49:61–70.

- [Penny et al., 2007] Penny, W. D., Friston, K. J., Ashburner, J. T., Kiebel, S. J., and Nichols, T. E. (2007). *Statistical Parametric Mapping: The Analysis of Functional Brain Images*. Academic Press London.
- [Peppiatt and Attwell, 2004] Peppiatt, C. and Attwell, D. (2004). Feeding the brain. *Nature*, 431:137–138.
- [Piechnik et al., 2009] Piechnik, S. K., Evans, J., Bary, L. H., Wise, R. G., and Jezzard, P. (2009). Functional changes in csf volume estimated using measurement of water t2 relaxation. *Magnetic Resonance in Medicine*, 61:579–586.
- [Poser, 2009] Poser, B. (2009). *Techniques for BOLD and blood volume weighted fMRI*. Donders Series.
- [Poser et al., 2011] Poser, B., Mierlo, E., and Norris, D. G. (2011). Exploring the post-stimulus undershoot with spin-echo fmri: Implications for models of neurovascular response. *Human Brain Mapping*, 32:141–153.
- [Poser and Norris, 2011] Poser, B. and Norris, D. G. (2011). Application of whole-brain cbv-weighted fmri to a cognitive stimulation paradigm: Robust activation detection in a stroop task experiment using 3d grase vaso. *Human Brain Mapping*, 32:974–981.
- [Poser and Norris, 2007] Poser, B. A. and Norris, D. G. (2007). Measurement of activation-related changes in cerebral blood volume: Vaso with single-shot haste acquisition. *Magnetic Resonance Materials in Physics, Biology and Medicine*, 20:63–67.
- [Rooney et al., 2007] Rooney, W. D., Johnson, G., Li, X., Cohen, E. R., Kim, S.-G., Ugurbil, K., and Springer, C. S. (2007). Magnetic field and tissue dependencies of human brain longitudinal h2o relaxation in vivo. *Magnetic Resonance in Medicine*, 57:308–318.
- [Rostrup et al., 2005] Rostrup, E., Knudsen, G. M., Law, I., Holm, S., Larsson, H. B. W., and Paulson, O. B. (2005). The relationship between cerebral blood flow and volume in humans. *Neuroimage*, 24:1–11.
- [Schroeter et al., 2006] Schroeter, M. L., Kupka, T., Mildner, T., Uludag, K., and v. Cramon, D. Y. (2006). Investigating the post-stimulus undershoot of the bold signal—a simultaneous fmri and fnirs study. *NeuroImage*, 30:349–358.
- [Scouten and Constable, 2007] Scouten, A. and Constable, R. T. (2007). Application and limitations of whole-brain magic vaso fuctional imaging. *Magnetic Resonance in Medicine*, 58:306–315.
- [Scouten and Constable, 2008] Scouten, A. and Constable, R. T. (2008). Vaso-based calculations of cbv change: Accounting for the dynamic csf volume. *Magnetic Resonance in Medicine*, 58:308–315.

- [Shen et al., 2009] Shen, Y., Kauppinen, R. A., Vidyasagar, R., and Golay, X. (2009). A functional magnetic resonance imaging technique based on nulling extravascular gray matter signal. *Journal of Cerebral Blood Flow and Metabolism*, 29:144–156.
- [Shin et al., 2010] Shin, W., Geng, X., Gu, H., Zhan, W., Zou, Q., and Yang, Y. (2010). Automated brain tissue segmentation based on fractional signal mapping from inversion recovery look-locker acquisition. *NeuroImage*, 52:1347–1354.
- [Siemens, 2010] Siemens (2010). *IDEA Sequenze programming Course*. Siemens Training and Development Center, North Carolina, USA.
- [Silver et al., 1984] Silver, M. S., Joseph, R. I., Chen, C., Sank, V. J., and Hoult, D. I. (1984). Selective population inversion in nmr. *Nature*, 310:681–683.
- [Slichter, 1989] Slichter, C. P. (1989). *Principles of Magnetic Resonance*. Springer-Verlag.
- [Stefanovic and Pike, 2005] Stefanovic, B. and Pike, G. B. (2005). Venous refocusing for volume estimation: Verve functional magnetic resonance imaging. *Magnetic Resonance in Medicine*, 53:339–347.
- [Stehling et al., 1998] Stehling, M. K., Schmitt, F., and Turner, R. (1998). *Echo-Planar Imaging Theory, Thechnique an Application*. Springer-Verlag.
- [Taheri and Sood, 2006] Taheri, S. and Sood, R. (2006). Spin-lock mri with amplitude- and phase-modulated adiabatic waveforms: an mr simulation study. *Magnetic Resonance Imaging*, 24:51–59.
- [Tjandra et al., 2005] Tjandra, T., Brooks, J. C. W., Figueiredo, P., Wise, R., Matthews, P. M., and Tracey, I. (2005). Quantitative assessment of the reproducibility of functional activation measured with bold and mr perfusion imaging: Implications for clinical trial design. *NeuroImage*, 27:393–401.
- [Turner, 2002] Turner, R. (2002). How much cortex can a vein drain? downstream milustion of activation-related cerebral blood oxygenation changes. *NeuroImage*, 16:1062–1067.
- [Turner and Thomas, 2007] Turner, R. and Thomas, D. L. (2007). Cerebral blood volume: Measurment and change. In *Proceedings of the Inernational Society of Magnetic Resonance in Medicine*.
- [Tuunanen et al., 2006] Tuunanen, P., Vidyasagar, R., and Kauppinen, R. A. (2006). Effects of mild hypoxic hypoxia on poststimulus undershoot of blood-oxygenation-level-dependent fmri signal in the human visual cortex. *Magnetic Resonance Imaging*, 24:993–999.
- [Uh et al., 2011] Uh, J., Lin, A.-L., Lee, K., Liu, P., Fox, P., and Lu, H. (2011). Validation of vaso cerebral blood volume measurement with positron emission tomography. *Magnetic Resonance in Medicine*, 65:744–749.

- [Vafae and Gjedde, 2004] Vafae, M. S. and Gjedde, A. (2004). Spatially dissociated flow-metabolism coupling in brain activation. *Neuroimage*, 21:507–515.
- [van de Moortele et al., 2005] van de Moortele, P. F., Akgun, C., Adriany, G., Moeller, S., Ritter, J., Collins, C. M., Smith, M. B., Vaughan, J. T., and Uğurbil, K. (2005). B1 destructive interferences and spatial phase patterns at 7 t with a head transceiver array coil. *Magnetic Resonance in Medicine*, 54:1503–1518.
- [Vaughan et al., 2001] Vaughan, J. T., Garwood, M., Collins, C. M., Liu, W., DelaBarre, L., Adriany, G., Andersen, P., Merkle, H., Goebel, R., Smith, M. B., and Uğurbil, K. (2001). 7t vs. 4t: Rf power, homogeneity, and signal-to-noise comparison in head images. *Magnetic Resonance in Medicine*, 46:24–30.
- [Villringer et al., 1994] Villringer, A., Them, A., Lindauer, U., Einhaupl, K., and Dirnagl, U. (1994). Capillary perfusion of the rat brain cortex. an in vivo confocal microscopy study. *Circulation Research: Journal of the American Heart Association*, 75:55–62.
- [Wang et al., 2011a] Wang, F., Chen, L. M., and Avison, M. J. (2011a). Specificity and stability of bold and cbv-based mapping signals for high resolution functional mapping at submillimeter resolution. In *Proceedings of the International Society of Magnetic Resonance in Medicine*.
- [Wang et al., 2011b] Wang, G., El-Sharkawy, A. M., Edelstein, W. A., Schär, M., and Bottomley, P. A. (2011b). Measuring and imaging t2 without echoes. In *Proceedings of the International Society of Magnetic Resonance in Medicine*.
- [Weber et al., 2008] Weber, B., Keller, A. L., Reichold, J., and Logothetis, N. K. (2008). The microvascular system of the striate and extrastriate visual cortex of the macaque. *Cerebral Cortex*, 18:2318–2330.
- [Wong et al., 1997] Wong, E. C., Buxton, R., and Frank, L. R. (1997). Implementation of quantitative perfusion imaging techniques for functional brain mapping using pulsed arterial spin labeling. *NMR in Biomedicine*, 10:237–249.
- [Worsley, 2001] Worsley, K. J. (2001). *Statistical analysis of activation images.*, chapter 14. P. Jezzard and P. M. Matthews and S. M. Smith.
- [Wright et al., 2008] Wright, P. J., Mougín, O. E., Totman, J. J., Peters, A. M., Brookes, J., Coxon, R., Morris, P. E., Clemence, M., Francis, S. T., Bowtell, R. W., and Gowland, P. A. (2008). Water proton t1 measurements in brain tissue at 7, 3, and 1.5t using ir-epi, ir-tse, and mprage: results and optimization. *Magnetic Resonance Materials in Physics, Biology and Medicine*, 21:121–130.
- [Wu et al., 2010] Wu, C. W., Liu, H.-L., Chen, J.-H., and Yang, Y. (2010). Effects of cbv, csf, and blood-brain barrier permeability on accuracy of pasl and vaso measurement. *Magnetic Resonance in Medicine*, 63:601–608.

- [Wu et al., 2007] Wu, W. C., Buxton, R. B., and Wong, E. C. (2007). Vascular space occupancy weighted imaging with control of residual blood signal and higher contrast-to-noise ratio. *IEEE Transactions on Medical Imaging*, 26:1319–1327.
- [Yacoub et al., 2001] Yacoub, E., Shmuel, A., Pfeuffer, J., van de Moortele, P. F., Adriany, G., Andersen, P., Vaughan, J. T., Merkle, H., Ugurbil, K., and Hu, X. (2001). Imaging brain function in human at 7 tesla. *Magnetic Resonance in Medicine*, 45:588–594.
- [Yang et al., 2004] Yang, Y., Gu, H., and Stein, E. A. (2004). Simultaneous mri acquisition of blood volume, blood flow, and blood oxygenation information during brain activation. *Magnetic Resonance in Medicine*, 52:1407–1417.
- [Yarnykh, 2007] Yarnykh, V. L. (2007). Actual flip-angle imaging in the pulsed steady state: A method for rapid three-dimensional mapping of the transmitted radiofrequency field. *Magnetic Resonance in Medicine*, 57:192–200.
- [Zaharchuk et al., 2005] Zaharchuk, G., Martin, A. J., Rosenthal, G., Manley, G. T., and Dillon, W. P. (2005). Measurement of cerebrospinal fluid oxygen partial pressure in humans using mri. *Magnetic Resonance in Medicine*, 54:113–121.

Acknowledgments

Herewith I want to thank all people that supported me during my master thesis. This thesis is done at the Max Planck Institute (MPI) for Human Cognitive and Brain Sciences in Leipzig, but it is supervised by the Ludwig-Maximilians-Universität (LMU) in Munich. In the first place, I want to thank my supervisor Walter Assmann for giving me the opportunity to do such an external thesis outside the university. I want to thank him, as well as Olaf Dietrich and Michael Peller from the LMU for advising me throughout this thesis. I would foremost like to thank my supervisor Robert Turner from the MPI for giving me the opportunity to be a part of his lab and for kindly guiding me through this project. I want to sincerely thank Dimo Ivanov. He spent a huge amount of time answering my questions, looking after me and discussing with me on a daily basis. He helped me to understand the physical and the physiological basics of fMRI. He taught me how to operate an MR scanner and how to use evaluation software packages. He arranged the experimental setup of the hyperoxia experiments and helped me perform and evaluate the corresponding data. His enormous knowledge of the appropriate literature helped me to get a good and fast overview of the current scientific discussion. In addition, I am grateful for his proofreading. I am grateful to Markus Streicher. He shared his Bloch simulation program with me that helped me to understand the features of the implemented tr-FOCI pulse. Furthermore, discussions with him always pushed me to a deeper physical understanding. I am thankful to Steffen Krieger for the discussions about the origin of blood volume changes and his efforts in proofreading this thesis. I want to thank Robert Trampel for his explanations concerning scanner software and scanner hardware. I am thankful to Toralf Mildner and Kathrin Lorenz for discussing the developed VASO sequence with respect to dependencies on blood arrival and transit times. I am grateful to Robin Heidemann and Andreas Schäfer for their kind explanations about the basics of the sequence programming environment IDEA. I would like to sincerely thank the medical technical assistants Domenica Wilfling and Elisabeth Wladimirow for kindly scheduling and preparing the subjects. I am thankful for the software support from Enrico Reimer. His programs were used to convert MRI data in suitable format. I want to thank Jessica Schulz for sharing her matlab programs with me, which helped me to simulate MRI artifacts in EPI. I want to thank Carsten Kögler for his kind and patient answers about RF data acquisition and RF coils and RF fields. I am grateful to all study participants who volunteers their time for the advancement of science. I am grateful for the financial support from my parents Doris Huber and Rupert Huber. Without this support this thesis would not have come to be. I want to thank Michael Paul for explaining to me how the eddy current correction of the scanner works. I am grateful to Beth Coppermayr for proofreading the thesis with respect to proper English phrasing. I want to thank Stefan Geyer for explaining to me the physiological basis of capillaries and the spinal canal. I am thankful to Jun Hua for his literature recommendation and his helpful answers to my questions. I am thankful to Pruce Pike for his advice concerning the pitfalls of VASO that are visible in the comparison of VASO and VERVE done by his student Claire Cohalan.

Erklärung:

Hiermit erkläre ich, die vorliegende Arbeit selbständig verfasst zu haben und keine anderen als die in der Arbeit angegebenen Quellen und Hilfsmittel benutzt zu haben.

München, 01.11.2011